

https://dspace.org/

The effect of metal support interactions between a cobalt catalyst and carbon dots (Cdots) in cobalt fischer-tropsch catalysts

Mokoloko, Lerato Lydia

2018

https://hdl.handle.net/10539/26174

Mokoloko, Lerato Lydia (2018) The effect of metal to support interactions between a cobalt catalyst and carbon dots (Cdots) in cobalt Fischer-Tropsch catalysts, University of the Witwatersrand, Johannesburg, <http://hdl.handle.net/10539/26174>

Downloaded from a DSpace repository. https://dspace.org/

The Effect of Metal to Support Interactions between a Cobalt catalyst and Carbon Dots (Cdots) in Cobalt Fischer-Tropsch Catalysts

By

Lerato Lydia Mokoloko

Student Number: 562061

A dissertation submitted to the Faculty of Science, University of the Witwatersrand, Johannesburg, in fulfilment for the degree of Master of Science in Chemistry.

Supervisor: Prof Neil J Coville

Co-Supervisor: Dr Roy P Forbes

University of the Witwatersrand, Johannesburg, January 2018

DECLARATION

I declare that this dissertation in my own, unaided work. It is being submitted for a Master of Science at the Faculty of Science, University of the Witwatersrand, Johannesburg. It has not been submitted before for any degree or examination at any other University.



(Signature of candidate)

On this 30th day of January 2018 at the University of the Witwatersrand

ABSTRACT

The aim of this study was to introduce functionalized carbon dots (Cdots) as potential support and reducing agents for cobalt-based Fischer-Tropsch catalysts. Cdots with different physicochemical properties were synthesized from natural-based product such as ascorbic acid, sucrose and chitosan, using microwave-assisted reactions. Two types of Cdots, namely N-free Cdots (or Cdots) and N-doped Cdots, with particle sizes < 10 nm were produced. Both Cdots and N-doped Cdots have an amorphous structure, containing both sp^2 and sp^3 type carbon. The surface of Cdots contained mainly hydroxyl and carboxyl functional groups, while N-doped Cdots contained hydroxyl, carbonyl, and nitrogen-based (mainly pyridinic and pyrrolic) functional groups.

Spinel Co_3O_4 nanoparticles with 10 nm crystallite sizes were synthesized from the "benzyl alcohol route". Both the spinel Co_3O_4 nanoparticles and functionalized Cdots were used to prepare the inverse Co_3O_4/Cdots and Co_3O_4/N-doped Cdots catalysts. The *in-situ* XRD results showed that under H_2 gas reduction conditions, the Co_3O_4/Cdots and Co_3O_4/N-doped Cdots catalysts increased the reduction temperature of Co_3O_4 to CoO and metallic Co, and Co (fcc) is the predominant form of metallic Co formed. However, when N-doped Cdots were used as both support and reducing agents, Co_3O_4 was reduced to both Co (fcc) and Co (hcp). The increase in reduction temperature of Co_3O_4 on Co_3O_4/Cdots and Co_3O_4/N-doped Cdots suggest the presence of strong metal to support interactions (SMSIs) between Co_3O_4 and functionalized Cdots. Further studies on the activity and selectivity of these prepared catalysts will be conducted under F-T reaction process.

DEDICATION

To my mother Lizzie Mokoloko and my grandmother Pulane Nthapo

"The fear of the Lord is the beginning of wisdom" Psalms 111:10 (NKJV)

ACKNOWLEDGEMENTS

I would like to express my profound gratitude to my supervisor Prof Neil J. Coville for giving me the opportunity to work with him and for the support he has given me throughout this journey.

I would like to thank my co-supervisor Dr Roy P. Forbes for his valued contribution in this project. Your guidance and support did not go unnoticed.

A special thank you goes to Dr Rudolph Erasmus for his assistance with photoluminescence measurements, and Dr James Wesley-Smith for helping me with TEM images. I would also like to thank the CSIR NMISA for assisting with XPS analysis. Your assistance is greatly appreciated.

I would like to thank Prof Alexandra Ziegler and Prof Dave Billing for an opportunity to use the electron microscopy and XRD instruments.

I would like to thank the School of Chemical Engineering at UCT for hosting me in their laboratory, more especially Mr Moritz Wolf for taking his time to go through the catalyst preparation process with me. Thank you very much.

I would like to thank Dr Manoko Maubane, Dr Tumelo Phaahlamohlaka, Dr William Dlamini, Dr Farai Dziike, Dr Boitumelo Matsoso and Dr Bridget Mutuma for their assistance inside and outside the laboratory. Thank you for your availability every time I needed your assistance. You are greatly appreciated.

A huge thank you to the CATOMAT research group, especially the following people: Mr Thomas Mongwe, Mr Victor Mashindi, Ms Alice Magubane, Ms Puledi Mphago and Mr Orlette Mkhari. Thank you for your participation and inputs during our weekly meetings, and for making this MSc journey fun.

This project would not have been possible if it wasn't for the financial assistance from the DST-NRF Centre of Excellence in Catalysis (*c**hange).

A special thanks goes to the all the members of Grace Bible Church Braamfontein's Ministry of Helps. Thank you for your prayers and support.

I would like to thank my relatives Mr and Mrs Maropeng. Thank you for your unfailing support and encouragement throughout my studies. Your prayers are what have kept me going till thus far. I love you both very much.

To my mother Lizzie Mokoloko, my grandmother Pulane Nthapo, my siblings Kamohelo Nthapo and Palesa Mokoloko, ke a leboha ka ho mpha lerato la lona le sa fetoheng. Ke a leboha ka tshehetso ya lona ya ka mehla. Ke seo ke leng sona kajeno ka lebaka la lona. Ke le rata ka pelo ya ka yohle.

Lastly but not least, to my Lord and Saviour King Jesus: thank you for the strength you have given me throughout this journey. Thank you for keeping my dreams alive and for the many mountains and many battles You have fought and won on my behalf. I'm here because of You. This journey, the people I have met, the places I have been and all the achievements I have had would not have been possible if it wasn't for Your unfailing grace. Thank You!

"The fear of the Lord is the beginning of wisdom" Psalms 111:10 (NKJV)

PRESENTATIONS

"The Effect of Metal to Support Interactions between a Cobalt catalyst and Carbon Dots (Cdots) in Cobalt Fischer-Tropsch Catalysts" (**Oral Presentation**), DST center of excellence in catalysis (*c*change*) meeting, Wits and UCT- Johannesburg (Gauteng), May 2016.

"The Effect of Metal to Support Interactions between a Cobalt catalyst and Carbon Dots (Cdots) in Cobalt Fischer-Tropsch Catalysts" (**Oral Presentation**), Syngas meeting, DST center of excellence in catalysis (*c*change*) Symposium, Drakensbug (Kwa-Zulu Natal), November 2016.

"The Effect of Metal to Support Interactions between a Cobalt catalyst and Carbon Dots (Cdots) in Cobalt Fischer-Tropsch Catalysts" (**Oral Presentation**), Wits and Sasol meeting, Sasol-Sasolburg (Free State), August 2016.

"The Effect of Metal to Support Interactions between a Cobalt catalyst and Carbon Dots (Cdots) in Cobalt Fischer-Tropsch Catalysts" (**Poster Presentation**), Catalysis for Fuels: Faraday Discussion, Cape-Town (Western Cape), January 2017.

"*N*-doped Cdots as potential support for cobalt-based catalysts used in Fischer-Tropsch reaction" (**Oral Presentation**), 7th annual South African Nanotechnology Initative Nanoscience Young Researchers Symposium (SANi-NYRS), Tshwane University of Technology (TUT), Pretoria (Gauteng), October 2017.

"Carbon dots: A new support material for use in the synthesis of transportation fuel" (**Oral Presentation**), 8th annual Cross-Faculty Postgraduate Symposium, Wits University, Johannesburg (Gauteng), October 2017.

"Inverse Co-based Fischer-Tropsch catalysts: Studies of metal to support interactions using functionalized Cdots supports" (**Oral Presentation**), Catalysis Society of South Africa (CATSA) Annual conference, Pilanesburg (North West), November 2017.

AWARDS

3rd place for best Oral presentation in the Faculty of Science, Wits Cross-Faculty Postgraduate Symposium (October 2017).

PUBLICATIONS

Hutchings, G., Bowker, M., Catlow, R., Nyathi, T., Abdullah, I., Claeys, M., Coville, N., Roldan, A., van Helden, P., Fischer, N., van Steen, E., Jewell, L., **Mokoloko, L.**, Bahnemann, D., Neurock, M., Kapteijn, F., Iglesia, E., Gibson, P., Holt, K., Domen, K. & Gupta, A. K. Novel photocatalysts: general discussion. *Faraday Discuss.* **197**, 533-546 (2017).

RESEARCH VISIT

Visited the School of Engineering at the University of Cape Town, in March 2017.

TABLE OF CONTENTS

DECLARATION i
ABSTRACT ii
DEDICATION iii
ACKNOWLEDGEMENTS iv
PRESENTATIONS vi
AWARDS vii
PUBLICATIONS vii
RESEARCH VISIT vii
TABLE OF CONTENTS viii
LIST OF FIGURES xi
LIST OF TABLES xiii
LIST OF SCHEMES xiii
LIST OF ABBREVIATIONS xiv
LIST OF CHEMICAL FORMULAS xv
CHAPTER 1: INTRODUCTION AND MOTIVATION 1
1.1 Introduction 1
1.2 Motivation 2
1.3 Aim and objectives 3
1.4 Research questions 4
1.5 Dissertation outline 4
References 5
CHAPTER 2: LITERATURE REVIEW 9
2.1 Introduction: Carbon dots 9
2.1.1 Synthesis of Cdots 10
2.1.2 Optical properties 13
2.1.3 Applications 14
2.2 Introduction: Fischer-Tropsch Process 16
2.2.1 The F-T process chemistry 16
2.2.2 F-T catalysts 18

2.2.3 Co-based F-T reactions....18
2.2.4 MSIs and inverse-supported catalysts....19
References....22
CHAPTER 3: SYNTHESIS AND CHARACTERIZATION OF CDOTS AND N-DOPED CDOTS....32
3.1 Introduction....32
3.2 Synthesis of Cdots and N-doped Cdots....33
3.3 Characterization techniques....37
3.3.1 X-ray diffraction: XRD....37
3.3.2 Transmission electron microscopy: TEM....37
3.3.3 Scanning electron microscopy: SEM....37
3.3.4 Raman spectroscopy....37
3.3.5 Fourier transform infrared spectroscopy: FT-IR....38
3.3.6 X-ray photoelectron spectroscopy: XPS....38
3.3.7 Thermogravimetric analysis: TGA....38
3.3.8 Photoluminescent: PL....38
3.3.9 Ultra-violet-visible: UV-vis....38
3.3.10 Product yield calculation....39
3.4 Results and Discussions....40
3.4.1 Synthesis....40
3.4.2 Structural properties....42
3.4.3 Chemical properties....47
3.4.4 Thermal stability: Thermal gravimetric analysis (TGA)....55
3.4.5 Optical properties....58
3.5 Conclusion....59
References....61
CHAPTER 4: SYNTHESIS AND CHARACTERIZATION OF SPINEL Cobalt (II,III) oxide (Co_3O_4) NANOPARTICLES....66
4.1 Introduction....66
4.2.1 Synthesis of spinel Co_3O_4 from the ammonia assisted “benzyl alcohol route”....66
4.2.1.1 Benzyl alcohol chemistry....67
4.2.2 Experimental procedures....70
4.2.3 Characterization....71
4.2.3.1 Temperature Programmed Reduction: TPR....71

4.2.4 Results and Discussions 72
4.2.4.1 Synthesis results 72
4.2.4.2 Physical properties 73
4.2.4.3 Chemical properties 75
4.2.4.4 Thermal reduction studies 76
4.3 Conclusion 76
References 78
CHAPTER 5: Synthesis and characterization of Co_3O_4/Cdots 81
5.1 Introduction 81
5.2 Experimental procedure 81
5.3 Characterization techniques 81
5.3.1 *In-situ* X-ray diffraction (XRD) 82
5.4 Results and discussions 82
5.4.1 X-ray diffraction: XRD 82
5.4.2 Transmission Electron Microscopy: TEM 83
5.4.4 Thermal gravimetric analysis: TGA 84
5.4.5 Fourier transform infrared spectroscopy: FT-IR spectroscopy 86
5.4.6 Temperature Programmed Reduction: TPR 86
5.4.7 *In-situ* X-ray diffraction (XRD) 88
5.4.8 The effect of metal to support interaction 91
5.4.9 Reduction properties of N-doped Cdots-1 91
5.5 Conclusion 94
References 95
CHAPTER 6: GENERAL CONCLUSIONS AND RECOMMENDATIONS 98
6.1 Conclusions 98
6.2 Recommendations 99
SUPPLEMENTARY INFORMATION 100

LIST OF FIGURES

CHAPTER 1

Figure 1.1: Simple cartoon illustrating conventional, core-shell and inverse methods to make catalysts.....2

CHAPTER 2

Figure 2.1: Proposed structure of a) CQDs and b) GQDs showing the ordering of layers of sp^2 type carbon (adopted from Jelinek, 2017)[3].....9

Figure 2.2: A simple schematic representation of the "top-down" and "bottom-up" synthesis approaches for the synthesis of Cdots (adopted from De and Karak, 2017)[19].....10

Figure 2.3: Cartoon illustrating surface change of Cdots after functionalization and passivation (after Baker and Baker, 2010)[5].....11

CHAPTER 3

Figure 3.1: Sample preparation for microwave-assisted synthesis.....34

Figure 3.2: a) Microwave rotor set-up before synthesis, and b) microwave oven.....34

Figure 3.3: Purification of the product by centrifugation.....35

Figure 3.4: Cdots product a) before and b) after drying.....35

Figure 3.5: a) Separation of sucrose Cdots from unreacted oleic acid, and b) Sucroce Cdots dialysis set-up.....36

Figure 3.6: XRD patterns of a) Cdots-1, b) Cdots-2, c) N-doped Cdots-1, and d) N-doped Cdots-2.....43

Figure 3.7: a) FT-IR and b) PL results for chitosan and N-doped Cdots-1.....45

Figure 3.8: Low resolution SEM images of a) Cdots-1, as well as b) N-doped Cdots-1.....45

Figure 3.9: a) TEM image with an inserted particle size distribution histogram and a normal distribution curve of Cdots-1, and b) a low resolution TEM image of N-doped Cdots-1. The red circles highlight Cdots that can be seen from the grid.....46

Figure 3.10: Raman spectra of a) Cdots-1, b) Cdots-2, c) N-doped Cdots-1, and d) N-doped Cdots-2.....47

Figure 3.11: FT-IR spectra of a) Cdots and b) N-doped Cdots.....48

Figure 3.12: XPS spectra of (a) Cdots-1, (b) Cdots-2, (c) N-doped Cdots-1 and (d) N-doped Cdots-2.....49

Figure 3.13: Expanded a) C1s and b) O1s survey XPS spectra of Cdots-1.....51

Figure 3.14: Expanded a) C1s and b) O1s survey XPS spectra of Cdots-2.....52

Figure 3.15: A structure showing the possible position of surface functional groups on Cdots as determined by C1s and O1s XPS survey deconvolution (after Ma *et al.*, 2017)[29].....52

Figure 3.16: Expanded a) C1s, b) O1s and c) N1s survey XPS spectra of N-doped Cdots-1 .53

Figure 3.17: Expanded a) C1s, b) O1s and c) N1s survey XPS spectra of N-doped Cdots-2 .54

Figure 3.18: A structure showing the possible position of surface functional groups on N-doped Cdots as determined by N1s XPS survey deconvolution (adopted from Zhang *et al.*, 2012)[30] 55

Figure 3.19: TG- DTG graphs of a) Cdots-1 and b) Cdots-2.....57

Figure 3.20: TG- DTG graphs of a) N-doped Cdots-1 and b) N-doped Cdots-2.....57

Figure 3.21: a) PL emission, the dotted lines represent the maximum intensity peak position, b) UV-vis absorption and inserted Cdots emission before and after 365 nm UV light irradiation.....59

CHAPTER 4

Figure 4.1: Experimental set-up for Co_3O_4 nanoparticles synthesis using a hotplate 71

Figure 4.2: XRD patterns of spinel Co_3O_4 nanoparticles highlighting the peak positions of the Co_3O_4 phase 73

Figure 4.3: TEM image with an inserted particle size distribution histogram of Co_3O_4 nanocubes synthesized by method a) 1*, b) $2^{\#}$, c) $3^{\#}$ and d) $4^{\#}$. 74

Figure 4.4: FT-IR spectra of a) spinel Co_3O_4 nanoparticles at b) Cobalt acetate c) benzyl alcohol.....75

Figure 4.5: TPR profile of crystalline Co_3O_4 nanoparticles 76

CHAPTER 5

Figure 5.1: XRD pattern of Co_3O_4/Cdots-1and Co_3O_4/N-doped Cdots-1 83

Figure 5.2: TEM image of Co_3O_4/Cdots-1 83

Figure 5.3: a) The TG and b) DTG thermograms of Cdots-1 and Co_3O_4/Cdots-1 85

Figure 5.4: a) The TG and b) DTG thermograms of N-doped Cdots-1 and Co_3O_4/N-doped Cdots-1.....85

Figure 5.5: FT-IR spectra of a) Co_3O_4, Cdots-1 and Co_3O_4/ Cdots-1, and b) Co_3O_4, N-doped Cdots-1 and Co_3O_4/ N-doped Cdots-1 86

Figure 5.6: TPR profile of Co_3O_4, Co_3O_4/ Cdots-1and Co_3O_4/ N-doped Cdots-1.....88

Figure 5.7: In-situ XRD pattern of a) Co_3O_4/Cdots-1 under H_2 reducing conditions, b) Co_3O_4/N-doped Cdots-1 under H_2 reducing conditions, and c) Co_3O_4/N-doped Cdots-1 under inert (N_2) conditions..... 89-91

Figure 5.8: a) TEM and b) Raman spectrum of the product obtained after annealing N-doped Cdots-1 at 500 °C under Argon gas 93

Figure S3.1: XRD patterns of a) ascorbic acid, b) sucrose, c) chitosan, and d) urea 100

Figure S3.2: Low resolution SEM images of a) Cdots-2, and b) N-doped Cdots-2. The dotted cycles highlights the Cdots clusters 101

Figure S5.1: a) The XRD pattern, b) FT-IR spectrum, c) PL spectra, and d) TG-DTG thermogram of the annealed N-doped Cdots-1 sample.....101

LIST OF TABLES

CHAPTER 3

Table 3.1: Cdots and N-doped Cdots microwave-assisted synthesis conditions 33

Table 3.2a): Percentage Atomic abundance in each sample 50

Table 3.2b): Peak positions of C1s bonding states 50

Table 3.2c): Peak positions of O1s bonding states 50

Table 3.2d): Peak positions of nitrogen bonding states 51

Table 3.3: PL and UV-vis peak positions 59

CHAPTER 4

Table 4.1: Summarized synthesis results of Co_3O_4 nanoparticles with different crystallite sizes 72

Table S3.2a): Relative concentrations of carbon bonding states 102

Table S3.2b): Relative concentrations of oxygen bonding states 102

Table S3.2c): Relative concentrations of nitrogen bonding states 102

LIST OF SCHEMES

CHAPTER 3

Scheme 3.1: A simple reaction scheme for the Cdots synthesis using ascorbic acid as a carbon source 40

Scheme 3.2: A simple reaction scheme for the Cdots synthesis using sucrose as a carbon source 41

Scheme 3.3: A simple reaction scheme for the N-doped Cdots synthesis using chitosan as both a carbon and nitrogen source 41

Scheme 3.4: A simple reaction scheme for N-doped Cdots synthesis using ascorbic acid as both a carbon source and urea as a nitrogen source 42

CHAPTER 4

Scheme 4.1: Benzyl alcohol and the four resonance structures of benzylic carbocation 68

LIST OF ABBREVIATIONS

AC: Activated carbon

BTL: Biomass-to-liquid

ca: Circa (approximately)

Cdots: Carbon dots

CNT: Carbon nanotubes

CQD: Carbon quantum dots

CSs: Carbon spheres

CTL: Coal-to-liquid

CVD: Chemical vapour deposition

DTG: Derivative thermal gravimetric

EDA: ethylenediamine

fcc: Face-centred cubic

F-T: Fischer-Tropsch

FT-IR: Fourier transform infrared spectroscopy

GHG: greenhouse

GO: graphene oxide

GQD: graphene quantum dots

GTL: Gas-to-liquid

HCSs: Hollow carbon spheres

hcp: hexagonal close packed

hrs: Hours

min: minutes

MSIs: Metal to support interactions

N-doped Cdots: Nitrogen-doped carbon dots

Nd:YAG: Q-switched neodymium-doped yttrium aluminium garnet

NIR: Near infrared

No.: Number

PEG: polyethylene glycol

PEG_{1500N} : bis(3-aminopropyl) terminated poly(ethylene glycol)

PL: Photoluminescence

SEM: Scanning electron microscopy

SWCNTs: single-walled carbon nanotubes

Syngas: synthesis gas

TEM: Transmission electron microscopy

TEOS: tetraethyl orthosilicate

TGA: Thermal gravimetric analysis

TOAB: Tetraoctylammonium bromide

TPR: Temperature programmed reduction

TTDDA: 4, 7, 10-trioxa-1,13-tridecanediamine

UV-vis: Ultraviolet to visible

WGS: Water gas shift

wt%: weight percentage

XPS: X-ray photoelectron spectroscopy

XRD: X-ray diffraction

LIST OF CHEMICAL FORMULAS

Al_2O_3: Alumina

Ag: Silver

Ar: Argon

CO_2: Carbon dioxide

CO: Carbon monoxide

Co: Cobalt

CoO: Cobalt (II) Oxide

Co_3O_4: Cobalt (II, III) Oxide

$Co(OAc)_2.4H_2O$: hydrated cobalt acetate

CuO: Copper oxide

Fe: Iron

HNO_3: nitric acid

H_2O: water

H_2SO_4: sulfuric acid

H_2: hydrogen gas

MnO_2: Manganese oxide

Ni: Nickel

N_2: Nitrogen gas

O: Oxygen

P: Phosphorus

Pd: Palladium

Ru: Ruthenium

SiO_2: Silica

TiO_2: Titania

ZnO: Zinc oxide

CHAPTER 1: INTRODUCTION AND MOTIVATION

1.1 Introduction

According to the International Energy Outlook (2017), the world's liquid fuel consumption may increase by 31 % between 2015-2040, with 55 % of this used for transport[1]. Crude oil has been the main contributor for transportation fuel productions for approximately 200 years[2]. However, population and industrial growth is outstripping the world's crude oil reserves[3]. In addition, the transportation sector is one of the biggest contributors of greenhouse gas (GHG) emissions worldwide[1,4,5]. The fear of the eventual end to crude oil reserves, as well as the strict policies put in place for GHG emitters has led to an increase in research on fuel energy sources that are renewable and environmentally friendly[4–6]. The Fischer-Tropsch (F-T) reaction process is one of the most studied technologies in that regard[7–10]. The F-T reaction process is based on the catalytic conversion of syngas (carbon dioxide and hydrogen) into fuels and a range of other chamicals[4–13]. This process is considered as a more environmentally friendly alternative for fuel production due to the utilization of naturally abundant and renewable resources such as natural gas, coal and biomass for syngas production, and low emission of GHG such as CO_2[9].

The syngas conversion reaction takes place on the surface of a catalyst[10]. Most commonly used F-T catalysts both industrially and academically, are cobalt (Co) and iron (Fe)[10,14,15]. Co based catalysts are preferred because of their high selectivity towards long chain hydrocarbons compared to Fe[7,16,17]. One of the ways to improve Co catalyst performance is by dispersing catalysts nanoparticles on a support material such as an inorganic oxide or shaped carbon material[7,15,18]. Dispersing small Co nanoparticles on a support helps maximise the number of active surface catalytic species, and hence improves syngas conversion in the F-T reaction[15,17,19].

Metal to support interactions (MSIs) also play a significant role in the Co catalyst performance[20–22]. Inorganic oxides such as silica (SiO_2), alumina (Al_2O_3), titania (TiO_2) and zeolites have been used as Co-based F-T catalysts support[20–22]. These supports are known to form strong metal to support interactions (MSIs) with the Co catalysts. Cobalt nanoparticles with strong MSIs are resistant to sintering, however, high reduction temperatures are required to reduce cobalt oxide (Co_3O_4) to the catalytically active Co[14,17,20]. Carbon nanomaterials such as graphene, carbon nanotubes (CNTs), carbon spheres (CSs) and hollow-carbon spheres (HCSs) have also been used as Co metal support due to their high surface area,

chemical stability, and electron conductivity[18,23]. In comparison to inorganic oxides, carbon nanomaterials are more chemically inert, and hence display weak interactions with metal catalysts[14,18]. As a result, the reduction of Co_3O_4 to Co happens at lower temperatures. In addition the catalyst can be recovered by simply burning off the carbon support in the presence of oxygen[14,18]. However, the metal catalyst nanoparticles can easily sinter due to the weak MSIs, leading to deactivation of catalytic properties. Therefore oxygen and/or nitrogen functional groups are normally introduced on the carbon surface to enhance the MSI, which consequently helps improve metal catalyst dispersion and overall activity during F-T reaction[14,17,18].

1.2 Motivation

Different supported catalyst models have been developed for dispersing the metal catalyst nanoparticles and to study the metal to support interactions (MSIs)[18,17]. These are the conventional method, core-shell method, and the inverse method as illustrated in **Figure 1.1** below[17,24]. In the conventional method, metal catalysts nanoparticles are dispersed on top of a large support bed[12,17,24]. The core-shell method can be used to encapsulate metal catalysts nanoparticles on the inside of a hollow support, while in the inverse method the metal catalyst surface is decorated with small amounts of the support[12,17,24]. All three of these support models have been explored with different types of inorganic oxides[12,17,20,21]. For carbon based nanomaterials, graphene, CNTs and CSs have been used for designing the conventional catalyst support, and HCSs have been used to achieve the core-shell method[18,23,25]. So far, to the best of our knowledge, there are no literature reports on any carbon allotrope being used to investigate the inverse supported catalyst method. In this study, a new type of carbon nanomaterial known as carbon dots (Cdots) were used for the first time to disperse cobalt (II,III) oxide (Co_3O_4) on carbon to make a Co-based F-T catalyst.

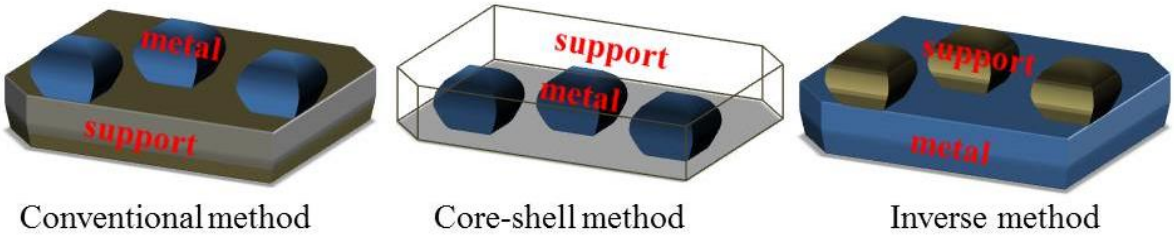


Figure 1.1: Simple cartoon illustrating conventional, core-shell and inverse methods to make catalysts

Carbon dots (Cdots) are surface functionalized carbon nanomaterials with particle sizes less than 10 nm[26]. They were discovered in 2004, and have since been explored for their unique physicochemical and optical properties. These include their tuneable photoluminescent properties, high photostability, water solubility and low toxicity[26–28]. As a result, Cdots have been used in bioimaging, biosensing, photocatalysis, solar cells, semiconductors, *etc.*[26]. Most of these applications are based on the material's photoluminescence properties. Other potential uses of Cdots remains relatively unexplored as compared to the other carbon based nanomaterials such as graphene, fullerene, carbon nanotubes (CNTs) and carbon spheres (CSs) *etc*[29]. A few reports have shown that Cdots and N-doped Cdots can reduce metal salts and also act as stabilizing agents for metal nanoparticle such as manganese oxide (MnO_2), silver (Ag) and palladium (Pd)[29–31]. These properties may also be advantageous for Co-based F-T catalysts, provide further the motivation for the study.

1.3 Aim and objectives

The main aim of this study was to introduce Cdots and N-doped Cdots as potential supports to make an inverse Co based F-T catalyst, and to study and compare the effect of MSIs between Co_3O_4/Cdots and Co_3O_4/N-doped Cdots on the reducibility properties of inverse Co_3O_4/Cdots and Co_3O_4/N-doped Cdots in the reduction of Co_3O_4 to metallic Co.

The following are the objectives of the study:

1. Synthesize Cdots and N-doped Cdots using microwave-assisted reactions and characterize their physical and chemical properties. The thermal stability of Cdots has not been well studied in the literature, as most of their applications take place under relatively mild conditions. In this study, Thermal gravimetric analysis (TGA) was used to study the thermal stability of Cdots.
2. Study the effect of annealing on the chemical and physical properties of the prepared Cdots.
3. Synthesize and characterize Co_3O_4 nanoparticle using the "benzyl alcohol route".
4. Prepare and characterize inverse Co_3O_4/ Cdots and Co_3O_4/ N-doped Cdots.
5. Apply an *in-situ* X-ray diffraction (XRD) technique to study Co_3O_4/ Cdots and Co_3O_4/ N-doped Cdots. In particular to i) study the effect of the MSIs on the reduction of Co_3O_4 to Co fcc and/or hcp phase/s, and ii) investigate the reducing properties of Cdots and N-doped Cdots by comparing the reduction of Co_3O_4 to Co fcc and/or hcp phase/s under hydrogen (as a reducing agent) and under inert conditions.

1.4 Research questions

The project aimed to answer the following question:

Do the Co_3O_4 /Cdots and Co_3O_4 /N-doped Cdots catalysts show potential as F-T catalysts?

- Are Cdots and N-doped Cdots thermally stable under reducing conditions?
- Is there a significant difference between the reducibility of the metal oxide catalysts when different functionalized Cdots are used?
- Will the Cdots and N-doped Cdots act as reducing and stabilizing agent for Co_3O_4 and metallic Co?

1.5 Dissertation outline

This dissertation is broken down into the following chapters:

Chapter 1: Discusses the motivation, aim, objectives, as well as research questions for the study.

Chapter 2: This chapter gives an insight into the synthesis (including microwave irradiation syntheses), characteristics and applications of Cdots as reported in the literature. This chapter ends with a discussion of basic concepts of the F-T process (more especially Co-based F-T process) as well as more detail on the application of carbon nanomaterials as F-T catalyst supports. The influence of MSIs on the catalysts performance will also be discussed in more details.

Chapter 3: This will give an overview on the synthesis and characterization of different functionalized Cdots.

Chapter 4: This chapter will look at the synthesis and characterization of Co_3O_4 nanoparticles.

Chapter 5: The chapter discusses the synthesis and characterizations inverse Co_3O_4/Cdots and Co_3O_4/N-doped Cdots supported catalysts, as well as the study of MSIs using *in-situ* XRD.

Chapter 6: This chapter will give a conclusion and recommendations for future studies.

References

1. EIA. International Energy Outlook 2017 Overview. *U.S. Energy Inf. Adm.* **IEO2017,** 143–934 (2017).

2. Phaahlamohlaka, T. N. Synthesis of carbon nanofibers and their subsequent use as catalyst supports for Fischer- Tropsch synthesis. MSc Dissertation (University of the Witwatersrand, Johannesburg, 2013).

3. Sorrell, S., Speirs, J., Bentley, R., Brandt, A. & Miller, R. Global oil depletion: A review of the evidence. *Energy Policy.* **38,** 5290–5295 (2010).

4. van Vliet, O. P. R., Faaij, A. P. C. & Turkenburg, W. C. Fischer – Tropsch diesel production in a well-to-wheel perspective : A carbon , energy flow and cost analysis. *Energy Convers. Manag.* **50,** 855–876 (2009).

5. Sauciuc, A., Potetz, A., Weber, G., Rauch, R., Hofbauer, H. & Dumitrescu, L. Synthetic diesel from biomass by Fischer-Tropsch synthesis. In: International conference of renewable energies and power quality (ICREPQ '11). Spain: Las Palmas de Gran Canaria, 2–7 (2011).

6. Hu, J., Yu, F. & Lu, Y. Application of Fischer–Tropsch Synthesis in Biomass to Liquid Conversion. *Catalysts.* **2,** 303–326 (2012).

7. Xie, J., Yang, J., Dugulan, A. L., Holmen, A., Chen, D., Jong, K. P. D. & Louwerse, M. J. Size and Promoter Effects in Supported Iron Fischer − Tropsch Catalysts: Insights from Experiment and Theory. *ACS Catal.* **6**, 3147–3157 (2016).

8. Dry, M. E. The Fischer – Tropsch process : 1950 – 2000. *Cat. Today* **71,** 227–241 (2002).

9. Ail, S. S. & Dasappa, S. Biomass to liquid transportation fuel via Fischer Tropsch synthesis – Technology review and current scenario. *Renewable and Sustainable Energy Reviews* **58,** 267–286 (2016).

10. Dry, M. E. High quality diesel via the Fischer – Tropsch process – a review. *J Chem Technol Biotechnol*. **77,** 43–50 (2002).

11. Leckel, D. Low-Pressure Hydrocracking of Coal-Derived Fischer – Tropsch Waxes to Diesel. *Energy Fuels* **21,** 1425–1431 (2007).

12. Mogorosi, R. P. Metal-support interaction on Fe-based Fischer-Tropsch catalysts. PhD Thesis (University of Cape Town, Cape Town, 2012).

13. Kreutz, T. G., Larson, E. D., Liu, G. & Williams, R. H. Fischer-Tropsch Fuels from Coal and Biomass. 25th Annual International Pittsburgh Coal Conference (2008).

14. Xiong, H., Motchelaho, M. A. M., Moyo, M., Jewell, L. L. & Coville, N. J. Correlating the preparation and performance of cobalt catalysts supported on carbon nanotubes and carbon spheres in the Fischer-Tropsch synthesis. *J. Catal.* **278,** 26–40 (2011).

15. Soled, S. L., Iglesia, E., Fiato, R. A., Baumgartner, J. E., Vroman, H. & Miseo, S. Control of metal dispersion and structure by changes in the solid-state chemistry of supported cobalt Fischer – Tropsch catalysts. *Topics in Catalysis*. **26,** 101–109 (2003).

16. Tsakoumis, N. E., Rønning, M., Borg, Ø., Rytter, E. & Holmen, A. Deactivation of cobalt based Fischer – Tropsch catalysts : A review. *Catal. Today.* **154,** 162–182 (2010).

17. Macheli, L. Co_3O_4 -Nanocubes modified with TEOS as models to study support interactions in cobalt-based Fischer-Tropsch catalysts. MSc Dissertation (University of Cape Town, Cape Town, 2014).

18. Xiong, H., Jewell, L. L. & Coville, N. J. Shaped Carbons As Supports for the Catalytic Conversion of Syngas to Clean Fuels. *ACS Catal.* **5,** 2640–2658 (2015).

19. Moyo, M. Cobalt and Iron Supported on Carbon Spheres Catalysts for Fischer Tropsch synthesis. PhD Thesis (University of the Witwatersrand, Johannesburg, 2012).

20. van Heerden, T. & van Steen, E. Metal – support interaction on cobalt based FT catalysts – a DFT study of model inverse catalysts. *Faraday Discuss.* **197,** 87–99 (2017).

21. Storsæter, S., Tøtdal, B., Walmsley, J. C., Tanem, B. S. & Holmen, A. Characterization of alumina-, silica-, and titania-supported cobalt Fischer-Tropsch catalysts. *J. Catal.* **236,** 139–152 (2005).

22. Kim, J. C., Lee, S., Cho, K., Na, K., Lee, C. & Ryoo, R. Mesoporous MFI zeolite nanosponge supporting cobalt nanoparticles as a Fischer-Tropsch catalyst with high yield of branched hydrocarbons in the gasoline range. *ACS Catal.* **4,** 3919–3927 (2014).

23. Karimi, S., Tavasoli, A., Mortazavi, Y. & Karimi, A. Cobalt supported on Graphene - A promising novel Fischer-Tropsch synthesis catalyst. *Appl. Catal. A Gen.* **499,** 188–196 (2015).

24. Rodríguez, J. A. & Hrbek, J. Inverse oxide / metal catalysts : A versatile approach for activity tests and mechanistic studies. *Surf. Sci.* **604,** 241–244 (2010).

25. Phaahlamohlaka, T. N., Kumi, D. O., Dlamini, M. W., Forbes, R., Jewell, L. L., Billing, D. G. & Coville, N. J. Effects of Co and Ru Intimacy in Fischer − Tropsch Catalysts Using Hollow Carbon Sphere Supports : Assessment of the Hydrogen Spillover Processes. *ACS Catal.***7,** 1568–1578 (2017).

26. Jelinek, R. *Carbon Quantum Dots*.1–129 (Springer International Publishing Switzerland , 2017)

27. Baker, S. N. & Baker, G. A. Luminescent Carbon Nanodots : Emergent Nanolights. *Angew. Chem. Int. Ed*. **49**, 6726–6744 (2010).

28. Li, X., Wang, H., Shimizu, Y., Pyatenko, A., Kawaguchi, K. & Koshizaku, N. Preparation of carbon quantum dots with tunable photoluminescence by rapid laser passivation in ordinary organic solvents. *Chem. Commun.***47,** 932–934 (2011).

29. Dey, D., Bhattacharya, T., Majumdar, B., Mandani, S., Sharma, B. & Sarma, T.K. Carbon dot reduced palladium nanoparticles as active catalysts for carbon–carbon bond formation. *Dalt. Trans.* **42,** 13821–13825 (2013).

30. Unnikrishnan, B. Wu, C. W., Chen, I. W. P., Chang, H. T., Lin, C. H. & Haung, C. C. Carbon Dot-Mediated Synthesis of Manganese Oxide Decorated Graphene Nanosheets for Supercapacitor Application. *ACS Sustain. Chem. Eng.* **4,** 3008–3016 (2016).

31. Liu, T., Dong, J. X., Liu, S. G., Li, N., Lin, S. M., Fan, Y. Z., Lei, J. L., Luo, H. Q. & Li, N. B. Carbon quantum dots prepared with polyethyleneimine as both reducing agent and stabilizer for synthesis of Ag/CQDs composite for Hg^{2+} ions detection. *J. Hazard. Mater*. **322,** 430–436 (2017).

CHAPTER 2: LITERATURE REVIEW

2.1 Introduction: Carbon dots

Carbon dots (abbreviated Cdots[1,2], also called carbon quantum dots, carbon nanodots, fluorescent carbon dots *etc.*) are carbon-based quantum dots with particle sizes less than 10 nm[3–5]. They were discovered serendipitously by Xu *et al.* in 2004 as by-products in the synthesis of single-walled carbon nanotubes (SWCNTs) by arc discharge of soot[6]. During purification by electrophoresis, the researchers noticed that the product separated into 3 distinct types of nanoparticles including Cdots, which were recognized by their high luminescence property[3–7]. Later in 2006, Sun *et al.* produced Cdots from laser ablation from a mixture of graphite powder and cement[8]. Since then, numerous studies have been made aiming at their synthesis, characterization and application, especially for scientific research that requires fluorescing nanomaterials[3,7,9,10].

Cdots consist of discrete and quasi-spherical nanostructures that are usually decorated with oxygen (e.g. carboxyl and hydroxyl) and/or nitrogen (e.g. amino, for N-doped Cdots) surface functional groups [9–14]. Cdots are classified into two categories based on their degree of crystallinity (or graphitic nature), namely carbon quantum dots (CQDs) and graphene quantum dots(GQDs)[3,10,15,16]. CQD refers to Cdots with sphere-like shape and a core structure consisting of predominantly disordered layers of carbon with sp^2 hybridization. GQDs are a more graphitic type of Cdots with limited sp^2 type carbon layers, and an overall disk-like shape as shown in **Figure 2.1** below[3,9]. Since CQDs and GQDs have relatively similar morphologies, they have also shown similar photoluminescent (PL) properties[3].

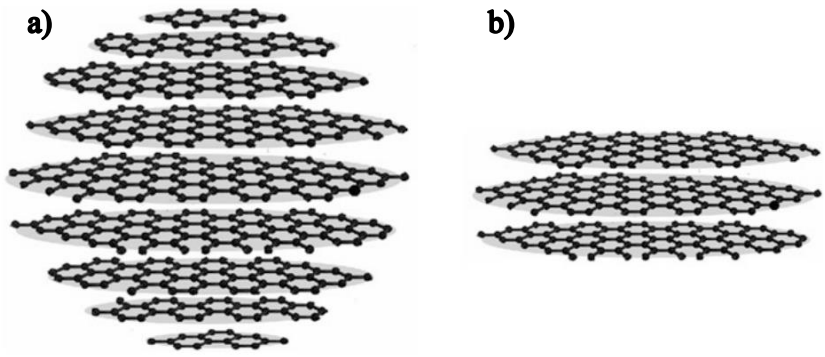


Figure 2.1: Proposed structure of a) CQDs and b) GQDs showing the ordering of layers of sp^2 type carbon (adopted from Jelinek, 2017)[3]

2.1.1 Synthesis of Cdots

Since 2006, a variety of synthesis procedures have been developed and modified for the synthesis of Cdots[7,9,10,12,17]. More importantly, the large scale synthesis of Cdots with tuneable physical, optical and electronic properties has been the motivation for the development and modification of Cdots synthesis[9,18]. Cdots synthesis methods have been divided into two different categories called the "top-down" and "bottom-up" methods[19], summarised by **Figure 2.2**. In the "top-down" method, large carbon nanomaterials such as graphite, carbon nanotubes (CNTs), carbon fiber and activated carbon (AC) are physically or chemically broken down into smaller Cdots nanoparticles[6,8,20,21]. Traditionally, chemical oxidation, electrochemical oxidation, laser ablation and arc discharge have been utilized in "top-down" methods for Cdots synthesis[21–23].

In the "bottom-up" method, smaller carbon precursors are built up into Cdots. Carbon precursors can vary from carbohydrates such as sucrose, glucose and starch, to polymers like (1,4)-2-amino-2-desoxy- beta-D-glucan (also known as chitosan) and polyethylene glycol (PEG), and food products including orange peels, watermelon peels, milk, eggs and coffee[5,7,17,20–24]. These precursors are converted to Cdots via methods such as hydrothermal/solvothermal methods and microwave irradiation[5,7,17,20–24]. The "top-down" method usually produces GQDs, while the "bottom-up" method produces CQDs[10,16]. Usually, the "bottom-up" method provides better morphology and size control of resulting Cdots, as well as the ease of incorporating a dopant (nitrogen, sulphur, silica, phosphorus *etc.*) or surface passivating agents in the reaction[15].

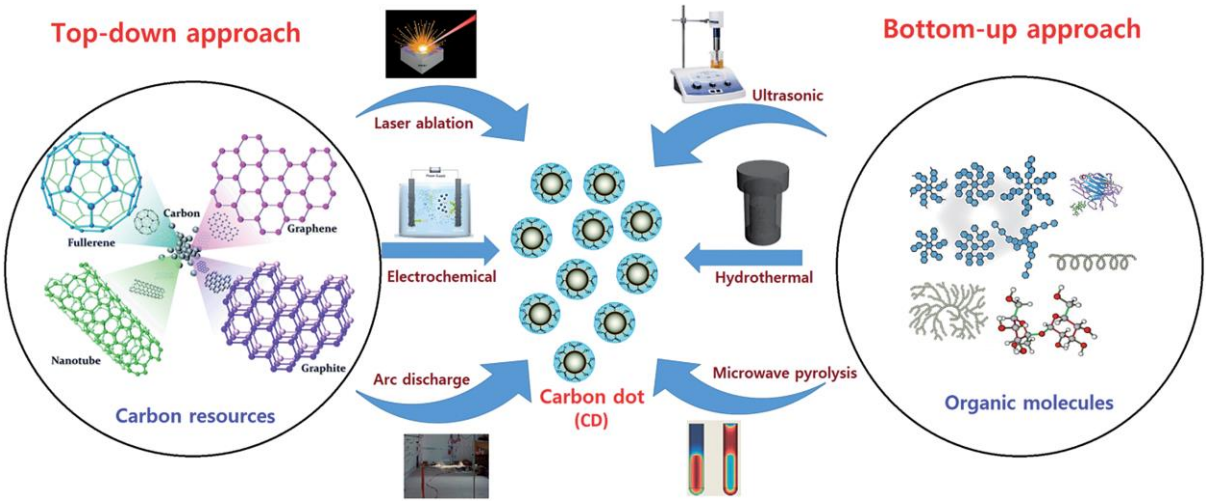


Figure 2.2: A simple schematic representation of the "top-down" and "bottom-up" synthesis approaches for the synthesis of Cdots (adopted from De and Karak, 2017)[19]

In the past, two very common synthesis steps in both "top-down" and "bottom-up" method (represented by **Figure 2.3** below) were important for the synthesis of Cdots with luminescent properties[3,5,7,11]. The first step was the surface functionalization step, where a carbon precursor was treated with a concentrated solution of sulfuric acid (H_2SO_4) and/or nitric acid (HNO_3)[5,24]. Following this a surface passivating step was used, where the resulting carbogenic material was further functionalized with polymers such as 4,7,10-trioxa-1,13-tridecanediamine (TTDDA), ethylenediamine, oleylamine, and bis (3-aminopropyl) terminated poly(ethylene glycol), abbreviated PEG_{1500N}[5,8,20,24]. The surface passivation step was very crucial for the production of the PL properties of Cdots[5,24].

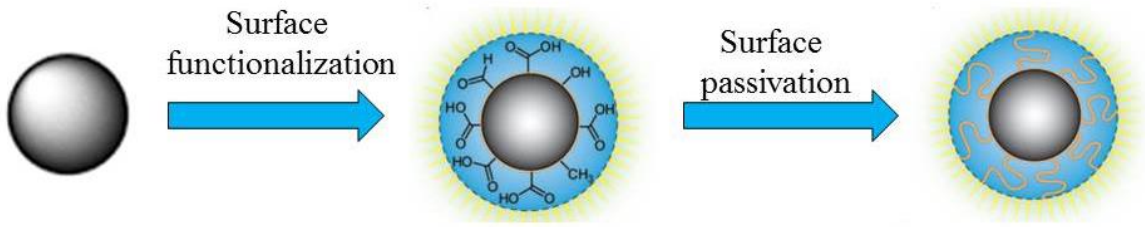


Figure 2.3: Cartoon illustrating surface change of Cdots after functionalization and passivation (after Baker and Baker, 2010)[5].

Using the "top-down", Su *et al.* produced Cdots from graphene and cement using a Q-switched neodymium-doped yttrium aluminium garnet (or Nd:YAG) laser method for ablation[8]. Thereafter, the obtained Cdots nanoparticles were functionalized by refluxing in concentrated HNO_3 solution. The as-prepared and acid treated Cdots did not show any fluorescent properties. However, the Cdots passivated with organic polymers such as PEG_{1500N} emitted strong PL. The particle sizes of the obtained Cdots were 5.0 nm[8]. Peng *et al.* also reported similar observation when synthesizing Cdots from carbohydrate (sucrose, glucose and starch). During synthesis, the carbohydrates were first dehydrated by a concentrated solution of H_2SO_4, and then functionalized by using concentrated HNO_3 solution. PL was also only observed after passivation of the surface with polymers such as 4,7,10-trioxa-1,13-tridecanediamine (TTDDA), ethylenediamine, oleylamine, and PEG_{1500N}[24].

Many of the past synthesis methods have drawbacks due to the requirement of sophisticated and expensive equipment, multiple synthesis steps and low product yield[11,20]. The continuous growth in interest on Cdots has opened the doors for the development of synthesis strategies that are much simpler, cost effective and environmentally friendly[20,25]. Therefore, the use of

harsh acids (H_2SO_4 and HNO_3) and equipment such as laser and arc discharge have become less popular. A significant amount of attention has been given to the "bottom-up" method for synthesis of both CQDs and GQDs[26]. For example, Lu *et al.* provided a simple one-step alternative method for synthesizing Cdots from black carbon, without using harsh acids or sophisticated equipment[25]. In their synthesis, black carbon was treated with hydrogen peroxide (a green solvent) for 90 min using a hydrothermal method, and then obtained Cdots with diameters between 3.0-4.5 nm[25]. Chen *et al.* produced Cdots from a one-step method using sucrose a carbon precursor and oleic acid as solvent[27]. Cdots with 1.8 nm size were produced after 5 min of heat treatment of the solution precursor in a hot oil bath[27]. Cdots obtained by both Lu *et al.* and Chen *et al.* had excellent PL properties and good photostability without any need for passivation[25,27]. N-doped Cdots have also been synthesized from a one-step hydrothermal reaction using chitosan as both a carbon and nitrogen source, and acetic acid as a solvent. The N-doped Cdots had an average particle size distribution of 5 nm[13].

2.1.1.1 Microwave-assisted syntheses

Microwave-assisted reactions are amongst the widely used methods for the synthesis of Cdots. Microwaves are electromagnetic waves with a 300 MHz to 300 GHz frequency range, corresponding to wavelengths between 1 mm and 1 m[28,29]. During microwave treatment, precursor molecules absorb electromagnetic fields generated by the microwave and converts them to heat energy to form the desired products[30,31]. Dielectric solvents, such as methanol, butanol, nitrobenzene, formic acid and even water absorb and convert electromagnetic irradiation into reaction heat[30,31]. Details on the mechanism and calculations related to electromagnetic irradiation absorption and conversion by different organic solvents have been discussed by Kappe[31]. Unlike traditional heating methods by the use of heating mantle, oil bath or hotplates, the use of microwave heating has the advantage of providing uniform heating, a short synthesis time and reproducible results[29–33]. Microwave heating also produces less by-products, and it allows for easy control of particle sizes, plus it is an environmentally friendly synthesis method[29–33].

For many years, microwave irradiation was mostly adopted for the synthesis of organic molecules such as functionalized aryl products, synthesized through a transition metal-catalysed reaction such as a coupling reaction[31,34]. However, there has been an increase in interest in microwave heating for the synthesis of inorganic metal nanoparticles such as zinc oxide (ZnO), copper oxide (CuO) and and silver (Ag) nanoparticles[35–38]. Different allotropes of carbon nanomaterials have also been synthesized using microwave-assisted reactions.

Carbon nanoparticles such as graphene, fullerene and CNT have been successfully synthesized in microwave-assisted reactions[39–41]. Microwave irradiation has also been used for post-functionalization of graphene, fullerene and CNT with organic and inorganic functional groups[39,42,43].

Functionalized Cdots with different particle sizes have also been obtained from microwave-assisted reactions. For example, using a microwave-assisted polyol method Liu *et al.* obtained a solution of Cdots with 5.0 nm particle sizes through a one-step conversion of sucrose, H_2SO_4 and polyethylene glycol (PEG)[32]. Bhaisare *et al.* also synthesized jelly-like N-doped Cdots by a 2-3 min microwave treatment of citric acid and tetraoctylammonium bromide (TOAB)[33]. The effect of TOAB (a capping agent) concentration on the morphology of N-doped Cdots was investigated. As the amount of TOAB was increased from 2 to 8 mL, the Cdots sizes became smaller (from > 10 nm to < 5 nm) and more dispersed[33]. N-doped Cdots have also been synthesized by a one-step, 15 min microwave treatment of chitosan, glacial acetic acid and ethylenediamine (EDA), to obtain N-doped Cdots with a size of 4.3 nm[44].

Although different solvents can been used for the synthesis of Cdots, as shown above, many publications have used water or no solvent at all in Cdots synthesis methods. These methods have been used for the synthesis of Cdots in the solid form[11]. Gong *et al.* have synthesized 3.0 nm Cdots nanoparticle by a 5 min microwave treatment of ascorbic acid and water[44]. N-doped Cdots (18 nm) were synthesized by Siriarti and Darmawan in 4 min using ascorbic acid as a carbon source, urea as a nitrogen source and water as a solvent[45]. Another interesting microwave synthesis procedure was reported by Li *et al.*[29]. In this report the synthesis of multi-functionalized (N-,P-doped) Cdots (3.3 nm) were achieved from N-phosphonomethyl aminodiacetic acid and ethylenediamine in water in 7 min[29]. PEG was also used in a one-step, one component microwave-assisted synthesis of Cdots synthesis under different atmosphere (air, oxygen and nitrogen) to give nanoparticles with sizes between 1-4 nm[26]. This shows that functionalized Cdots can be obtained from a variety of synthesis methods.

2.1.2 Optical properties

It is known that the PL emission wavelength of Cdots is excitation dependent[27,44,46]. However, Cdots typically emit light with wavelengths between 450-750 nm, corresponding to the entire visible to near infrared (NIR) region[46]. The PL peak of Cdots is usually broad. This

is due to the different functional group moieties associated with their structure[47]. The Cdots also absorb ultra-violet to visible (UV-vis) radiation[46,48]. Typically, absorption peaks are observed between 260-320 nm and 350-550 nm, corresponding to a $\pi \rightarrow \pi^*$ transition associated with the C=C (aromatic sp^2) bonds and $n \rightarrow \pi^*$ transition associated with the surface functional groups, especially the oxygen functional groups[46,48].

2.1.3 Applications

The fascinating aspect of Cdots is associated with their size and excitation wavelength dependant PL properties and their biocompatibility [3,5,14,18]. Another advantage is that these materials are derived from carbon, which is a highly abundant and non-toxic element[3,7]. Their surface oxygen and/or nitrogen functional groups makes it easy to manipulate the surface chemistry of Cdots by further functionalizing them with organic or inorganic functional groups (as discussed above)[14]. Manipulating the surface chemistry of Cdots makes it easy to tune their solubility and PL properties[14]. The electronic properties and photostability of Cdots are very similar to those of metal-based quantum dots (QDs)[3,7,14]. However, unlike QDs, Cdots have very low toxicity, and they can be easily synthesized from inexpensive materials and energy saving procedures in large quantities[3,7]. Therefore, due to their excellent PL properties and low toxicity, Cdots have been used as alternatives for QDs especially in biotechnology and solar cells[3,27,49].

Over the past decade, there has been an exponential increase in the number of publication on Cdots[14]. Interestingly, according to a Web of Science™ search done by Wang *et al.*, Chinese authors have contributed 47 % of all publications on Cdots, making them the highest contributors since the discovery of Cdots[14]. As mentioned above, the majority of these publications are based on exploiting the PL properties of Cdots for application in bioimaging, chemical and biological sensing, drug delivery, photocatalysis, solar cells, semiconductors *etc*[1,5,7,14]. Details on how Cdots are applied in the above mentioned technologies have been extensively discussed in the literature.

A few publications have described making use of Cdots size and reduction properties. Genc *et al.* used Cdots for the fabrication of Cdots/MnO_2 hydrid nanorod electrodes for supercapacitors. Amongst other observations, the conductivity and ion-donating properties of Cdots were found to improve the electron transfer properties of the electrode[50]. Cdots have also been used as reducing and stabilizing agents for the synthesis of metal nanoparticles and their subsequent use. For example, Unnikrishnan *et al.* used Cdots to disperse graphene

sheets and to also reduce potassium permanganate ($KMnO_4$) to MnO_2 under mild conditions (75 °C), while the sp^2 type carbon on graphene remained protected[51]. The graphene-Cdots-MnO_2 nanocomposite was also used in electrode fabrication in supercapacitors[51]. Using X-ray photoelectron spectroscopy (XPS) and Fourier transform infrared (FT-IR) results, the authors concluded that the reduction of MnO_2 is accompanied by oxidation of the C=C and oxygen-type functional groups of Cdots[51]. Liu *at el.* also reported a similar observation from the formation of a Silver(Ag)-N-doped Cdots nanocomposite[52]. Cdots have also been used as reducing and stabilizing agent of palladium (Pd) nanoparticle for use in the Heck and Suzuki-Miyaura coupling reactions[53].

In this study microwave-assisted syntheses were employed for making functionalized Cdots. Cdots were synthesized from ascorbic acid[44], sucrose[27,32], chitosan[54] and ascorbic acid and urea[45], with slight modifications from the methods represented in the literature. Since all these reactions can be classified as "bottom-up" methods, the obtained Cdots are expected to be the CQDs and not GQDs, as described earlier in this chapter. The abbreviation "Cdots" (instead of CQDs) has therefore been used throughout this dissertation to describe the all Cdots synthesized from the "bottom-up" microwave-assisted methods.

2.2 Introduction: Fischer-Tropsch Process

The conversion of coal-to-liquid (CTL), gas-to-liquid (GTL) and biomass-to-liquid (BTL) by means of the Fischer-Tropsch (F-T) process is a powerful and most promising approach for fuel production around the world[55,56]. In the most general sense, the F-T process is the conversion of syngas, such as hydrogen (H_2) and carbon monoxide (CO) or carbon dioxide (CO_2), to hydrocarbons and oxygen-based chemicals as by-products[55–58]. In 1902, Sabatier and Senderens used cobalt (Co) or nickel (Ni) to catalyse the hydrogenation of CO or CO_2 to methane 180- 200 °C under atmospheric pressure[59,60]. Later in 1923, scientists Franz Fischer and Hans Tropsch (whom the process was named after) showed that both Co and iron (Fe) are capable of converting syngas from coal to long chain hydrocarbon under low pressures (< 10 bar)[59,60].

Fischer and Tropsch laid the ground breaking work which enabled companies such as Ruhrchemie (Germany) in 1927 to develop an industrial scale F-T plant which later produced millions of barrels of fuel for Germany[57,59]. Years later, what started as laboratory experiments has become the industry's biggest producer of synthesized fuel, and the process became even more important because of the scarcity of crude oil reserves and environmental pollution[61]. South Africa, being a country with large coal reserves, adopted the F-T process for CTL conversion in 1955 under Sasol[62–64]. The abundance of natural gas reserves in many parts of the world inspired the development of new plants based on the GTL F-T process[3]. Shell Bintulu in Malaysia built a GTL F-T plant in 1993, in 2006 Sasol and Qatar Petroleum built a GTL F-T plant in Qatar, and in 2015 Sasol SasolChevron also built its Escarvos GTL plant in Nigeria[57,59,63,65].

2.2.1 The F-T process chemistry

In the F-T process, CO (or CO_2) is hydrogenated via a heterogeneous catalyzed surface polymerization reaction[56,66,67]. The reduction process for CO and CO_2 are represented by **eq. 2.1** and **2.2** below. Although both CO and CO_2 are converted to hydrocarbons, CO_2 hydrogenation is a two-step reaction which requires three moles of hydrogen; therefore the process is much slower compared to CO hydrogenation[61,68]. CO_2 hydrogenation also produces plenty of water as by-product which accelerate the deactivation of the catalysts[68].

The actual mechanism of the conversion of syngas to long chain hydrocarbons using the F-T process is not well understood. There are different mechanisms proposed so far which have been discussed elsewhere[69–71]. However, the general understanding is that CO is

hydrogenated to form -CH_2- monomer (**eq. 2.2**), which undergo step by step polymerization to form long chain hydrocarbons that include alkanes, alkenes and oxygen-based chemicals, represented by simplified reactions equations **eq. 2.3-2.5** below[65,66,72]. The F-T products are separated into methane and unreacted syngas which can be recycled, the gas fraction (C_2-C_4), petrol (C_5-C_{11}), diesel (C_{12}-C_{18}), wax (C_{19+}) and other chemicals (e.g alcohols)[72]. The production of long chain (C_{5+}) hydrocarbons and low selectivity to methane (C_1) is usually desired in the F-T process[73]. However, the major products depend on the catalyst used, type of support, reaction temperature, syngas ratios *etc*.

Two-step CO_2 reduction series:

$$CO_2 + H_2 \leftrightarrow CO + H_2O$$ ….....**eq. 2.1**

$$CO + 2H_2 \rightarrow -(CH_2) - + H_2O$$ ……...**eq. 2.2**

Simplified F-T chemical reactions:

Alkanes: $$nCO + (2n + 1)H_2 \rightarrow C_n H_{2n+2} + nH_2O$$ .....**eq. 2.3**

Alkenes: $$nCO + 2nH_2 \rightarrow C_n H_{2n} + nH_2O$$ .....**eq. 2.4**

Alcohol: $$nCO + 2nH_2 \rightarrow C_n H_{2n+1}OH + (n-1)H_2O$$ .....**eq. 2.5**

n = integer

Water-Gas-Shift (WGS) reaction: $$CO + H_2O \leftrightharpoons CO_2 + H_2$$……**eq. 2.6**

As seen in the equations above, water is a by-product of F-T reactions derived from the hydrogenation of the oxygen atom in CO[74]. Although water is a non-toxic solvent in general, the presence of water in the F-T medium can accelerate the deactivation of a catalyst, especially Co[74,75]. Deactivation may result from oxidation Co to F-T inactive CoO, hydrothermal sintering of cobalt particles, and the formation of Co-support complexes[75] . Iron is not as easily deactivated by water like Co. In Fe-based F-T reaction, water participates in the water to gas shift (WGS) reaction catalysed by Fe (in **eq. 2.6**)[76]. WGS is an important reaction in synthesis processes when low amounts of H_2 are available for hydrogenation of CO, and hence Fe is used for CTL and BTL F-T processes[76,77].

2.2.2 F-T catalysts

Metals from group 8-10 of the periodic table especially Co, Fe, Ni and Ru can be used to catalyze the F-T process[72,77,78]. However, Co and Fe are the most commonly used catalysts both academically and industrially[78,79]. The products produced from the F-T process can be affected by the choice of the catalyst. It has been reported that the catalysts activity and long chain hydrocarbons selectivity produced by F-T synthesis decreased as follows: Ru > Co > Fe > Ni [72].

Ni is an active F-T catalyst which produces predominantly methane (n=1, in **eq. 2.1**) at high temperatures (300-350 °C), which is not a desired F-T product[57,72]. At lower temperatures (190-260 °C), Ni forms volatile nickel carbonyl complexes, thereby resulting in the loss of the catalyst[57]. Ru is a highly active F-T catalyst, with high selectivity to long chain hydrocarbons at low temperatures and has good stability in the presence of large amounts of water[77,78,80]. However, Ru has an estimated earth abundance of 0.0004 parts per million and hence is very expensive[81]. This excludes Ru for commercial application. Because of these considerations, Ni and Ru are used for the synthesis of bimetallic F-T catalysts[76,82]. Ru is also used as a catalyst promoter for Fe- or Co-based F-T processes[76,83,84].

Fe is a cheap F-T catalyst with very low selectivity toward methane[66,85]. The catalyst is highly active especially at high temperatures (300-350 °C) and low H_2/CO ratios (~ 1) as mentioned above[76,77]. Fe is however less active compared to Ru and Co[80]. Fe_3O_4 shows selectivity towards the WGS reaction, which is a side reaction in the F-T process[76,77]. The formation of Fe oxides under the F-T condition reduces the number of F-T active catalytic species[62].

2.2.3 Co-based F-T reactions

Co is the most active and selective F-T catalyst at low temperatures (after Ru)[64]. It is also more abundant and cheaper than Ru. Compared to Fe, Co has low selectivity towards the WGS reaction, and this makes it the preferred catalyst for F-T synthesis, especially when natural gas is used as a carbon source[86,87]. The Co as F-T catalyst has been widely used in both academia and industry for the synthesis of long chain hydrocarbons, under a variety of conditions[80]. Co is mostly active at low temperature (200-240 °C) F-T conditions[65]. Co-based F-T process is preferred for GTL conversion due to high CO conversion, high activity and selectively towards long chain hydrocarbons[88]. Syngas derived from natural gas has a ratio of 2 ratios of H_2/CO[88].

A Co catalyst is often derived from its precursor Co_3O_4, and the oxide undergo a two-step reduction process from Co_3O_4 to CoO and finally to metallic Co (or Co^0) metal. Metallic Co is the F-T active catalytic species[85,86]. Co can exist in the hexagonal close packed (hcp) and/or the face centred cubic (fcc) crystallographic structure, and both have significantly different activities as F-T catalysts[89]. The Co (hcp) form is the more highly active form of Co as it has the appropriate active sites desired for F-T conversion[89–91].

The type of crystallographic structure formed after Co_3O_4 reduction depends on a number factors, including crystallite size and catalyst support[89–91]. Kitakami *et al.* reported that Co (hcp) is dominant when metallic Co crystallite sizes are > 40 nm, particle between 20-40 nm have both the Co (hcp) and Co (fcc) phase, and the Co (fcc) phase is mostly dominant in Co with crystallite sizes < 20 nm[92]. Different supports can also promote the formation of Co (hcp) and/or Co (fcc). For example, SiO_2 supports are said to promote the formation of Co (fcc) while the Co (hcp) forms when cobalt oxide is supported on Al_2O_3[91,93].

The importance of supporting Co nanoparticles was highlighted in **CHAPTER 1**. Inorganic oxides (SiO_2, Al_3O_4 and TiO_2) and shaped carbon materials (graphene, CNTs, CSs *etc.*) are used as catalysts supports[83,94]. The type of support used not only affects the phase of Co metal formed but it also affects the reduction temperature of reduction of Co_3O_4 to CoO and Co[93–95]. The reducibility of Co_3O_4 nanoparticles affects the activity and selectivity of the metal catalyst. This is because the more Co_3O_4 nanoparticles are reduced to Co, the higher the number of F-T active catalytic species, and hence the better the catalyst activity and selectivity[75,96]. Therefore, the support material does not only stabilize the catalyst, but it can also act as an activity and selectivity promoter[86]. The reducibility of Co_3O_4 to F-T active Co depends on metal to support interactions (MSIs)[55,86].

2.2.4 MSIs and inverse-supported catalysts

MSIs are the physical and chemical interactions between the metal catalyst and the support[83,97,98]. The stronger they are, the better the stability of a catalyst on a support during the F-T reaction process[83,86]. Cobalt catalysts supported on inorganic oxides have strong metal to support interactions which helps keep the catalyst stable during the F-T process and more resistanct to sintering compared to a carbon support[83,86]. However, Co_3O_4 reduction to its F-T active Co species requires higher temperatures compared to the reduction of Co_3O_4 to Co on a carbon support[79,83,86]. The Co nanoparticles supported on carbon nanomaterials are however most likely to sinter[79,83,86]. To improve the stability of a carbon support, the carbon

material is usually doped with heteroatoms such as nitrogen, oxygen and boron[72,83]. For example, carbon spheres (with sizes between 200-400 nm) doped with nitrogen produce a supported catalyst with better catalyst stability than a catalyst supported on undoped carbon spheres[72]. This means that the interactions between the metal and the support change when the surface chemistry of the support is changed[86,99,100].

As mentioned in **CHAPTER 1**, there are different approaches used to investigate these interactions and they are all related to supported catalyst fabrication[98]. These are the conventional method, core-shell method, and the inverse method[86,100]. In the conventional approach, small catalyst particle sizes are dispersed on a bulk support, the core-shell method involves encapsulating the catalyst inside a support, and the inverse approach is the opposite of the conventional method[86,100].

MSIs have been widely studied using the conventional method and the core-shell method using both inorganic oxide and carbon supported Co-based F-T catalyst[83,86,90,99,101]. MSIs between cobalt and inorganic oxides have been studied using the inverse supported catalyst model[86,87,99,100]. One of the studies was based on metal to support interactions between Co_3O_4 and a silica support [86]. In the study, Co_3O_4 with particle sizes between 17 and 50 nm were synthesised. The particles were then "decorated" with tetraethyl orthosilicate (TEOS) using the inverse approach to investigate the Co-O-Si metal to support interactions. Different amounts of tetraethyl orthosilicate were added to the catalysts. The results obtained were compared to the catalytic activity of Co in an unsupported Co_3O_4 catalyst. The supported catalyst showed a thirteen times increase in the rate of reaction and catalytic activity compared to the unsupported catalyst. The catalysts also showed very good selectivity towards long chain aliphatic hydrocarbon and showed a decrease in both methane and olefin selectivity. The rate and activity of the catalyst increased with increase in the amount of support material (TEOS) added to the catalyst.

The strong MSIs allowed the catalytic species to remain very stable throughout the F-T process, with only a small amount of increase in particle size being observed after the reaction. The reduction temperature was determined using TPR studies to investigate the effect of MSIs. The Co_3O_4 nanoparticles were however reduced at high temperatures (> 400 °C) compared to unsupported Co_3O_4 (< 350 °C), due to the strong MSIs. The reduction temperature increased with an increase in the concentration of TEOS. The presence of hard to reduce Co-silicates were noted[86]. These results show that the inverse method not only affords

a good understanding of MSIs, but it also showed how these MSIs can be manipulated to improve the catalyst activity and selectivity.

As mentioned in **CHAPTER 1**, Cdots were used as dispersing and stabilizing agent for Co-based Fischer-Trospch catalysts. The ability of Cdots and N-doped Cdots to disperse and stabilize Co nanoparticles will be studied and compared. The reducing properties of Cdots were also investigated in this study. This was done by looking at the reducibility of Co_3O_4 nanoparticle to Co (active Fischer-Tropsch catalytic species) using *in-situ* X-ray diffraction (XRD) technique and comparing the results with Co_3O_4 nanoparticle reducibility using hydrogen as a reducing agent. Co can exist in two different phases namely the fcc and hcp phases, the latter being the most active form in Co-based Fischer-Tropsch reactions[89]. The types of phase/s that are formed during the two reduction conditions were also investigated.

References

1. Xu, Y., Wu, M., Liu, Y., Feng, X. Z., Yin, X. B., He, X. W. & Zhang, Y. K. Nitrogen-Doped Carbon Dots: A Facile and General Preparation Method, Photoluminescence Investigation, and Imaging Applications. *Chem. a Eur. J.* **19**, 2276–2283 (2013).

2. Liu, H., Zhang, L., Yan, M. & Yu, J. Carbon nanostructures in biology and medicine. *J. Mater. Chem. B* **5**, 6437–6450 (2017).

3. Jelinek, R. *Carbon Quantum Dots*.1–129 (Springer International Publishing Switzerland, 2017).

4. Wang, Y., Zhu, Y., Yu, S. & Jiang, C. Fluorescent carbon dots: rational synthesis, tunable optical properties and analytical applications. *RSC Adv.* **7**, 40973–40989 (2017).

5. Baker, S. N. & Baker, G. A. Luminescent Carbon Nanodots : Emergent Nanolights. *Angew. Chem. Int. Ed*. **49**, 6726–6744 (2010).

6. Xu, X., Ray, R., Gu, Y., Ploehn, H. J., Gearheart, L., Raker, K. & Scrivens W. A. Electrophoretic Analysis and Purification of Fluorescent Single-Walled Carbon Nanotube Fragments. *J. Am. Chem. Soc*. **126**, 12736–12737 (2004).

7. Wang, Y. & Hu, A. Carbon quantum dots: synthesis, properties and applications. *J. Mater. Chem. C* **2**, 6921–6939 (2014).

8. Sun, Y. P., Zhou, B., Lin, Y., Wang, W., Fernando, K. A. S., Pathak, P., Meziani, M. J., Harruff, B. A., Wang, X., Wang, H., Luo, P. G., Yang, H., Kose, M. E., Chen, B., Veca, L. M., Xie, S. Y. Quantum-Sized Carbon Dots for Bright and Colorful Photoluminescence. *J. Am. Chem. Soc.* **128**,7756–7757 (2006).

9. Wang, R., Lu, K. Q., Tang, Z. R. & Xu, Y. J. Recent progress in carbon quantum dots: synthesis, properties and applications in photocatalysis. *J. Mater. Chem. A* **5**, 3717–3734 (2017).

10. Tuerhong, M., Xu, Y. & Yin, X. B. Review on Carbon Dots and Their Applications. *Chin. J. Anal. Chem.* **45**, 139–150 (2017).

11. Zhang, J. & Yu, S. H. Carbon dots: large-scale synthesis, sensing and bioimaging. *Mater. Today* **19**, 382–393 (2016).

12. Lim, S. Y., Shen, W. & Gao, Z. Carbon quantum dots and their applications. *Chem. Soc. Rev.* **44**, 362–381 (2014).

13. Yang, Y., Cui, J., Zheng, M., Hu, C., Tan, S., Xiao, Y., Yang, Q. & Liu, Y. One-step synthesis of amino-functionalized fluorescent carbon nanoparticles by hydrothermal carbonization of chitosan. *Chem. Comm.* **48**, 380–382 (2012).

14. Wang, J., Choi, H. S. & Wáng, Y. X. J. Exponential growth of publications on carbon nanodots by Chinese authors. *J. Thorac. Dis.* **7**, 201–205 (2015).

15. Dong, Y. Lin, J., Chen, Y., Fu, F., Chi, Y. & Chen, G. Graphene quantum dots, graphene oxide, carbon quantum dots and graphite nanocrystals in coals. *Nanoscale* **6**, 7410–7415 (2014).

16. Lim, C. S., Hola, K., Ambrosi, A., Zboril, R. & Pumera, M. Graphene and carbon quantum dots electrochemistry. *Electrochem. commun.* **52**, 75–79 (2015).

17. Li, H., Kang, Z., Liu, Y. & Lee, S. T. Carbon nanodots: synthesis, properties and applications. *J. Mater. Chem.* **22**, 24230–24253 (2012).

18. Li, X., Wang, H., Shimizu, Y., Pyatenko, A., Kawaguchi, K. & Koshizaki, N. Preparation of carbon quantum dots with tunable photoluminescence by rapid laser passivation in ordinary organic solvents. *Chem. Commun.* **47**, 932–934 (2011).

19. De, B. & Karak, N. Recent progress in carbon dot–metal based nanohybrids for photochemical and electrochemical applications. *J. Mater. Chem. A* **5**, 1826–1859 (2017).

20. Peng, J., Gao, W., Gupta, B. K., Liu, Z., Romero-Aburto, R., Ge, L., Song, L., Alemany, L. B., Zhan, X., Gao, G., Vithayathil, S. A., Kaipparettu, B. A., Marti, A. A., Hayashi, T., Zhu, J. J. & Ajayan, P. M. Graphene quantum dots derived from carbon fibers. *Nano Lett.* **12**, 844–849 (2012).

21. Qiao, Z. A., Wang,Y., Gao, Y., Li, H., Dai, T., Liu, Y. & Huo, Q. Commercially activated carbon as the source for producing multicolor photoluminescent carbon dots by chemical oxidation. *Chem. Commun.* **46**, 8812–8814 (2010).

22. Zhou, J., Sheng, Z., Han, H., Zou, M. & Li, C. Facile synthesis of fluorescent carbon dots using watermelon peel as a carbon source. *Mater. Lett.* **66**, 222–224 (2012).

23. Prasannan, A. & Imae, T. One-pot synthesis of fluorescent carbon dots from orange waste peels. *Ind. Eng. Chem. Res.* **52**, 15673–15678 (2013).

24. Peng, H. & Travas-Sejdic, J. Simple aqueous solution route to luminescent carbogenic dots from carbohydrates. *Chem. Mater.* **21**, 5563–5565 (2009).

25. Lu, Q., Wu, C., Liu , D., Wang, H., Su, W., Li, H., Zhang, Y. & Yao, S. A facile and simple method for synthesis of graphene oxide quantum dots from black carbon. *Green Chem.* **19**, 900–904 (2017).

26. Zhao, Y., Zuo, S. & Miao, M. The effect of oxygen on the microwave-assisted polyethylene glycol. *RSC Adv.* **7**, 16637–16643 (2017).

27. Chen, B., Li, F., Li , S., Weng , W., Guo , H., Guo , T., Zhang , X., Chen , Y., Huang , T., Hong , X., You , S., Lin , Y., Zeng, K. & Chen, S. Large scale synthesis of photoluminescent carbon nanodots and their application for bioimaging. *Nanoscale* **5**, 1967–1971 (2013).

28. Wang, Q., Liu, X., Zhang, L. & Lv, Y. Microwave-assisted synthesis of carbon nanodots through an eggshell membrane and their fluorescent application. *Analyst* **137**, 5392–5397 (2012).

29. Li, H., Shao, F. Q., Zou, S. Y., Yang, Q. J., Huang, H., Feng, J. J. & Wang, A. J. Microwave-assisted synthesis of N , P-doped carbon dots for fluorescent cell imaging. *Microchimica Acta.* **183**, 821–826 (2016).

30. Hong, E. H., Lee, K. H., Oh, S. H. & Park, C. G. Synthesis of Carbon Nanotubes Using Microwave Radiation. *Adv. Funct. Mater.* **13**, 961–966 (2003).

31. Kappe, C. O. & Dallinger, D. Controlled microwave heating in modern organic synthesis: Highlights from the 2004-2008 literature. *Mol. Divers.* **13**, 71–193 (2009).

32. Liu, Y. Xiao, N., Gong, N., Wang, H., Shi, X., Gua, W. & Yea, L. One-step microwave-assisted polyol synthesis of green luminescent carbon dots as optical nanoprobes. *Carbon* **68**, 258–264 (2013).

33. Bhaisare, M. L., Talib, A., Khan, M. S. & Pandey, S. Synthesis of fluorescent carbon dots via microwave carbonization of citric acid in presence of tetraoctylammonium ion, and their application to cellular bioimaging. *Microchimica Acta.* **182**, 2173–2181 (2015).

34. Lidström, P., Tierney, J., Wathey, B. & Westman, J. Microwave assisted organic synthesis—a review. *Tetrahedron* **57**, 9225–9283 (2001).

35. Hasanpoor, M., Aliofkhazraei, M. & Delavari, H. Microwave-assisted Synthesis of Zinc Oxide Nanoparticles. *Procedia Mater. Sci.* **11**, 320–325 (2015).

36. Zhang, C. Y., Zhu, H. T., Wang, J. X. & Chang, S. B. Preparation of CuO nanoparticles by ultrasonic vibration and microwave irradiation. *Rare Met. Mater. Eng.* **36**, 88–90 (2007).

37. Zhao, X., Xia, Y., Li, Q., Ma, X., Quan, F., Geng, C. & Han, Z. Microwave-assisted synthesis of silver nanoparticles using sodium alginate and their antibacterial activity. *Colloids Surfaces A Physicochem. Eng. Asp.* **444**, 180–188 (2014).

38. Bilecka, I. & Niederberger, M. Microwave chemistry for inorganic nanomaterials synthesis. *Nanoscale* **2**, 1358–1374 (2010).

39. Economopoulos, S. P., Rotas, G., Miyata, Y., Shinohara, H. & Tagmatarchis, N. Exfoliation and Chemical Modification. *ACS Nan.* **4**, 7499–7507 (2010).

40. Hetzel, R., Manning, T., Lovingood, D., Strouse, G. & Phillips, D. Production of fullerenes by microwave synthesis. *Fuller. Nanotub. Carbon Nanostruct.* **20**, 99–108 (2012).

41. Schwenke, A. M., Hoeppener, S. & Schubert, U. S. Synthesis and Modification of Carbon Nanomaterials utilizing Microwave Heating. *Adv. Mater.* **27**, 4113–4141 (2015).

42. Economopoulos, P., Karousis, N., Rotas, G., Pagona, G. & Tagmatarchis, N. Microwave-assisted Functionalization of Carbon Nanostructured Materials. *Curr. Org. Chem.* **15**, 1121–1132 (2011).

43. Vázquez, E. & Prato, M. Carbon Nanotubes and Microwaves : *ACS Nano* **3**, 3819–3824 (2009).

44. Gong, J., Lu, X. & An, X. Carbon dots as fluorescent off–on nanosensors for ascorbic acid detection. *RSC Adv.* **5**, 8533–8536 (2015).

45. Sugiarti, S. & Darmawan, N. Synthesis of fluorescence carbon nanoparticles from ascorbic acid. *Indones. J. Chem.* **15**, 141–145 (2015).

46. Roy, P., Chen, P. C, Periasamy, A. P., Chen, Y. N. & Chang, H. T. Photoluminescent carbon nanodots : synthesis , physicochemical properties and analytical applications. *Mater. Today.* **18**, 447–458 (2015).

47. Zhu, S., Song, S., Zhao, X., Shao, J., Zhang, J. & Yang, B. The photoluminescence mechanism in carbon dots (graphene quantum dots , carbon nanodots and polymer dots): current state and future perspective. *Nano. Res.* **8**, 355–381(2014).

48. Peng, Z., Han. X., Li, S., Al-Youbi, A. O., Bashammakh, A. S., El-Shahawi, M. S. & Leblanc, R. M. Carbon dots : Biomacromolecule interaction , bioimaging and nanomedicine. *Coord. Chem. Rev.* **343**, 256–277 (2017).

49. Wang, H., Sun, P., Cong, S., Wu, J., Gao, L., Wang, Y., Dai, X., Yi, Q. & Zou, G. Nitrogen-Doped Carbon Dots for ‘ green ’ Quantum Dot Solar Cells. *Nanoscale Res. Lett.* **11**, 1–6 (2016).

50. Genc, R., Alas, M. O., Harputlu, E., Repp, S., Kremer, N., Castellano, M., Colak, S. G., Ocakoglu, K. & Erdem, E. High-Capacitance Hybrid Supercapacitor Based on Multi-Colored Fluorescent Carbon-Dots. *Sci. Rep.* **7**, 1–13 (2017).

51. Unnikrishnan, B., Wu, W. C., Chen, I. W. P., Chang, H. T., Lin, C. H. & Huang, C. C. Carbon Dot-Mediated Synthesis of Manganese Oxide Decorated Graphene Nanosheets for Supercapacitor Application. *ACS Sustain. Chem. Eng.* **4**, 3008–3016 (2016).

52. Liu, T., Dong, J. X., Liu, S. G., Liu, S. G., Li, N., Lin, S. M., Fan, Y. Z., Lei, J. L., Luo, H. Q. & Li, N. B. Carbon quantum dots prepared with polyethyleneimine as both reducing agent and stabilizer for synthesis of Ag/CQDs composite for Hg^{2+} ions detection. *J. Hazard. Mater.* **322**, 430–436 (2017).

53. Dey, D., Bhattacharya, T., Majumdar, B., Mandani, S., Sharm, B. & Sarma, T. K. Carbon dot reduced palladium nanoparticles as active catalysts for carbon–carbon bond formation. *Dalt. Trans.* **42**, 13821-13825 (2013).

54. Xiao, D., Yuan, D., He, H. & Lu, J. Microwave-assisted one-step green synthesis of amino-functionalized fluorescent carbon nitride dots from chitosan. *Luminescence* **28**, 612–615 (2013).

55. van Vliet, O. P. R., Faaij, A. P. C. & Turkenburg, W. C. Fischer – Tropsch diesel production in a well-to-wheel perspective : A carbon , energy flow and cost analysis. *Energy Convers. Manag.* **50**, 855–876 (2009).

56. Ail, S. S. & Dasappa, S. Biomass to liquid transportation fuel via Fischer Tropsch synthesis – Technology review and current scenario. *Renewable Sustainable Energy Rev.* **58**, 267–286 (2016).

57. Dry, M. E. High quality diesel via the Fischer – Tropsch process – a review. *Technol. Biotechnol*. **77**, 43–50 (2002).

58. Sauciuc, A., Potetz, A., Weber, G., Rauch, R., Hofbauer, H. & Dumitrescu, L. Synthetic diesel from biomass by Fischer-Tropsch synthesis. In: International conference of renewable energies and power quality (ICREPQ '11). Spain: Las Palmas de Gran Canaria, 2–7 (2011).

59. Khodakov, A. Y., Chu, W. & Fongarland, P. Advances in the Development of Novel Cobalt Fischer − Tropsch Catalysts for Synthesis of Long-Chain Hydrocarbons and Clean Fuels. *Chem. Rev.* **107**, 1692–1744 (2007).

60. Fischer, F. The Fischer-Tropsch Synthesis: Molecular Weight Distribution of Primary Products and Reaction Mechanism. **15**, 136–141 (1975).

61. Melaet, G., Ralston, W. T., Li, C. S., Alayoglu, S., An, K., Musselwhite, N., Kalkan, B. & Somorjai, G. A. Evidence of highly active cobalt oxide catalyst for the Fischer-Tropsch synthesis and CO_2 hydrogenation. *J. Am. Chem. Soc.* **136**, 2260–2263 (2014).

62. Dry, M. E. Fischer-Tropsch synthesis over iron catalysts. *Catal. Letters* **7**, 241–251 (1990).

63. Krishna, R. & Sie, S. T. Design and scale-up of the Fischer – Tropsch bubble column slurry reactor. *Fuel Processing Technology* **64**, 73–105 (2000).

64. Krylova, A. Y. Products of the Fischer – Tropsch Synthesis (A Review). *Solid Fuel Chemistry* **48**, 23–36 (2014).

65. Dry, M. E. The Fischer – Tropsch process : 1950 – 2000. *Catalysis Today* **71,** 227–241 (2002).

66. Phaahlamohlaka, T. N. Synthesis of carbon nanofibers and their subsequent use as catalyst supports for Fischer- Tropsch synthesis By. MSc Dissertation (University of the Witwatersrand, Johannesburg 2013).

67. Faaij, P. C., Hamelinck, C. N. & van Hardeveld, M. R. M. Exploration of the possibilities for production of Fischer Tropsch liquids and power via biomass gasiÿcation. *Biomass and Bioenergy* **23**, 129–152 (2002).

68. Choi, Y. H., Jang, Y. J., Park, H., Kim, W. Y., Lee, Y. H., Choi, S. H. & Lee, J. S. Carbon dioxide Fischer-Tropsch synthesis: A new path to carbon-neutral fuels. *Appl. Catal. B Environ.* **202**, 605–610 (2017).

69. Schulz, H., Erich, E., Gorre, H. & van Steen, E. Regularities of selectivity as a key for discriminating FT-surface reactions and formation of the dynamic system. *Catal. Letters* **7**, 157–167 (1990).

70. Long, H. C., Turner, M. L., Fornasiero, P., Kašpar, J., Graziani, M. & Maitlis, P. M. Vinylic initiation of the Fischer-Tropsch reaction over ruthenium on silica catalysts. *J. Catal.* **167**, 172–179 (1997).

71. Davis, B. H. Fischer-Tropsch synthesis: Current mechanism and futuristic needs. *Fuel Process. Technol.* **71**, 157–166 (2001).

72. Moyo, M. Cobalt and Iron Supported on Carbon Spheres Catalysts for Fischer. PhD Thesis (University of the Witwatersrand, Johannesburg, 2012).

73. Bukur, D. B., Todic, B. & Elbashir, N. Role of water-gas-shift reaction in Fischer-Tropsch synthesis on iron. *Catal. Today* **275**, 66–75 (2016).

74. Hibbitts, D. D., Loveless, B. T., Neurock, M. & Iglesia, E. Mechanistic role of water on the rate and selectivity of Fischer-Tropsch synthesis on ruthenium catalysts. *Angew. Chemie - Int. Ed.* **52**, 12273–12278 (2013).

75. Wolf, M., Kotzé, H., Fischer, N. & Claeys, M. Size dependent stability of cobalt nanoparticles on silica under high conversion Fischer–Tropsch environment. *Faraday Discuss.* **197**, 243–268 (2017).

76. Li, T., Wang, H., Yang, Y., Xiang, H. & Li, Y. Study on an iron-nickel bimetallic Fischer-Tropsch synthesis catalyst. *Fuel Process. Technol.* **118**, 1–8 (2014).

77. Jahangiri, H., Bennett, J., Mahjoubi, P., Wilson, K. & Gu, S. A review of advanced catalyst development for Fischer–Tropsch synthesis of hydrocarbons from biomass derived syn-gas. *Catal. Sci. Technol.* **4**, 2210–2229 (2014).

78. Khodakov, A. Y., Chu, W. & Fongarland, P. Advances in the development of novel cobalt Fischer-Tropsch catalysts for synthesis of long-chain hydrocarbons and clean fuels. *Chem. Rev.* **107**, 1692–1744 (2007).

79. Motchelaho, M. A. M., Xiong, H., Moyo, M., Jewell, L. L. & Coville, N. J. Effect of acid treatment on the surface of multiwalled carbon nanotubes prepared from Fe-Co supported on $CaCO_3$: Correlation with Fischer-Tropsch catalyst activity. *J. Mol. Catal. A Chem.* **335**, 189–198 (2011).

80. Ordomsky, V. V., Khodakov, A. Y., Legras, B. & Lancelot, C. Fischer–Tropsch synthesis on a ruthenium catalyst in two-phase systems: an excellent opportunity for the control of reaction rate and selectivity. *Catal. Sci. Technol.* **4**, 2896 (2014).

81. Schulz, H. Short history and present trends of Fischer – Tropsch synthesis. *Applied Catalysis A: General* **186,** 3–12 (1999).

82. Phaahlamohlaka, T. N., Kumi, D. O., Dlamini, M. W., Forbes, R., Jewell, L. L., Billing, D. G. & Coville, N. J. Effects of Co and Ru Intimacy in Fischer − Tropsch Catalysts Using Hollow Carbon Sphere Supports : Assessment of the Hydrogen Spillover Processes. *ACS Catal.* **7**, 1568−1578 (2017).

83. Xiong, H., Jewell, L. L. & Coville, N. J. Shaped Carbons As Supports for the Catalytic Conversion of Syngas to Clean Fuels. *ACS Catal.* **5**, 2640−2658 (2015).

84. Chu, W., Xu, J., Hong, J., Lin, T. & Khodakov, A. Design of efficient Fischer Tropsch cobalt catalysts via plasma enhancement : Reducibility and performance (Review). *Catal. Today* **256**, 41–48 (2015).

85. Mukenz, T. M. FISCHER-TROPSCH REACTION : Towards understanding the mixed iron-cobalt catalyst systems. PhD Thesis (University of the Witwatersrand, Johannesburg, 2010).

86. Macheli, L. Co_3O_4-Nanocubes modified with TEOS as models to study support interactions in cobalt-based Fischer-Tropsch catalysts. MSc Dissertation (University of Cape Town, Cape Town, 2014).

87. Tauster, S. J., Fung, S. C., Baker, R. T. K. & Horsley, J. A. Strong Interactions in Supported-Metal Catalysts. *Science, New Series* **211**, 1121–1125 (1981).

88. Dlamini, M. W. Spherical carbons as model supports for Fe , Co and Fe-Co Fischer-Tropsch catalysts. PhD Thesis (University of the Witwatersrand, Johannesburg, 2016).

89. Liu, J., Wang, P., Xu, W. & Hensen, E. J. M. Particle Size and Crystal Phase Effects in Fischer-Tropsch Catalysts. *Engineering* **3**, 467–476 (2017).

90. van Heerden, T. & van Steen, E. Metal – support interaction on cobalt based FT catalysts – a DFT study of model inverse catalysts. *Faraday Discuss.* **197**, 87–99 (2017).

91. Gnanamani, M. K., Jacobs, G., Shafer, W. D. & Davis, B. H. Fischer-Tropsch synthesis: Activity of metallic phases of cobalt supported on silica. *Catal. Today* **215**, 13–17 (2013).

92. Kitakami, O., Sato, H., Shimada, Y., Sato, F. & Tanaka, M. Size effect on the crystal phase of cobalt fine particles. *Phys. Rev. B* **56**, 13849–13854 (1997).

93. Fischer, N., van Steen, E. & Claeys, M. Preparation of supported nano-sized cobalt oxide and fcc cobalt crystallites. *Catal. Today* **171**, 174–179 (2011).

94. Storsæter, S., Tøtdal, B., Walmsley, J. C., Tanem, B. S. & Holmen, A. Characterization of alumina-, silica-, and titania-supported cobalt Fischer-Tropsch catalysts. *J. Catal.* **236**, 139–152 (2005).

95. Xiong, H., Motchelaho, M. A. M., Moyo, M., Jewell, L. L. & Coville, N. J. Correlating the preparation and performance of cobalt catalysts supported on carbon nanotubes and carbon spheres in the Fischer-Tropsch synthesis. *J. Catal.* **278**, 26–40 (2011).

96. Garces, L. J., Hincapie, B., Zerger, R. & Suib, S. L. The Effect of Temperature and Support on the Reduction of Cobalt Oxide: An in Situ X-ray Diffraction Study. *J. Phys. Chem. C* **119,** 5484–5490 (2015).

97. van Dijk, H. A. J., Hoebink, J. H. B. J., Schouten, J.C. The Fischer-Tropsch synthesis: A mechanistic study using transient isotopic tracing. *Chem. Eng. Sci.* **56**, 1211-1748 (2001).

98. Tsakoumis, N. E., Rønning, M., Borg, Ø., Rytter, E. & Holmen, A. Deactivation of cobalt based Fischer–Tropsch catalysts : A review. *Catal. Today* **154**, 162–182 (2010).

99. Mogorosi, R. . Metal-support interaction on Fe-based Fischer-Tropsch catalysts. PhD Thesis (University of Cape Town, Cape Town, 2012).

100. Rodríguez, J. A. & Hrbek, J. Surface Science Inverse oxide/metal catalysts : A versatile approach for activity tests and mechanistic studies. *Surf. Sci.* **604**, 241–244 (2010).

101. Karimi, S., Tavasoli, A., Mortazavi, Y. & Karimi, A. Cobalt supported on Graphene -A promising novel Fischer-Tropsch synthesis catalyst. *Appl. Catal. A Gen.* **499**, 188–196 (2015).

CHAPTER 3: SYNTHESIS AND CHARACTERIZATION OF CDOTS AND N-DOPED CDOTS

3.1 Introduction

Synthesis of carbon dots (Cdots) from a variety of carbon precursors and a wide range of synthesis techniques has broadened the extent of this developing field significantly[1,2]. Earlier on in their discovery, Cdots were derived from breaking down larger carbon nanomaterials by means of the "top-down" methods[1,2]. However, many of the current synthesis studies are based on building up Cdots from smaller carbon precursors such organic molecules and food products using the "bottom-up" methods[3]. The "bottom-up" methods can be used to synthesize Cdots from a large library of carbon precursors using readily available laboratory facilities[3–5]. Microwave-assisted reactions are one of the fast and simple "bottom-up" method commonly used for the synthesis of Cdots that have controlled size and high purity[6–8]. The aim of this work is to outline the synthesis of functionalized Cdots using microwave-assisted reactions, and compare their characteristics (structural, chemical, thermal and optical properties) to those reported in the literature. This section gives the detailed synthesis methods used to obtain gram quantities of Cdots and N-doped Cdots. Four different precursors, namely ascorbic acid, sucrose, chitosan and urea were used for the synthesis of functionalised Cdots.

It is well known that the chemical properties of Cdots are affected by the chemical make-up of the precursor molecules[4,9]. In this study, ascorbic acid and sucrose were selected for the synthesis of Cdots, while ascorbic acid with urea and chitosan were used for the synthesis of N-doped Cdots. Ascorbic acid and sucrose are both cyclic hydrocarbons containing six and eleven oxygen (O) atoms, respectively. The X-ray diffraction (XRD) patterns of both these structures show that they are crystalline. However, carbonization of these two molecules to give the formation of Cdots results in an amorphous peak at 2θ between 20 and 30 ° in the XRD pattern[10,11]. The Cdots particle sizes may also differ depending on the precursor type and the synthesis procedure[9]. Therefore structural, chemical, thermal and optical properties of Cdots from ascorbic acid and Cdots from sucrose were compared.

In the synthesis of N-doped Cdots from ascorbic acid and urea, ascorbic acid acts as a carbon source and urea as a nitrogen (N) source[12]. Chitosan however is a very unique polymer that shows the presence of both O- and N-functional groups (as seen in **Scheme 3.3**), and

therefore produce N-doped Cdots[13]. The structural, chemical, thermal and optical properties of these two types of N-doped Cdots are expected to be different. Since the types of N sources used were different, the N content as well as the type of N-functional groups found in these syntheses were determined and compared.

3.2 Synthesis of Cdots and N-doped Cdots

The synthesis methods followed in this work were obtained from the literature; except for the microwave-assisted synthesis of Cdots from sucrose and oleic acid, which has not been previously reported. Cdots and N-doped Cdots were synthesized using an Anton-Paar Multiwave 3000 SOLV system, with maximum power and controlled pressure of 1400 W and 60 bars, respectively. The microwave power was set manually, and in each case the reaction power was ramped for 10 min. The temperature of carbonization of precursors to Cdots was set manually as the maximum temperature (or infrared temperature limit on the microwave) of the reaction mixture. The microwave exposure time was the time it took for the reaction mixture to reach the set maximum temperature, at a fixed power (i.e. after ramping). The reaction conditions are summarized in **Table 3.1** below.

Table 3.1: Cdots and N-doped Cdots microwave-assisted synthesis conditions

Reaction No.	Carbon source (g)	Nitrogen source (g)	Solvent (mL)	Power (W)	Temperature (°C)	Time (min)
1	Ascorbic acid (6)	-	Water (600)	900	180	10
2	Sucrose (40)	-	Oleic acid (80)	600	200	30
3	Chitosan (6)	Chitosan -	Water (600)	600	200	5
4	Ascorbic acid (24)	Urea (24)	Water (240)	600	140	1

The step-by-step reaction procedures were carried out as follows:

For reaction no. 1, 3 and 4, in the first step, precursors are mixed with distilled water in a 1 L beaker according to the quantities mentioned in **Table 3.1**. Thereafter, 4 × 60 mL of homogeneous mixture containing reaction precursors were measured using a 100 mL

measuring cylinder and transferred into 4 × 100 mL microwave reaction vessels as represented by **Figure 3.1**. For the synthesis of N-doped Cdots from chitosan, 5 × 15 mm magnetic stirrer bars were also included in the reaction vessels since chitosan sparingly dissolved in water even after the mixture was sonicated for an hour.

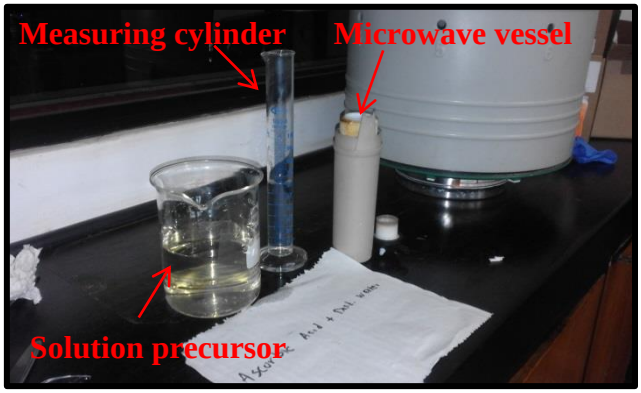


Figure 3.1: Sample preparation for microwave-assisted synthesis

In the second step, the vessels were sealed with vessels caps and placed inside liners and pressure jackets. The vessels were then placed on a rotor (**Figure 3.2a)**) and the rotor was covered, and inserted in the microwave (**Figure 3.2b)**) as illustrated below.

a) **b)**

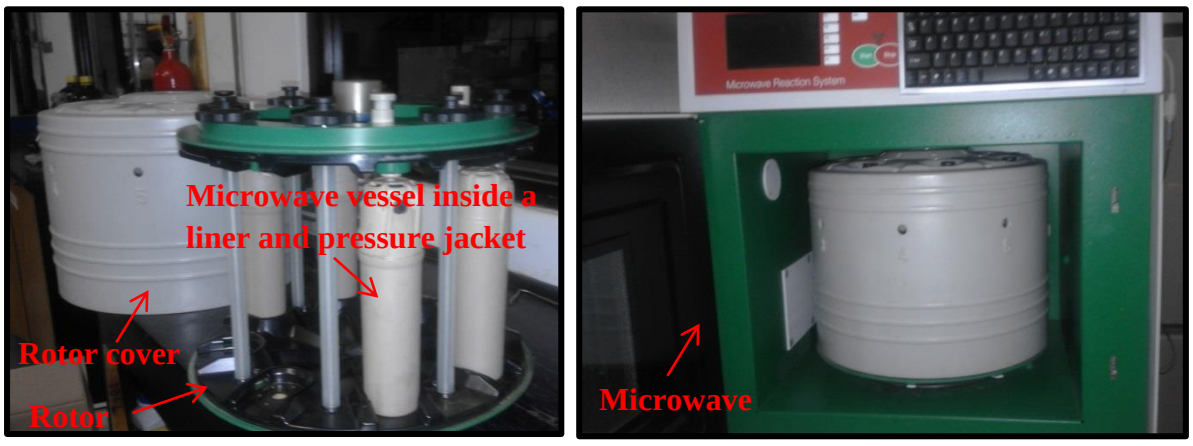


Figure 3.2: **a)** Microwave rotor set-up before synthesis, and **b)** microwave oven

All reaction mixtures were colourless to whitish before the reaction, and turned brown after microwave treatment, symbolizing carbonization. After the reaction, the mixtures were allowed to cool to room temperature, thereafter the mixtures were centrifuged at 15000 rpm

for 15 min to separate the precipitates (large carbon agglomerates) from the supernatants (Cdots or N-doped Cdots), as seen in **Figure 3.3**.

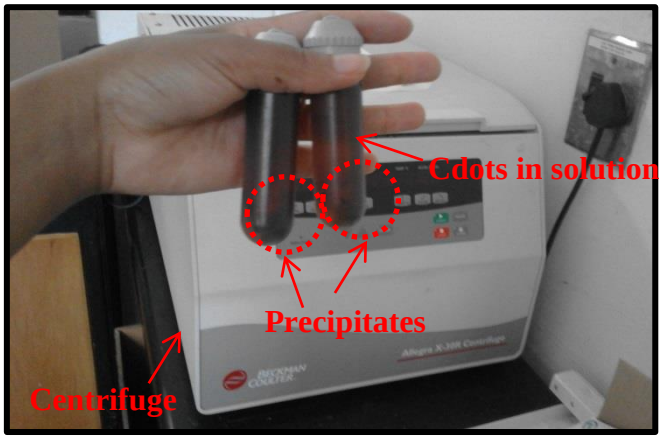


Figure 3.3: Purification of the product by centrifugation

The Cdots and N-doped Cdots solutions were then dried by rotary evaporation, at 60 °C (shown in **Figure 3.4a)**) until they showed no solvent condensing into the collection bottle. Thereafter the samples were further dried in an oven at 40 °C for 3 days, to obtain a brown solid product (**Figure 3.4b)**). The as prepared Cdots and N-doped Cdots were then taken for analysis.

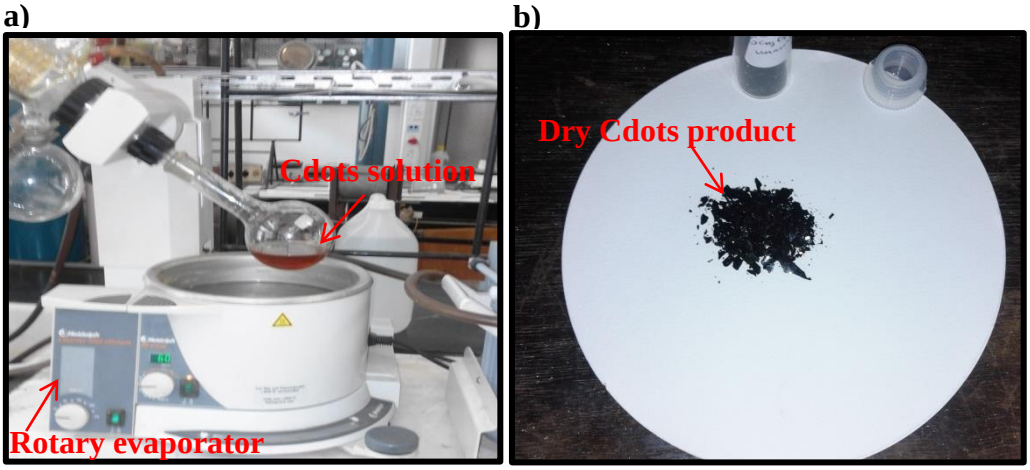


Figure 3.4: Cdots product **a)** before and **b)** after drying

For reaction no. 2 (**Table 3.1),** sucrose was used as a carbon source and oleic acid as a solvent. The first step was to prepare 4 × 20 mL of reaction mixture and to include a 5×15 mm magnetic stirrer bar in each vessel. The reaction mixture was bubbled with N_2 gas (to provide an inert atmosphere) before sealing the vessels. After the microwave treatment, the reaction was allowed to cool to room temperature. After cooling, 50 mL distilled water was

added to the reaction mixture to dissolve the greasy product. Thereafter, 50 mL normal hexane (n-hexane) was added to the solution to remove unreacted oleic acid. The mixture was transferred into a separating funnel as shown in **Figure 3.5a)**, and the products were separated from the starting material. The Cdots were collected from the solution at the bottom of the separating funnel containing water, while the top layer was also collected and then discarded. n-Hexane was added to the Cdots solution (about 5 times) until only one layer was present in the separating funnel. Afterwards, the mixture was further purified by dialysis using distilled water and 500 Da dialysis membranes for 3 days using to remove by-products, as shown in **Figure 3.5b)**. The Cdots were dried the using the same procedure described above.

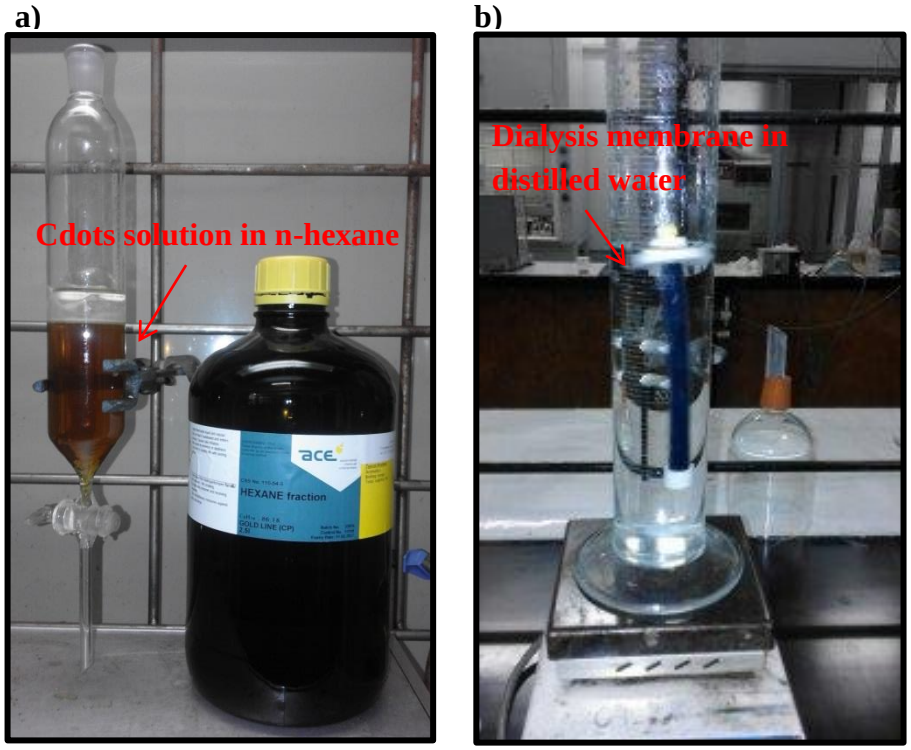


Figure 3.5: **a)** Separation of sucrose Cdots from unreacted oleic acid, and **b)** sucrose Cdots dialysis set-up

3.3 Characterization techniques

The structural properties of Cdots and N-doped Cdots (including their crystallographic nature, morphology and size) were determined by the techniques listed below.

3.3.1 X-ray diffraction: XRD

The phase composition of Cdots, N-doped and their carbon (and nitrogen) sources were determined using a Bruker D2 phaser low- and wide-angle *ex-situ* X-ray diffractometer equipped with a Co Kα X-ray source operating at 30 kV and 10 mA. A small amount (mg) of solid samples were first deposited on a silica supported zero background. The measurements were taken between 2θ = 10-90 °, with a 0.026 ° step.

3.3.2 Transmission electron microscopy: TEM

The particle size distribution and morphology of the as prepared Cdots and N-doped Cdots were determined using a FEI G^2 TECNAI Spirit T12, with a high powered beam of electrons accelerated at 120 kV. The samples were re-dispersed in distilled water. Each sample solution was dropped to a carbon coated copper grid and the grids were allowed to air dry before being analysed.

3.3.3 Scanning electron microscopy: SEM

SEM was used to determine the morphology of the Cdots and N-doped Cdots using a FEI Nova Nanolab 600 FIB with electrons were accelerated at 5 eV. The samples were dispersed in water, and the sample solution was dropped on a copper tape on an aluminium stub and allowed to air dry. The carbon tape was further coated with a palladium/gold coating before analysis.

3.3.4 Raman spectroscopy

Raman analyses were performed in order to determine the degree of disorder in the Cdots and N-doped Cdots. Raman spectra were determined using a Bruker Raman Senterra spectrometer with laser excitation of 532 nm and at 0.2 mV laser power and 15 s integration time. The samples were measured in their solid state, and the measurements were done on a glass substrate.

To study the surface chemistry of the prepared Cdots and N-doped Cdots, the following spectroscopy techniques were used:

3.3.5 Fourier transform infrared spectroscopy: FT-IR

The chemical bonds present in the Cdots and N-doped Cdots were determined from the IR absorption bands using a Brucker TENSOR 27 FT-IR spectrometer. The measurements were performed on solid samples under ambient conditions. The samples were scanned between 4000 and 500 cm^{-1}, using 64 scans.

3.3.6 X-ray photoelectron spectroscopy: XPS

XPS was used to determine the binding energies of the electrons extracted from the samples. The binding energy peaks gave information about the elemental composition as well as chemical bonds present in Cdots and N-doped Cdots. The measurements were recorded on the Physical Electronics Quantum 2000, using a monochromatic Al Kα source operating at 1486.7 eV. Sample preparation and analyses were done at NMISA, CSIR.

3.3.7 Thermogravimetric analysis: TGA

The TGA was used to determine the thermal stability of the Cdots and N-doped Cdots under air. The analyses were performed on a PerkinElmer Pyris STA6000. The sample (5-10 mg) was placed in an alumina crucible and subjected to temperatures from 35 to 900 °C, at 10 °C/min increment rate. N_2 gas (20 mL/min flow rate) was used as a purge gas, and air (10 mL/min) as an analysis gas. The weight loss (TG) and derivative thermal gravimetric (DTG) curve were obtained were measured and obtained from the Pyris software after analysis.

3.3.8 Photoluminescent: PL

PL spectroscopy was used to determine the light emission properties of the Cdots and N-doped Cdots. Solid state PL measurements were taken from a Horiba LabRAM HR micro-Raman spectrometer (frequency-double Lexel SHG argon ion laser). The sample measurements were taken from a silica substrate. The samples were excited at 244 nm and the measurements were taken between 350 and 800 nm.

3.3.9 Ultra-violet-visible: UV-vis

UV-vis spectroscopy was used to determine the light absorption properties of Cdots and N-doped Cdots. UV-vis analyses were carried out on a Agilent Technologies Cary (100) Series UV-Vis spectrophotometer, using a tungsten halogen light source. The samples were dispersed in distilled water for measurements. The samples were excited at 350 nm and the

measurements were taken between 200 and 800 nm, however the spectra were drawn only from the 200-500 nm range.

3.3.10 Product yield calculation

The Cdots and N-doped Cdots yield was calculated by dividing the final product mass by the amount of carbon starting material, as shown by **eq. 3.1** below:

$$\% \text{ yield} = \frac{\text{Cdots (g)}}{\text{carbon source (g)}} \times 100\ \% \quad \text{..... eq. 3.1}$$

3.4 Results and Discussions

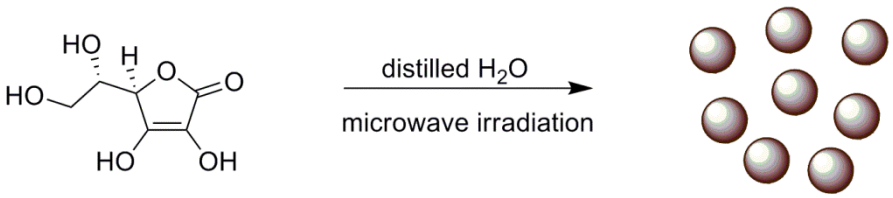
In this section, the experimental results are discussed and compared with the results obtained from the literature using the same or similar procedure. The physicochemical properties of Cdots and N-doped Cdots are also discussed, as well as some of the analysis challenges.

3.4.1 Synthesis

The syntheses procedures as well as the yields of Cdots and N-doped Cdots are discussed below:

Synthesis of Cdots from ascorbic acid

The synthesis procedure for making Cdots from ascorbic acid and water were obtained from Gong *et al.*[10], and the procedure is represented in **Scheme 3.1** below. They obtained 3.0 nm Cdots nanoparticle by a 5 min microwave treatment of the same precursors. The yield of the product was not reported. In this study, 5 min microwave treatment of ascorbic acid in distilled water did not yield any product; the mixture was colourless before and after microwave treatment. This is because the carbonization temperature (180 °C as noted in **Table 3.1**) could not be reached after 5 min. Therefore the reaction time was recorded after the temperature of the mixture reached 180 °C, which was found to be 10 min. The reaction produced a fairly good yield of product (28 %).

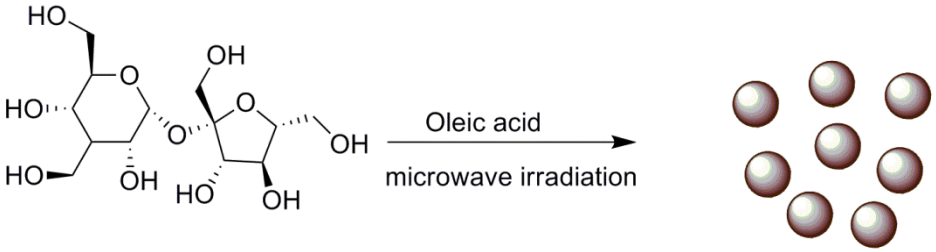


Scheme 3.1: A simple reaction scheme for the Cdots synthesis using ascorbic acid as a carbon source

Synthesis of Cdots from sucrose

Chen *et al.*[11] synthesized Cdots from sucrose and oleic acid using a hot oil bath method at 215 °C (5 min), to obtain 42 % yield of Cdots with average size of 1.8 nm. In this study, this procedure was used for the synthesis of Cdots using the microwave treatment method, summarized in **Scheme 3.2** below. The synthesis conditions are recorded in **Table 3.1** and the yield obtained was 60 %. The increase in product yield could be due to the advantage of the microwave irradiation over a traditional heating method as discussed in **CHAPTER 2**. Microwave irradiation provides direct and uniform heating, while the hot oil bath does not[6].

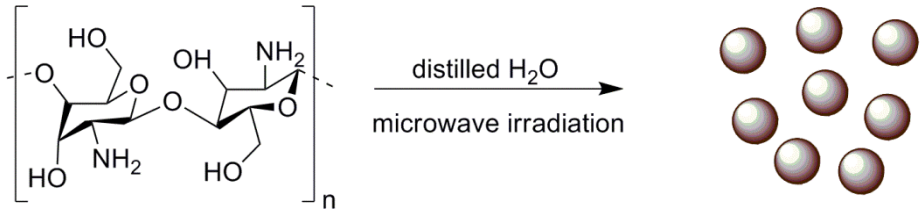
This might have contributed to the increase in carbonization of sucrose to the desired product. For this reaction, oleic acid was used as both the solvent and the capping agent. Replacing oleic acid with distilled water did not lead to any carbonization.



Scheme 3.2: A simple reaction scheme for the Cdots synthesis using sucrose as a carbon source

Synthesis of N-Cdots from chitosan

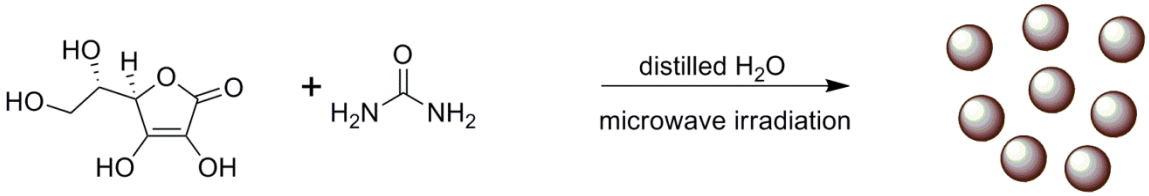
Xiao *et al.*[14] reported the synthesis of N-doped Cdots from the microwave-assisted reaction between chitosan and water. N-doped Cdots with particle sizes of 4.6 nm were obtained, however the authors did not report the reaction temperature or product yield. For the synthesis reported here, the conditions reported in **Table 3.1** (and **Scheme 3.3**) were used. The carbonization temperature was determined by trial and error. Initially, chitosan and water were treated in the microwave oven at 900 W (as in the Cdots-1 synthesis). However, it was noticed that during the synthesis, the reaction pressure increased drastically to pressures above 50 bar, while the reaction temperature was still at 150 °C. Due to this, the reaction power was changed to 600 W, to avoid a possible microwave explosion due to the high pressures. The N-doped Cdots were obtained in a fairly good yield of 21 %.



Scheme 3.3: A simple reaction scheme for the N-doped Cdots synthesis using chitosan as both a carbon and nitrogen source

Synthesis of N-Cdots from ascorbic acid and urea

Another type of N-doped Cdots material was prepared by a procedure described by Siriarti and Darmawan[12]. In their synthesis, the authors used ascorbic acid and different urea concentrations (0 %, 10 %, 25 %, 50 % and 75 %), and only reported the result for the synthesis that gave the highest PL emission intensity, i.e when 75 % urea concentration was used and 18 nm sized N-doped Cdots were obtained. In this study, the synthesis procedure used by Siriarti and Darmawan[12] was modified to the conditions mentioned in **Table 3.1**, and summarized by **Scheme 3.4** below.



Scheme 3.4: A simple reaction scheme for N-doped Cdots synthesis using ascorbic acid as both a carbon source and urea as a nitrogen source

The synthesis results show that microwave-assisted procedure provided a simple way of synthesizing Cdots and N-doped Cdots in a scalable manner. The characterization results are discussed below. For simplicity, **Scheme 3.1**, **3.2**, **3.3** and **3.4** represent the formation of Cdots-1, Cdots-2, N-doped Cdots-1 and N-doped Cdots-2, respectively.

3.4.2 Structural properties

3.4.2.1 X-ray diffraction: XRD

The XRD patterns of Cdots-1, Cdots-2, N-doped Cdots-1 and N-doped Cdots-2 are represented in **Figure 3.6a) - d)** below. The results show a peak between 2θ of 20 and 25 °, which is typical for carbon with a poorly crystalline nature[9,15]. These humps appear close to the (002) plane of a graphitic structure, which typically appears at 2θ = 26 ° [16,17]. The amorphous peak may due to the presence of surface functional groups causing disorder of the sp^2 type carbon layers and/or the presence of amorphous sp^3 type diamond like carbon[9,10,13]. A similar peak has been reported for CSs, HCSs and CNTs, which are known to be carbon allotropes with disorder of the sp^2 type graphitic flakes carbon[18,19].

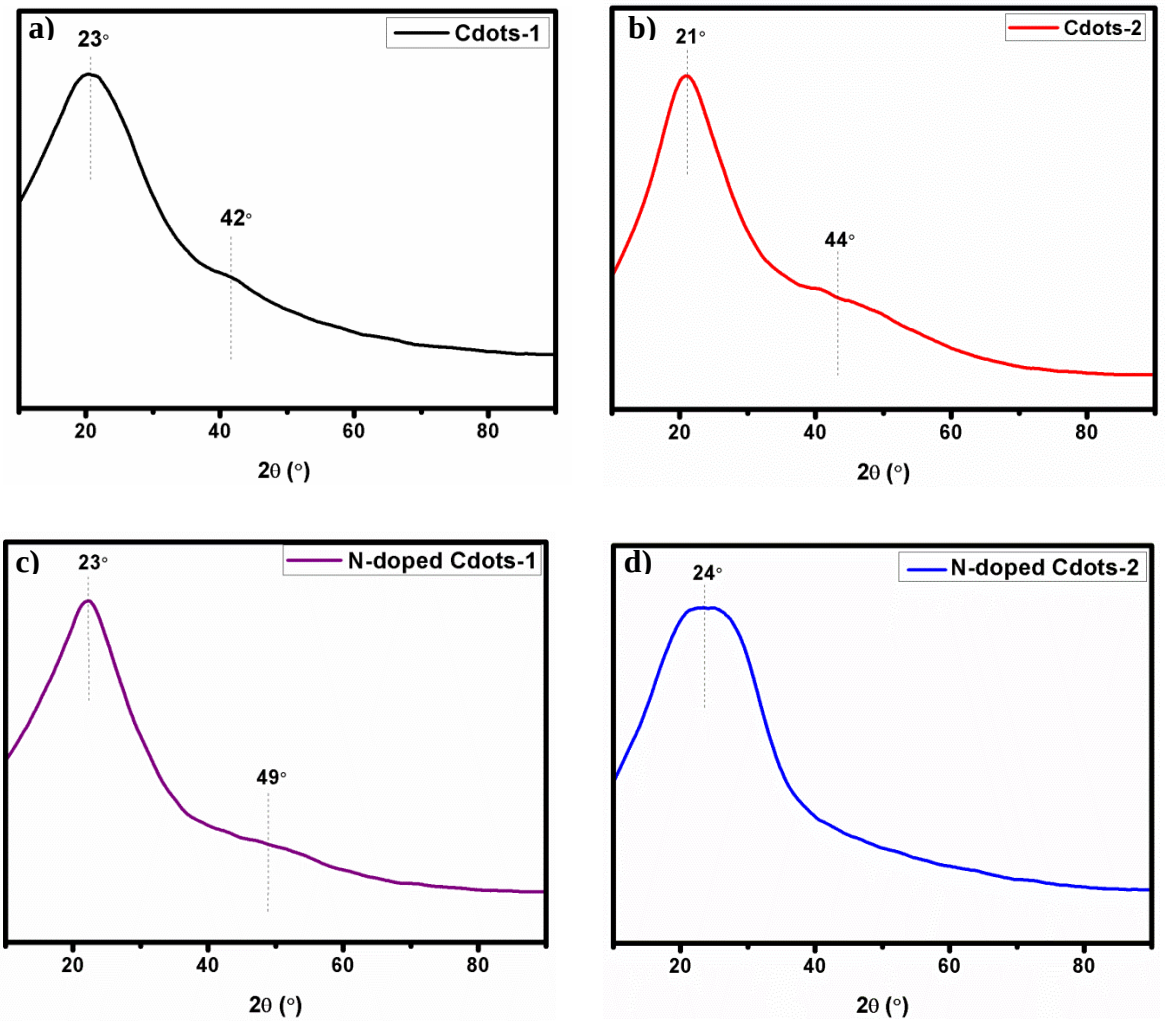


Figure 3.6: XRD patterns **a)** Cdots-1, **b)** Cdots-2, **c)** N-doped Cdots-1, and **d)** N-doped Cdots-2

It has been noted that the more disordered the sp^2 type carbon layers of carbon nanomaterials are, the broader the peak at 2θ between 20 and 25 ° [20]. The XRD patterns in **Figure 3.6a) - d)** suggest that the Cdots-1 and N-doped Cdots-2 synthesized using ascorbic acid are more disordered than the Cdots-2 and N-doped Cdots-1. This suggests that ascorbic acid forms highly amorphous Cdots. The XRD patterns of the Cdots-1, Cdots-2 and N-doped Cdots-1 also shows a shoulder around 2θ of 40-49 °, which is in the region of the (101) plane of graphitic carbon[21]. The presence of the 2θ = 20-25 ° and 2θ = 40-49 ° peaks suggests that the Cdots and N-doped Cdots are partially graphitic. The XRD pattern of N-doped Cdots-2 only showed one broad peak at 24 ° as seen in **Figure 3.6d)**, typical of N-doped Cdots with high nitrogen content[22]. The XRD patterns of the starting precursors may be found in supplementary **Figure S3.1a-d**, which shows that all starting precursors are purely crystalline materials in contrast to the end product, except for chitosan, which contains peaks at

2θ = 11 °,23 ° and 43 °. The 2θ at 23 ° corresponds to the crystalline nature of chitosan, while the two peaks at 11 and 43 ° degrees are attributed to the amorphous nature[13,23].

Confirmation of chitosan carbonization

It has been shown in **Figure 3.6c)** that the XRD pattern of N-doped Cdots-1 (synthesized from chitosan) also has a peak at 2θ = 23 °. It was therefore difficult to confirm complete carbonization of chitosan from XRD results as with other crystalline precursors. Other properties (chemical and optical properties) of N-doped Cdots were determined and compared with chitosan. The FT-IR and PL spectra of N-doped Cdots-1 vs chitosan are shown in **Figure 3.7a)** and **b)**, respectively**.** The FT-IR spectrum shows the peak intensities of the O-H and C-O-C peaks in N-doped Cdots-1 have decreased relative to the starting material. The peak between 1152 and 877 cm^{-1} is associated with the C-H bending vibration of the pyranose ring (or heterocyclic ring) in chitosan[13]. This peak is significantly reduced after carbonization as a result of the decomposition of the pyranose ring during carbonization[13,14]. The FT-IR spectrum of N-doped Cdots-1 also shows a weak peak between 1152 and 890 cm^{-1} which may be ascribed to the C-H bending vibrations. The decrease in intensity of the observed N-doped Cdots-1spectrum suggests decomposition of the chitosan structure during carbonization, and since there are no peaks in the N-doped Cdots-1 identical to the chitosan peaks, this may also suggest that chitosan was completely carbonized. The FT-IR results are very similar to those reported by Xiao *et al.*[14] for the same reaction. The PL spectra also showed that only N-doped Cdots-1 has a strong PL absorption peak at 517 nm, while chitosan does not fluoresce. This also confirmed that chitosan was completely carbonized. Therefore the XRD peaks seen for the N-doped Cdots-1 are due to the nature of its structure and not chitosan residues. These results show that the XRD can be most helpful in indicating complete carbonization of crystalline carbon and/or nitrogen precursors.

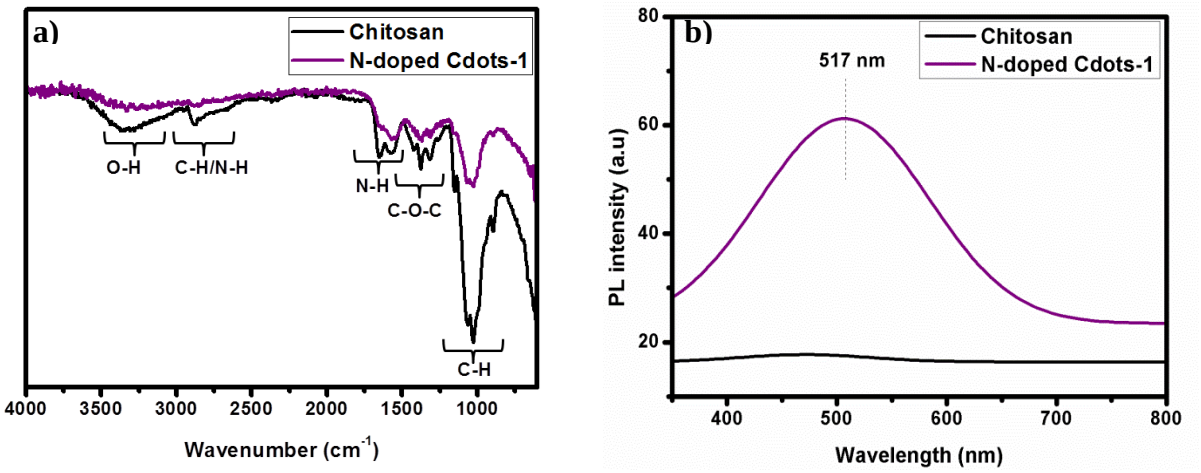


Figure 3.7: **a)** FT-IR and **b)** PL results for chitosan and N-doped Cdots-1

3.4.2.2 Scanning Electron Microscopy: SEM

The low resolution SEM image of Cdots-1 and N-doped Cdots-1 are shown in **Figure 3.8a)** and **b)**, respectively. The results show spherically shaped clusters of Cdots. There were no significant differences between SEM images of all four samples at this magnification. Supplementary **Figure S3.1a)** and **b)** has the SEM images of the Cdots-2 and N-doped Cdots-2 samples.

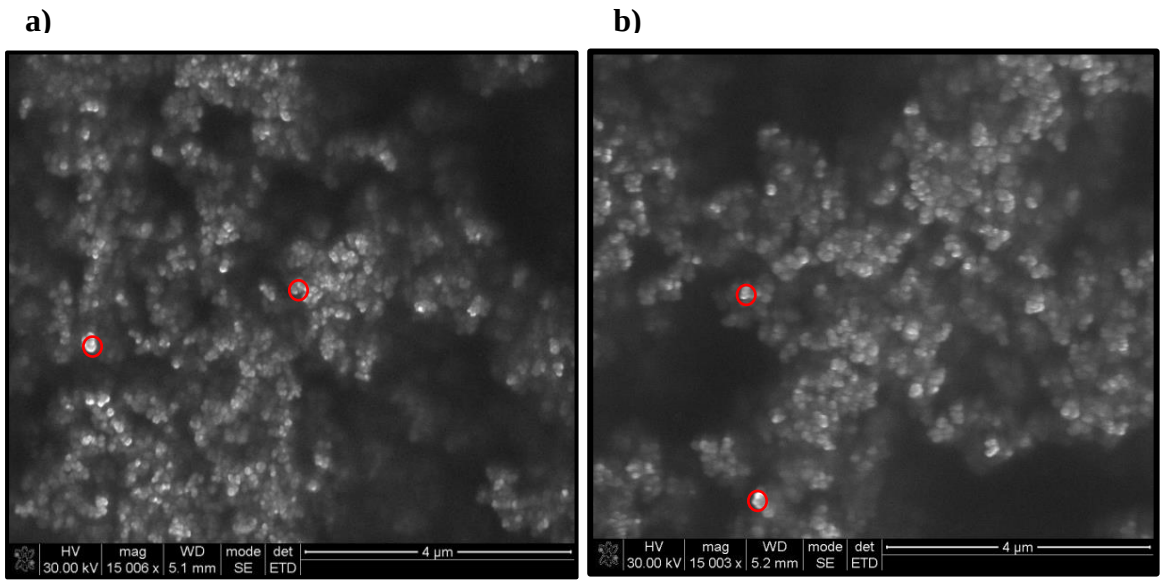


Figure 3.8: Low resolution SEM images of **a)** Cdots-1, as well as **b)** N-doped Cdots-1. The red circles in each image highlights some Cdots clusters

3.4.2.3 Transmission Electron Microscopy: TEM

The TEM images and size distribution histogram with a normal distribution curve of Cdots-1 are shown in **Figure 3.9a)** below. Due to limited access to a TEM instrument, only Cdots-1 was recorded at a fairly good resolution. The TEM image shows the sphere-like shaped nanoparticles, which agrees with the literature reports[9,10,24]. The average diameters were determined for 100 nanoparticles collected from different TEM images at the same scale. The average diameter was found to be 4.1 $\pm$1 nm, which is very similar to the 3.0 nm average diameter obtained by Gong *et al.* (2015)[10]. A low resolution N-doped Cdots-1 TEM images is also shown in **Figure 3.9b)**. The particles size distribution could not be determine because the particles on the TEM image are very small.

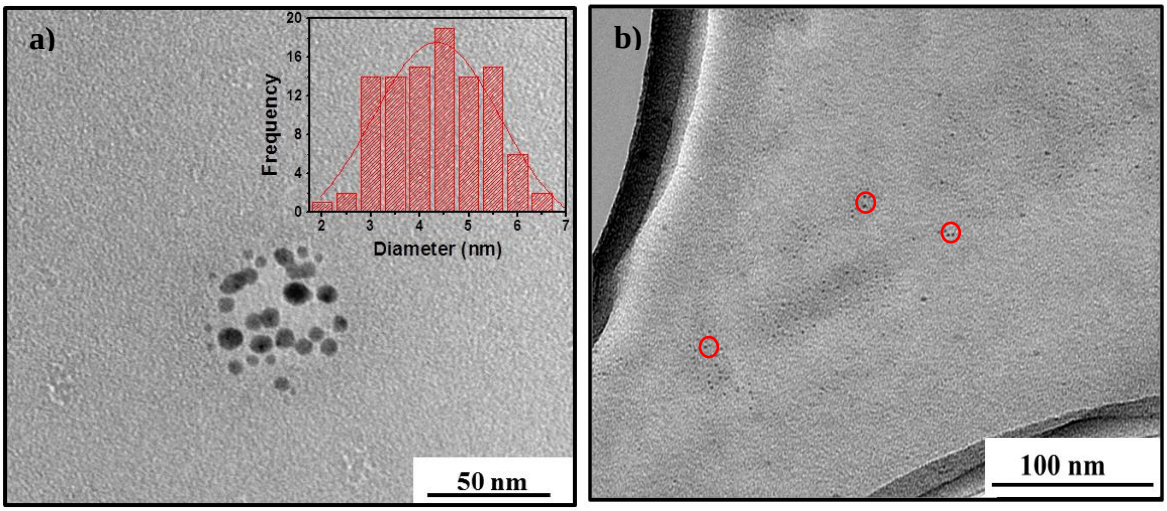


Figure 3.9: **a)** TEM image with an inserted particle size distribution histogram and a normal distribution curve of Cdots-1, and **b)** a low resolution TEM image of N-doped Cdots-1. The red circles highlight Cdots that can be seen from the grid

3.4.2.4 Raman spectroscopy

Raman spectroscopy analyses were performed in order to determine the D bands (sp^3 graphitic type carbon) and the G bands (sp^2 graphitic type carbon) position and intensity and the corresponding I_D/I_G ratio of the Cdots and N-doped Cdots. Unfortunately in this case, the D and G bands could not be observed in the Raman spectra due to the excitation of fluorescing Cdots and N-doped Cdots by the Raman spectroscopy light source. The results may be seen in **Figure 3.10** below. It was suggested that a Fourier tranform Raman (FT-Raman) spectroscopy instead of the conventional Raman spectroscopy may be of good use

for analysis of these materials. This is because FT-Raman is able to reduce background fluorescence of materials. Further studies on this will be carried out at a later stage.

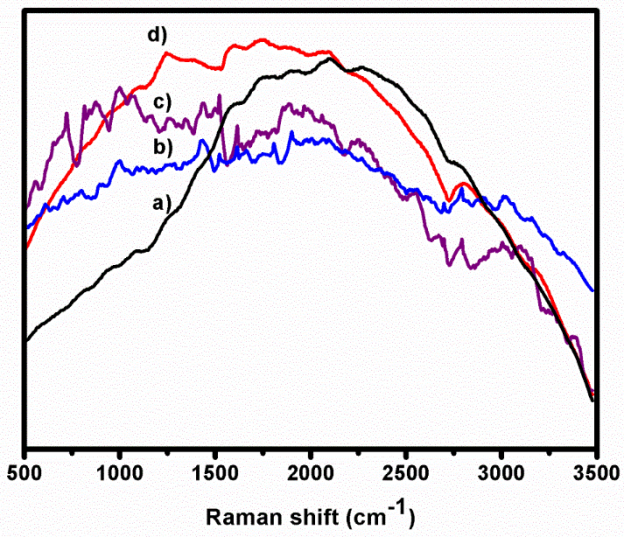


Figure 3.10: Raman spectra of **a)** Cdots-1, **b)** Cdots-2, **c)** N-doped Cdots-1, and **d)** N-doped Cdots-2

3.4.3 Chemical properties

Chemical properties of Cdots and N-doped Cdots were determined using FT-IR and XPS spectroscopy. The results are discussed below.

3.4.3.1 Fourier transform infrared spectroscopy: FT-IR spectroscopy

FT-IR spectroscopy was used to determine the functional groups present in Cdots and N-doped Cdots. **Figure 3.11** represents the FT-IR spectra of Cdots and N-doped Cdots. In **Figure 3.11a)**, the broad O-H stretch band for both Cdots appears at 3333 cm^{-1}, which may be attributed to the presence of water residue left behind after drying the sample, and/or multiple hydroxyl functional groups present on the surface of Cdots[10,11]. The low intensity bands between 2982 and 2899 cm^{-1} in Cdots-1 may be attributed to the aromatic C-H stretch. The band at 1733 cm^{-1}, may be ascribed to the C=C bending of aromatic rings. The band at 1607 cm^{-1} imply the presence of the carboxylic acid C=O group[11]. The peaks between 1500 and 1000 cm^{-1} corresponds to the asymmetry (alcohol C-O-C) and symmetric (ether C-O-C) stretching bands due, respectively. The C-H bands are more prominent in Cdots-1 compared to Cdots-2; this suggests that Cdots-1 has more sp^3 type carbon compared to Cdots-2. The high intensities of the O-H, C=O and C-O-C in both Cdots-1 and Cdots-2 suggests that these materials have high oxygen content.

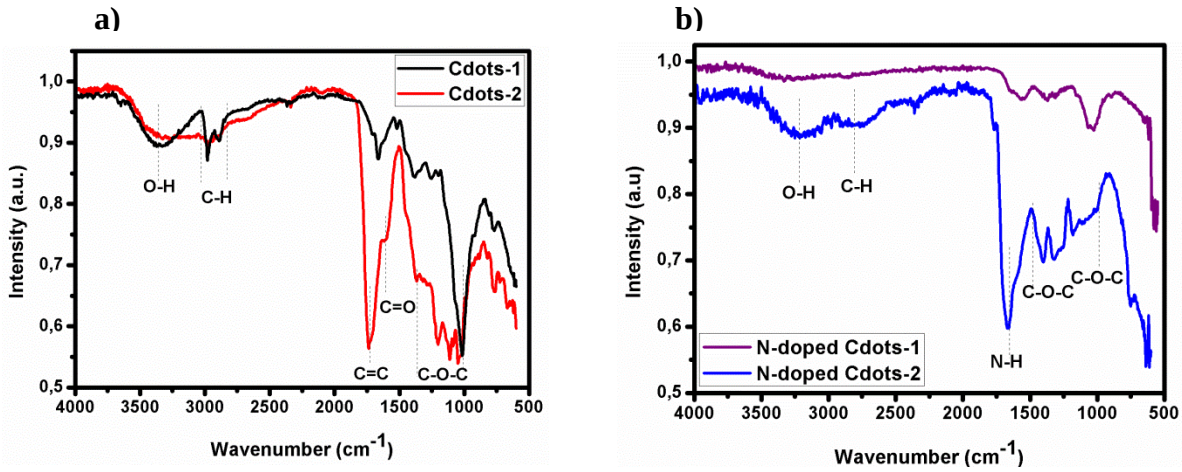


Figure 3.11: FT-IR spectra of **a)** Cdots and **b)** N-doped Cdots

Figure 3.11b) shows a broad peak at 3204 cm^{-1} due to the O-H stretching vibration. Another broad band at 2794 cm^{-1} in N-doped Cdots-2 corresponds to the C-H stretching vibration. This suggests the presence of sp^3 type carbon in the N-doped Cdots-2. The strong band at 1667 cm^{-1} may be ascribed to the N-H bending vibration, which appears with very high intensity in N-doped Cdots-2 than N-doped Cdots-1. This could mean that N-doped Cdots-2 have a high nitrogen content than N-doped Cdots-1. The last bands between 1500 and 1000 cm^{-1}, similar to those found in Cdots, also corresponds to the asymmetric and symmetric stretching bands associated with the C-O-C bonds, respectively.

3.4.3.2 X-ray photoelectron spectroscopy: XPS

XPS analyses were made to further study the surface chemistry of the Cdots and N-doped Cdots. XPS is a very useful technique in that it gives information about both the type and percentage of elements present in a sample[25]. **Figure 3.12** below shows the XPS survey spectra of Cdots and N-doped Cdots, with **a)**, **b)**, **c)** and **d)** representing Cdots-1, Cdots-2, N-doped Cdots-1 and N-doped Cdots-2, respectively. The survey spectra show that Cdots contains carbon (C1s) and oxygen (O1s), while N-doped Cdots contain carbon, oxygen and nitrogen (N1s). The C1s, O1s and N1s peaks appear at 285 eV, 530 eV and 400 eV, respectively.

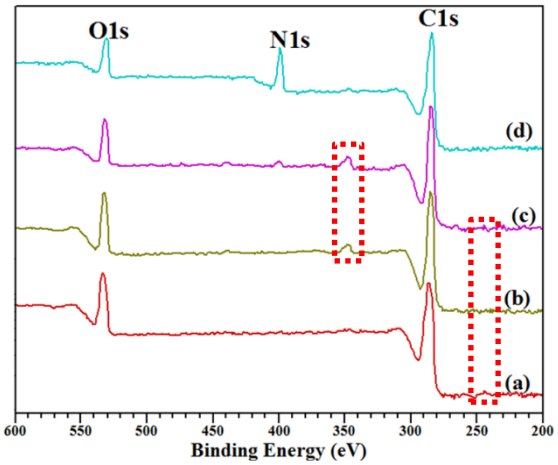


Figure 3.12: XPS spectra of **(a)** Cdots-1, **(b)** Cdots-2, **(c)** N-doped Cdots-1 and **(d)** N-doped Cdots-2

The peaks around 240 eV (very weak) and 350 eV in the XPS spectra (highlighted in **Figure 3.12** above), corresponds to silicon (Si, < 1 %) and calcium (Ca, < 1.5 %) impurities in each sample, which is due to equipment used during sample preparation. The Si is due to silica (SiO_2) which is a very stable complex which does not decompose even at 900 °C[26], while Ca is due to calcium carbonate ($CaCO_3$) which decomposes above 800 °C under air[27]. All Cdots and N-doped Cdots thermograms showed that there are no residuals left at 700 °C (as it will be seen in **section 3.4.4**), and therefore the Si and/or Ca present in the XPS data were not from the samples.

The relative abundance of the C (1s), O (1s) and N (1s) in each sample are summarized in **Table 3.2a)** below. The relative concentrations of different carbon, oxygen and nitrogen functional groups were obtained from spectral areas of the C (1s), O (1s) and N (1s) XPS peaks[25,28]. The chemical bonding configurations and their corresponding binding energies are tabulated in **Table 3.2 b)**, **c)** and **d)** and **e)** below. The relative concentrations of the bonding state in all the samples are recorded in **Table S3.2a)** and **b)** of the supplementary information. Since the amount of Si and Ca is very small compared to the bulk amount each sample, their contribution to the percentage oxygen and carbon (due to SiO_2 and $CaCO_3$) were neglected. However, the samples were also discarded after analyses to avoid contamination of the main batches of materials.

Table 3.2a): Percentage Atomic abundance in each sample

Sample	Relative atomic abundance (%)		
	C	**O**	**N**
Cdots-1	73.1	26.2	-
Cdots-2	75.8	23.0	-
N-doped Cdots-1	79.1	16.9	2.2
N-doped Cdots-2	68.8	15.2	15.9

Table 3.2b): Peak positions of C1s bonding states

Sample	Peak position (eV)				
	sp^2 C-C	**sp^2 C-N**	**sp^3 C-N/C-C**	**C=O**	**O-C=O**
Cdots-1	284.08	-	285.58	286.90	288.34
Cdots-2	284.06	-	285.25	286.04	287.33
N-doped Cdots-1	283.83	284.58	285.48	286.77	288.14
N-doped Cdots-2	283.80	284.54	285.42	286.64	288.04

Table 3.2c): Peak positions of O1s bonding states

Sample	Peak position (eV)		
	C=O	**O-C=O**	**C-O-C/C-OH**
Cdots-1	531.21	530.02	532.33
Cdots-2	530.87	530.33	532.57
N-doped Cdots-1	531.23	530.08	532.56
N-doped Cdots-2	531.08	530.26	533.68

Table 3.2d): Peak positions of nitrogen bonding states

Sample	Peak position (eV)			
	Pyridinic-N	**Pyrrolic-N**	**Graphitic-N**	**NOx**
N-doped Cdots-1	398.15	398.98	399.92	401.01
N-doped Cdots-2	398.10	399.08	399.98	400.94

Cdots-1 contains 73.1 wt% carbon and 26.2 wt% oxygen (reported in **Table 3.2a)**). The deconvoluted spectra of the C1s peaks shows four peaks at 284.1 eV, 285.6 eV, 286.9 eV and 288.3 eV corresponding to the sp^2 C-C, sp^3 C-C, C=O and O-C=O groups, respectively, as shown in **Figure 3.13a)**. The O1s peaks in **Figure 3.13b)** was also deconvoluted into two peaks which were matched to the C=O (531.2 eV) and O-C=O (530.0 eV). Another peak at 532.2 eV was also noted which corresponds to the C-O-C binding energy. These peaks suggest that the sp^3 type carbon bonds form to give the C-O-C type bond in the Cdots structure. These peaks are also observed to be present in the FT-IR of Cdots-1 in **Figure 3.11a)** above.

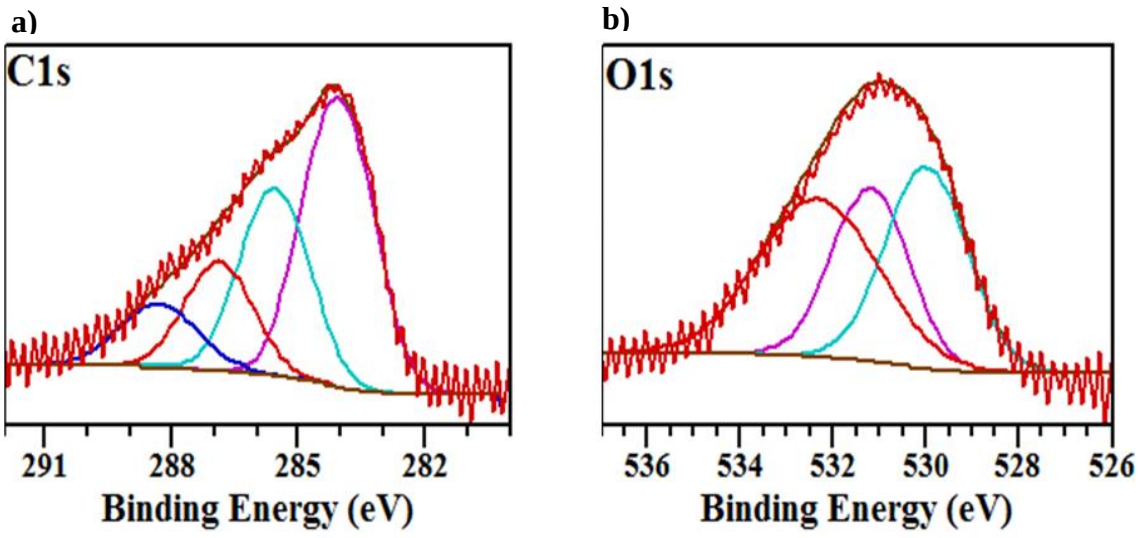


Figure 3.13: Expanded **a)** C1s and **b)** O1s survey XPS spectra of Cdots-1

Cdots-2 contains 75.8 wt% carbon and 23.0 wt% of oxygen as shown in **Table 3.2a)**. The expanded spectra of the C1s and O1s of Cdots-2 are shown in **Figure 3.14** below. The deconvoluted spectra of the C1s shows four peaks at 284.1 eV, 285.3 eV, 285.0 eV and 287.3 corresponding to the sp^2 C-C, sp^3 C-C, C=O and O-C=O groups, respectively. The

O1s peak was deconvoluted into three peaks at 530.9 eV, 530.3 eV and 532.6 eV corresponding to the C=O, O-C=O and C-O-C, respectively. These peaks are also in agreement with the functional groups noted in the FT-IR spectra of Cdots-2 shown in **Figure 3.11a)**.

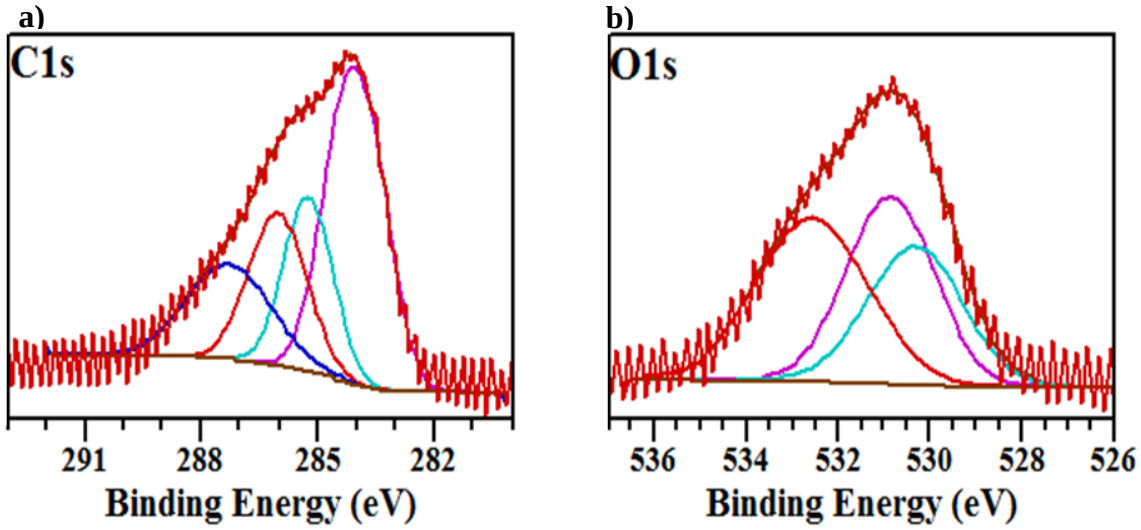


Figure 3.14: Expanded **a)** C1s and **b)** O1s survey XPS spectra of Cdots-2

The expanded peaks of Cdots-1 and Cdots-2 show very similar peaks and functional groups as expected. **Figure 3.15** below shows the possible chemical bonds and their positions in the structure of both Cdots, taken from a structure of the GO as reported in the literature[29].

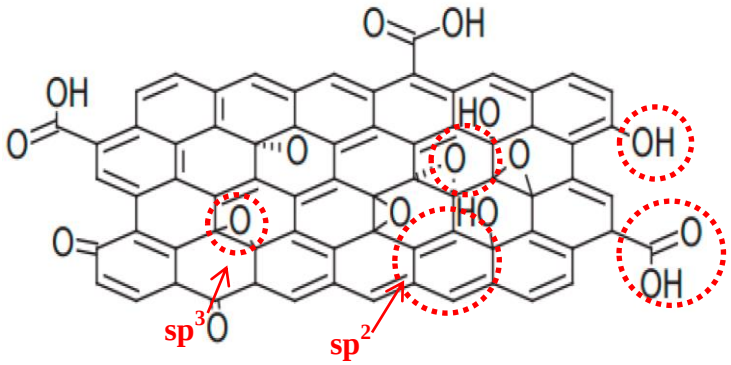


Figure 3.15: A structure showing the possible position of surface functional groups on Cdots as determined by C1s and O1s XPS survey deconvolution (after Ma *et al.*, 2017)[29].

Cdots-1 has a higher amount of O1s than Cdots-2. This is consistent with the very broad and intense C-O-C bonds found in the FT-IR spectra in **Figure 3.11a)**. The higher the oxygen content, the more disordered the carbon structure. This is seen in the XRD peak of Cdots-1

which is broader than the XRD peak of Cdots-2. Cdots-1 also has a very high content of sp^3 type carbon (27 wt% in **Table S3.2b)**), which was also prominent in the FT-IR spectra.

N-doped Cdots have similar chemical properties as found for the Cdots, except for the presence of nitrogen functional groups. N-doped Cdots-1 contains 79.1 wt% of carbon, 16.9 wt% of oxygen and 2.2 wt% of nitrogen (as reported in **Table 3.2a)**). The deconvoluted spectra of the C1s in **Figure 3.16a)** shows five peaks at 283.8 eV, 284.6 eV, 285.5 eV, 286.8 eV and 288.1 corresponding to the sp^2 C-C, N-C sp^2, sp^3 C-C/C-N, C=O and O-C=O groups, respectively. The O1s was also deconvoluted into three peaks at 531.2 eV, 530.1 eV and 532.6 eV, which corresponds to the binding energy of C=O, O-C=O and C-O-C, respectively (**Table 3.2b)**). The N1s peaks appear at 398.2 eV, 399.0 eV and 399.9 eV corresponding to the pyridinic, pyrrolic and graphitic nitrogen, respectively. A very weak peak at 401 eV was also observed, which signifies the presence of NOx (8 wt%) as shown in **Table S3.2c)**.

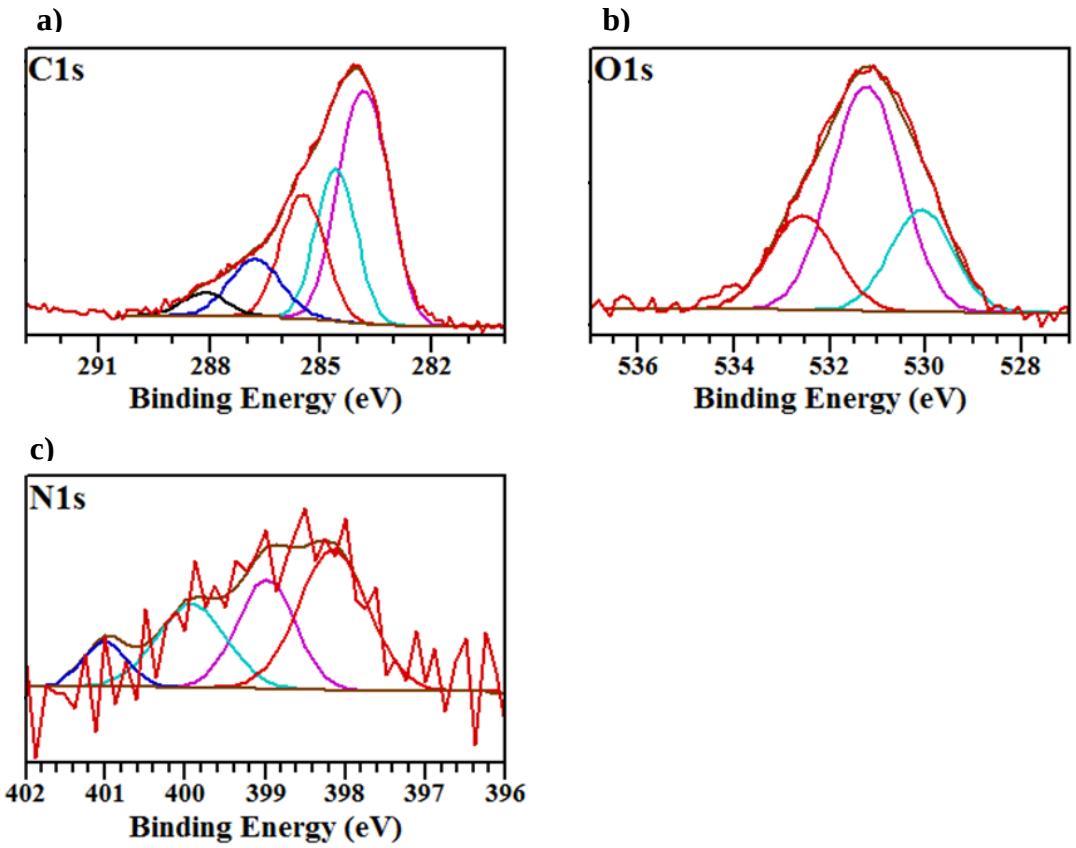


Figure 3.16: Expanded **a)** C1s, **b)** O1s and **c)** N1s survey XPS spectra of N-doped Cdots-1

N-doped Cdots-2 contains 68.8 wt% carbon, 15.2 wt% oxygen and 15.9 wt% nitrogen (as reported in **Table 3.2a)**). The deconvoluted spectra of the C1s shows four peaks at 283.8 eV,

284.5 eV, 285.4 eV, 286.6 eV and 288.0 also corresponding to the sp^2 C-C, N-C sp^2, sp^3 C-C/C-N, C=O and O-C=O groups, respectively, as shown in **Table 3.2b)**. The O1s was also deconvoluted into three peaks at 531.1 eV, 530.3 eV and 533.7 eV, which corresponds to the binding energy of C=O, O-C=O and C-O-C, respectively. The N1s peaks appear at 398.1 eV, 399.1 eV and 400.0 eV corresponding to the pyridinic, pyrrolic and graphitic nitrogen, respectively. A very weak peak at 400.9 eV was also observed, which signifies the presence of NOx, bearing a very small amount (5 wt %). The decovoluted XPS peaks of C1s, O1s and N1s are shown in **Figure 3.17** below. These peaks are comparable to the presence of functional groups noted in the FT-IR spectrum of N-doped Cdots -2 in **Figure 3.11b)** above. The pyridinic and pyrrolic nitrogen configuration is dominant in both N-doped Cdots-1 and N-doped-Cdots-2. It has been reported that iron (Fe) catalysts supported on N-doped carbon spheres (CSs) with predominantly pyridinic and pyrrolic nitrogen configurations were more active and selective towards long chain (C_{5+}) hydrocarbon under the Fischer-Tropsch (F-T) condition compared to Fe supported on N-doped CSs with predominantly graphitic configuration[30]. Therefore the N-doped Cdots are expected to give better metal stability compared to Cdots during F-T process.

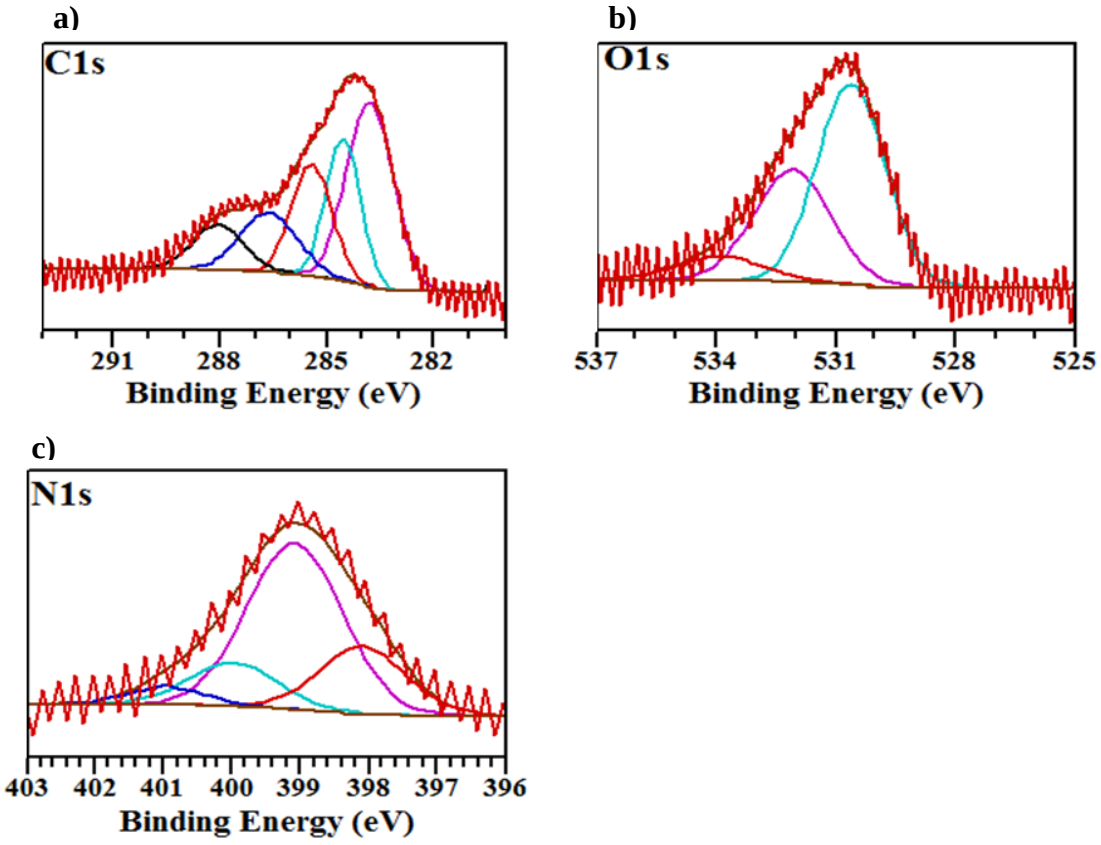


Figure 3.17: Expanded **a)** C1s, **b)** O1s and **c)** N1s survey XPS spectra of N-doped Cdots-2

The presence of nitrogen functional groups in both the FT-IR (N-H bands in **Figure 3.11b)**) and XPS spectra of N-doped Cdots confirmed that nitrogen was successfully incorporated in the structure of Cdots. **Figure 3.18** below shows different nitrogen domains that correspond to those expected from the surface of N-doped Cdots. The Figure is based on the structure of graphene, and this provides a model structure for the N-doped Cdots. N-doping with urea gave Cdots with a higher nitrogen content compared to chitosan. The low sp^2 type carbon and high nitrogen content could be the reason for the highly amorphous nature of the N-doped Cdots structure as seen in the XRD data in **Figure 3.8b)**. N-doped Cdots-2 also showed the highest content of pyrrolic N compared to N-doped Cdots-1, which was also confirmed by a very intense N-H peak in the FT-IR spectrum.

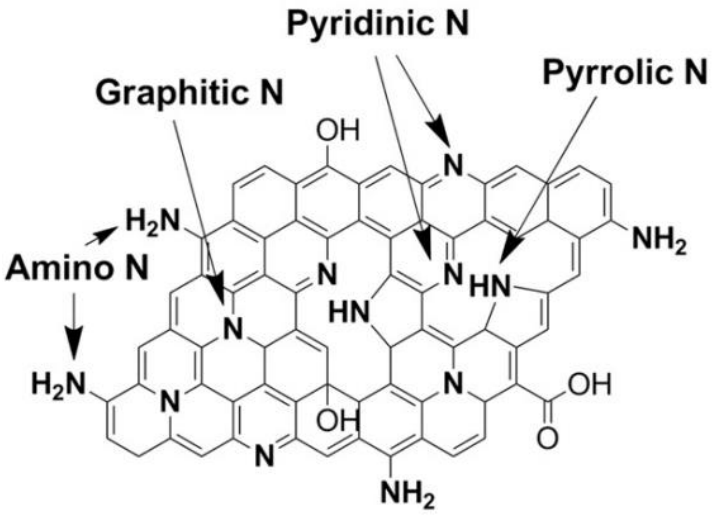


Figure 3.18: A structure showing the possible position of surface functional groups on N-doped Cdots as determined by N1s XPS survey deconvolution (adopted from Zhang *et al.*, 2012)[31]

3.4.4 Thermal stability: Thermal gravimetric analysis (TGA)

Thermal gravimetric analysis (TGA) was used to determine the thermal stability and composition of the Cdots and N-doped Cdots. TG analyses were performed on all samples, and the results are discussed below.

By measuring the amount and rate of change of the weight of material with respect to temperature under air conditions, the TG and DTG graphs of all four samples were obtained as shown in **Figure 3.19** and **3.20** below. The results were used to compare the thermal stability of both Cdots and N-doped Cdots.

Numerous research reports have indicated that graphitic carbon decomposes to CO and CO_2 at temperatures above 700 °C under air conditions, while carbon with amorphous properties starts decomposing at temperatures as low as 500 °C[18,32]. In the presence of heteroatoms in the carbon surface, the carbon nanostructure starts decomposing at 200 °C as a result of the removal of volatile and strongly anchored surface functional groups[33–35]. Kumar *et al.*[32] and Gao *et al.*[35] reported that GO (derived from graphite acid treatment) started decomposing around 200 °C, due to the presence of surface bound oxygen functional groups. On the other hand, graphite only started decomposing above 700 °C[32,] . Xiong *et al.*[18] reported that acid functionalized CNTs start decomposing at 150 °C under air due to the presence of hydroxyl and carboxyl functional groups, while non-functionalized CNTs were thermally stable under air until 500 °C. This means that the presence of heteroatoms on the surface of carbon nanomaterials decreases their thermal stability. The FT-IR and XPS spectra showed that the Cdots and N-doped Cdots are rich in surface functional groups, therefore this functional groups are expected to decrease the thermal stability of the materials.

Figure 3.19a) and **b)** below shows the TG-DTG graph of Cdots-1 and Cdots-2, respectively. The peak at *ca* 102 °C with 3 % weight loss in the DTG of Cdots-2 corresponds to loss of absorbed moisture[18,36,37]. At *ca* 300 °C, there is a drastic loss of 39 wt% and 55 wt% weight for both Cdots-1 and Cdots-2, respectively. This may be attributed to the decomposition of surface functional grounds[36–38]. Cdots-1 and Cdots-2 are derived from a carbon source with oxygen based functional groups, therefore the weight loss maybe specifically due to hydroxyl and carboxyl based functional groups [36–39]. The presence of the hydroxyl and carbonyl functional groups was confirmed by the FT-IR spectra in **Figure 3.11a)**. The same may be true for the slight decrease in mass at *ca* 445 °C in the Cdots-1, although due to the high temperature, this might have been strongly bound functional groups. This peak might also be due from the formation of water at high temperature because of the reduction of oxygen molecules by hydrogen gas released by the sample[40]. The final peak at *ca* 597 °C (60 wt%) and 566 °C (38 wt%) for Cdots-1 and Cdots-2, respectively, corresponds to the weight loss due the oxidation of the non-functionalized carbon residue to CO and/or CO_2[18,38]. The results suggest that the Cdots-1 has a higher C: O ratio compared to Cdots-2.

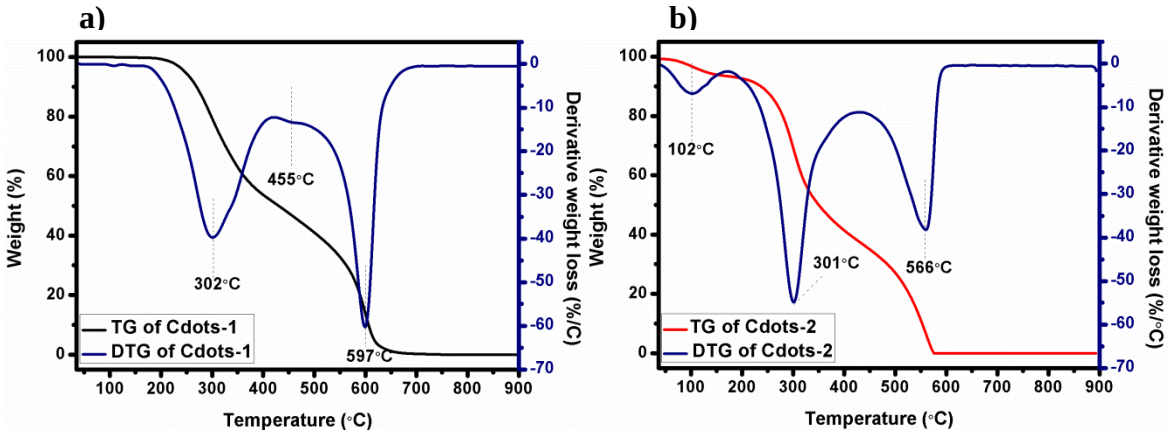


Figure 3.19: TG- DTG graphs of **a)** Cdots-1 and **b)** Cdots-2

Figure 3.20a) and **b)** below shows the TG-DTG graph of N-doped Cdots-1 and N-doped Cdots-2. It is to be noted that these two samples have more distinctive peaks compared to the Cdots in **Figure 3.19**. This could be due to the presence of nitrogen functional groups in addition to the oxygen functional groups confirmed by the FT-IR and XPS spectra, which further alters the surface chemistry of the Cdots. The weight loss peak at *ca* 89 °C and 161 °C which corresponds to the weight loss of 8 wt% and 7 wt% for N-doped Cdots-1 and N-doped Cdots-2, respectively, may be due to loss of moisture or highly volatile functional groups[33,34]. Between *ca* 200 to 432 °C, there is a weight loss of 59 wt% and 64 wt% for N-doped Cdots-1 and N-doped Cdots-2, respectively. This may be due to strongly bound surface functional groups[36–39]. Oxidation of carbon residue happens at *ca* 606 °C (33 wt%) and 627 °C (29 wt%) for N-doped Cdots-1 and N-doped Cdots-2, respectively. This suggests that the N-doped Cdots carbon core is more stable than the Cdots carbon core, however the amount of the non-functionalized carbon residue is very low (< 40 wt%).

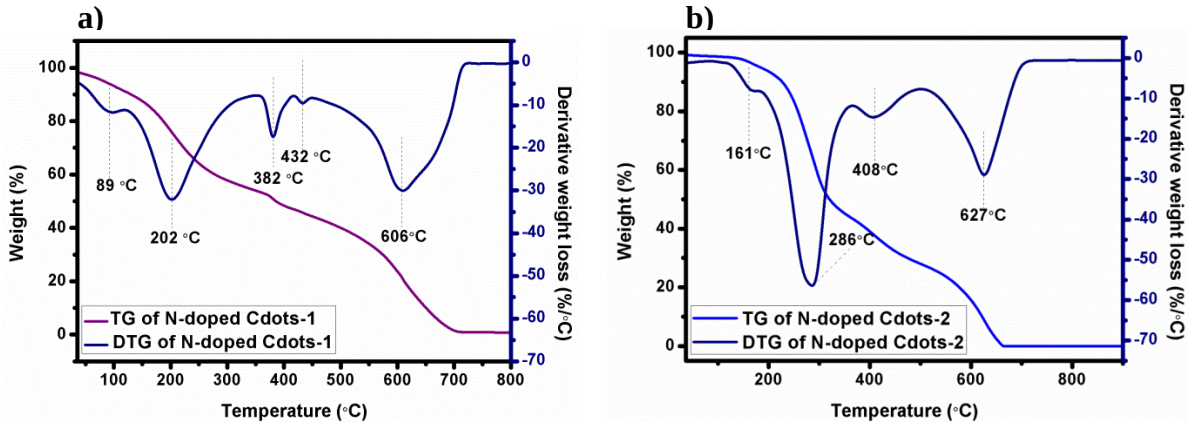


Figure 3.20: TG- DTG graphs of **a)** N-doped Cdots-1 and **b)** N-doped Cdots-2

3.4.5 Optical properties

As mentioned earlier in **CHAPTER 2**, the PL emission spectra of functionalized Cdots depends on their surface chemistry and structural morphology[9,14]. The actual mechanism for emission is still under investigation, however it has been noted that fluorescence result from emission selectivity by different sized Cdots and/or surface energy traps and as a result surface defects can be attributed to the functional groups[5,9,41]. The PL and UV-vis spectra of Cdots and N-doped Cdots are shown in **Figure 3.21a)** and **b)**, respectively. The spectra are drawn separately as the PL was measured on solid materials and the UV-vis spectra on solution samples.

3.4.5.1 Photoluminescent spectroscopy: PL

The PL spectra features broad peaks between 490-540 nm, corresponding to the blue to green emission in the visible light spectrum region[42]. Functional Cdots with PL emission in the blue to green spectra region have been used for chemical and biological sensing[12,43,44]; therefore these materials might also be suitable for application in chemical and biological sensing. The actual peak maximum positions are found in **Table 3.3**. The broadness of the peaks result from the inhomogeneous composition of Cdots and N-doped Cdots resulting from a variety of surface functional groups[45].The peak intensity of Cdots-2 is much higher when compared to the others. Peak intensity is affected by the amount of sample used. There is also a small shift in peak position as seen in **Table 3.3**. It has been reported that functionalized Cdots have excitation and/or particle size dependent PL properties[5,9,41]. However, this cannot be the reason for peak shift in this study since all measurements were taken at the same wavelength (244 nm). Roy *et al.*[46] reported PL spectrum shift from 450 nm to 486 nm (when excited at 300 nm) when Cdots sizes were increased from 5- 17 nm particle sizes. Therefore, the PL spectra shift of the Cdots-2 implies that their particle sizes are larger than the others.

3.4.5.2 Ultra-violet to visible absorption spectroscopy: UV-vis

The UV-vis spectra of Cdots and N-doped Cdots in **Figure 3.21b)** show absorption peaks between 280 and 300 nm which may be ascribed to $\pi \rightarrow \pi^*$ transition due to sp^2 aromatic domains[11,14,46]. For Cdots-1 and Cdots-2, there is a shoulder around 340 nm, which associated with the $n \rightarrow \pi^*$ transition of C=O bonds[47]. The significance of this shoulder in the Cdots sample might be due to their high wt% of oxygen. The actual absorption peak positions are recorded in **Table 3.3** below. The Inserted image in **Figure 3.21b)** shows the solution of Cdots-1 was colourless under ambient light and bluish-green when subjected to 365 nm UV light. This observation was the same for all four samples.

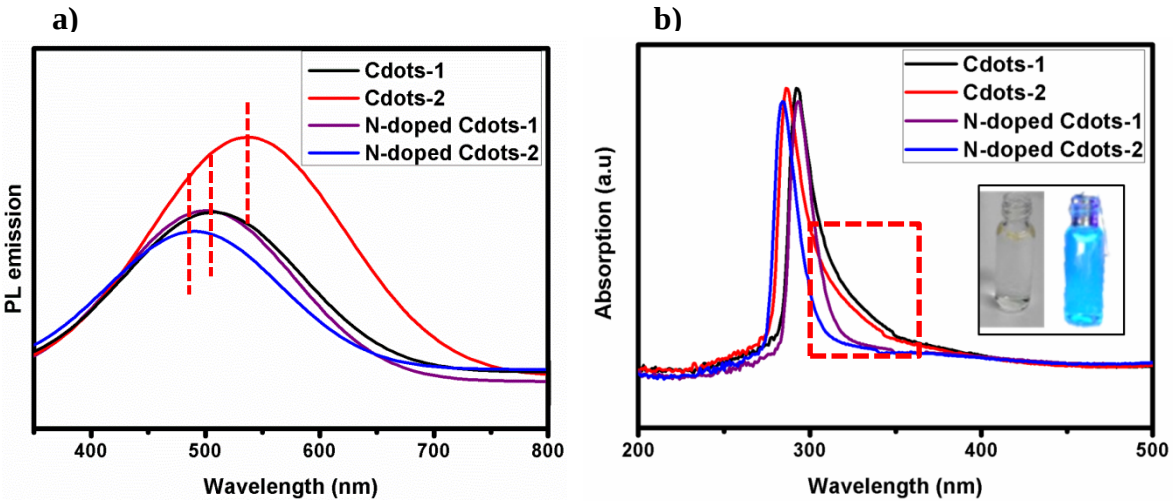


Figure 3.21: **a)** PL emission, the dotted lines represent the maximum intensity peak position, **b)** UV-vis absorption and inserted Cdots emission before and after 365 nm UV light irradiation

Table 3.3: PL and UV-vis peak positions

Sample	PL	UV (π→π*)	UV (n→π*)
Cdots-1	519	292	330
Cdots-2	537	286	330
N-doped Cdots-1	517	293	-
N-doped Cdots-1	491	284	-

3.5 Conclusion

Functionalized Cdots with different physicochemical properties were synthesized using the microwave-assisted reactions. The microwave assisted-reaction produced grams quantities of materials over a short reaction time. The XRD results showed that these functionalized Cdots are amorphous in nature. Raman spectroscopy results could not be interpreted due to the interference of Raman spectrometer light by the fluorescent Cdots. The FT-IR and XPS spectra proved that Cdots synthesized from ascorbic acid and sucrose contained hydroxyl and carbonyl functional groups. The FT-IR and XPS analysis results also proved that N-doped Cdots synthesized from chitosan, ascorbic acid and urea contained hydroxyl, carbonyl and nitrogen-based (mostly containing pyridinic and pyrrolic) functional groups. The TG-DTG thermograms showed that the functionalized Cdots decompose completely at 700 °C under

air. These functionalized Cdots are expected to keep the Co catalysts nanoparticles stable during *in-situ* X-ray diffraction reduction via MSIs.

References

1. Xu, X., Ray, R., Gu, Y., Ploehn, H. J., Gearheart, L., Raker, K. & Scrivens W. A. Electrophoretic Analysis and Purification of Fluorescent Single-Walled Carbon Nanotube Fragments. *J. Am. Chem. Soc*. **126**, 12736–12737 (2004).

2. Sun, Y. P., Zhou, B., Lin, Y., Wang, W., Fernando, K. A. S., Pathak, P., Meziani, M. J., Harruff, B. A., Wang, X., Wang, H., Luo, P. G., Yang, H., Kose, M. E., Chen, B., Veca, L. M., Xie, S. Y. Quantum-Sized Carbon Dots for Bright and Colorful Photoluminescence. *J. Am. Chem. Soc.* **128**, 7756–7757 (2006).

3. Zhang, J. & Yu, S. H. Carbon dots: large-scale synthesis, sensing and bioimaging. *Mater. Today* **19**, 382–393 (2016).

4. Tuerhong, M., Xu, Y. & Yin, X. B. Review on Carbon Dots and Their Applications. *Chin. J. Anal. Chem.* **45**, 139–150 (2017).

5. Lim, S. Y., Shen, W. & Gao, Z. Carbon quantum dots and their applications. *Chem. Soc. Rev.* **44**, 362–381 (2014).

6. Kappe, C. O. & Dallinger, D. Controlled microwave heating in modern organic synthesis: Highlights from the 2004-2008 literature. *Mol. Divers.* **13**, 71–193 (2009).

7. Li, H., Shao, F. Q., Zou, S. Y., Yang, Q. J., Huang, H., Feng, J. J. & Wang, A. J. Microwave-assisted synthesis of N , P-doped carbon dots for fluorescent cell imaging. *Microchimica Acta.* **183**, 821–826 (2016).

8. Liu, Y., Xiao, N., Gong, N., Wang, H., Shi, X., Gua, W. & Yea, L. One-step microwave-assisted polyol synthesis of green luminescent carbon dots as optical nanoprobes. *Carbon* **68**, 258–264 (2013).

9. Jelinek, R. *Carbon Quantum Dots*. 1–129 (Springer International Publishing Switzerland , 2017).

10. Gong, J., Lu, X. & An, X. Carbon dots as fluorescent off–on nanosensors for ascorbic acid detection. *RSC Adv.* **5**, 8533–8536 (2015).

11. Chen, B., Li, F., Li , S., Weng , W., Guo , H., Guo , T., Zhang , X., Chen , Y., Huang, T., Hong , X., You , S., Lin , Y., Zeng, K. & Chen, S. Large scale synthesis of photoluminescent carbon nanodots and their application for bioimaging. *Nanoscale* **5**, 1967–1971 (2013).

12. Sugiarti, S. & Darmawan, N. Synthesis of fluorescence carbon nanoparticles from ascorbic acid. *Indones. J. Chem.* **15**, 141–145 (2015).

13. Liu, X., Pang, J., Xu, F. & Zhang, X. Simple Approach to Synthesize Amino-Functionalized Carbon Dots by Carbonization of Chitosan. *Nat. Publ. Gr.* **2**, 1–8 (2016).

14. Xiao, D., Yuan, D., He, H. & Lu, J. Microwave-assisted one-step green synthesis of amino-functionalized fluorescent carbon nitride dots from chitosan. *Luminescence* **28**, 612–615 (2013).

15. Dlamini, M. W., Kumi, D. O., Phaahlamohlaka, T. N., Lyadov, A. S., Billing, D. G., Jewell, L. L. & Coville, N. J. Carbon Spheres Prepared by Hydrothermal Synthesis—A Support for Bimetallic Iron Cobalt Fischer–Tropsch Catalysts. *ChemCatChem* **7**, 3000–3011 (2015).

16. Guo, D. J., Wei, Z. Y., Shi, B., Wang, S. W., Wang, L. Z., Tanc, W. & Fang, S. M. Copper nanoparticles spaced 3D graphene films for binder-free lithium-storing electrodes. *J. Mater. Chem. A* **4**, 8466–8477 (2016).

17. Oh, Y. J., Yoo, J. J., Il Kim, Y., Yoon, J. K., Yoon, H. N., Kim, J. H. & Park, S. B. Oxygen functional groups and electrochemical capacitive behavior of incompletely reduced graphene oxides as a thin-film electrode of supercapacitor. *Electrochim. Acta* **116**, 118–128 (2014).

18. Xiong, H., Motchelaho, M. A. M., Moyo, M., Jewell, L. L. & Coville, N. J. Correlating the preparation and performance of cobalt catalysts supported on carbon nanotubes and carbon spheres in the Fischer-Tropsch synthesis. *J. Catal.* **278**, 26–40 (2011).

19. Xiong, H., Moyo, M., Rayner, M. K., Jewell, L. L., Billing, D. G. & Coville, N. J. Autoreduction and Catalytic Performance of a Cobalt Fischer-Tropsch Synthesis Catalyst Supported on Nitrogen-Doped Carbon Spheres. *ChemCatChem* **2**, 514–518 (2010).

20. Dlamini, M. W. Spherical carbons as model supports for Fe , Co and Fe-Co Fischer-Tropsch catalysts. PhD Thesis (University of the Witwatersrand, Johannesburg, 2016).

21. Peng, S., Fan, X., Li, S. & Zhang, J. Green synthesis and characterization of graphite oxide by orthogonal experiment. *J. Chil. Chem. Soc.* **58,** 2213–2217 (2013).

22. Mohapatra, S., Sahu, S., Sinha, N. & Bhutia, S. K. Synthesis of a carbon-dot-based photoluminescent probe for selective and ultrasensitive detection of Hg^{2+} in water and living cells. *Analyst* **140**, 1221–1228 (2015).

23. Gong, X., Lu, W., Paau, M. C., Hu, Q., Wu, X., Shuang, S., Dong, C., Choi, M. M. F. Facile synthesis of nitrogen-doped carbon dots for Fe^{3+} sensing and cellular imaging. *Anal. Chim. Acta* **861**, 74–84 (2015).

24. Li, H., Kang, Z., Liu, Y. & Lee, S. T. Carbon nanodots: synthesis, properties and applications. *J. Mater. Chem.* **22**, 24230 (2012).

25. Qu, D. Zheng, M., Zhang, L., Zhao, H., Xie, Z., Jing, X., Haddad, R. E., Fan, H. & Sun, Z. Formation mechanism and optimization of highly luminescent N-doped graphene quantum dots. *Sci. Rep.* **4**, 1–11 (2014).

26. Mutuma, B. K. Synthesis and characterization of solid, hollow, core-shell and worm-like carbon nanostructures for applications in organic photovoltaic devices and chemical sensors. PhD Thesis (University of the Witwatersrand, Johannesburg, 2016).

27. Li, X. G., Lv, Y., Ma, B. G., Wang, W. Q. & Jian, S. W. Decomposition kinetic characteristics of calcium carbonate containing organic acids by TGA. *Arab. J. Chem.* **10**, S2534–S2538 (2017).

28. Wepasnick, K. A., Smith, B. A., Bitter, J. L. & Fairbrother, D. H. Chemical and structural characterization of carbon nanotube surfaces. *Anal. Bioanal. Chem.* **396**, 1003–1014 (2010).

29. Ma, J., Ping, D. & Dong, X. Recent developments of graphene oxide-based membranes: A review. *Membranes (Basel).* **7**, 1–29 (2017).

30. Xiong, H., Moyo, M., Motchelaho, M. A., Tetana, Z. N., Dube, S. M. A., Jewell, L. L. & Coville, N. J. Fischer-Tropsch synthesis: Iron catalysts supported on N-doped carbon spheres prepared by chemical vapor deposition and hydrothermal approaches. *J. Catal.* **311**, 80–87 (2014).

31. Zhang, C., Hao, R., Liao, H. & Hou, Y. Synthesis of amino-functionalized graphene as metal-free catalyst and exploration of the roles of various nitrogen states in oxygen reduction reaction. *Nano Energy* **2**, 88–97 (2013).

32. Kumar, K. S., Pittala, S., Sanyadanam, S. & Paik, P. A new single/few-layered graphene oxide with a high dielectric constant of 10^6: contribution of defects and functional groups. *RSC Adv.* **5**, 14768–14779 (2015).

33. Bandi, R., Gangapuram, B. R., Dadigala, R., Eslavath, R., Singh, S. S. & Guttena, V. Facile and green synthesis of fluorescent carbon dots from onion waste and their potential applications as sensor and multicolour imaging agents. *RSC Adv.* **6**, 28633–28639 (2016).

34. Mewada, A., Pandey, S., Shinde, S., Mishra, N., Oza, G., Thakur, M., Sharon, M. & Sharon, M. Green synthesis of biocompatible carbon dots using aqueous extract of Trapa bispinosa peel. *Mater. Sci. Eng. C* **33**, 2914–2917 (2013).

35. Gao, R., Hu, N., Yang, Z., Zhu, Q., Chai, J., Su, Y., Zhang, L & Zhang Y. Paper-like graphene-Ag composite films with enhanced mechanical and electrical properties. *Nanoscale Res. Lett.* **8**, 2–9 (2013).

36. Sachdev, A. & Gopinath, P. Green synthesis of multifunctional carbon dots from coriander leaves and their potential application as antioxidants, sensors and bioimaging agents. *Analyst* **140**, 4260–4269 (2015).

37. Mehta, V. N., Jha, S. & Singhal, K. Preparation of multicolor emitting carbon dots for HeLa cell imaging. *New J. Chem.* **38**, 6152–6160 (2014).

38. Moyo, M. Cobalt and Iron Supported on Carbon Spheres Catalysts for Fischer. PhD Thesis (University of the Witwatersrand, Johannesburg, 2012).

39. Motchelaho, M. A. M., Xiong, H., Moyo, M., Jewell, L. L. & Coville, N. J. Effect of acid treatment on the surface of multiwalled carbon nanotubes prepared from Fe-Co supported on $CaCO_3$: Correlation with Fischer-Tropsch catalyst activity. *J. Mol. Catal. A Chem.* **335**, 189–198 (2011).

40. Arenillas, A., Rubiera, F. & Pis, J. J. Simultaneous thermogravimetric-mass spectrometric study on the pyrolysis behaviour of different rank coals. *J. Anal. Appl. Pyrolysis* **50**, 31–46 (1999).

41. Li, X. Wang, H. ,Shimizu, Y., Pyatenko, A., Kawaguchi, K. & Koshizaki, N., Preparation of carbon quantum dots with tunable photoluminescence by rapid laser passivation in ordinary organic solvents. *Chem. Commun***. 47**, 932–934 (2011).

42. Wen, Z. H. & Yin, B. X. Excitation-independent carbon dots, from photoluminescence mechanism to single-color application. *RSC Adv.* **6**, 27829–27835 (2016).

43. Liu, H., Zhang, L., Yan, M. & Yu, J. Carbon nanostructures in biology and medicine. *J. Mater. Chem. B* **5**, 6437–6450 (2017).

44. Demchenko, A. P. & Dekaliuk, M. O. Novel fluorescent carbonic nanomaterials for sensing and imaging. *METHODS Appl. Fluoresc.* **1**, 1–17 (2013).

45. Zhu, S., Song, Y., Zhao, X., Shao, J., Zhang, J. & Yang, B. The photoluminescence mechanism in carbon dots (graphene quantum dots , carbon nanodots and polymer dots): current state and future perspective. *Nano. Res.* **8**, 355–381 (2014).

46. Roy, P., Chen, P., Periasamy, A. P., Chen, Y. & Chang, H. Photoluminescent carbon nanodots : synthesis , physicochemical properties and analytical applications. *Mater. Today* **18**, 447–458 (2015).

47. Peng, Z., Han. X., Li, S., Al-Youbi, A. O., Bashammakh, A. S., El-Shahawi, M. S. & Leblanc, R. M. Carbon dots : Biomacromolecule interaction, bioimaging and nanomedicine. *Coord. Chem. Rev.* **343**, 256–277 (2017).

CHAPTER 4: SYNTHESIS AND CHARACTERIZATION OF SPINEL Cobalt (II,III) oxide (Co_3O_4) NANOPARTICLES

4.1 Introduction

Co-based catalysts are the most widely used catalysts in Fischer-Tropsch (F-T) process. This is due to their favourable attributes such as high activity and selectively towards long-chain hydrocarbons, low selectivity to water to gas shift (WGS) compared to Fe, and low cost compared to Ru[1–3]. A lot of research has been done on understanding the size-activity relationship as well as the support-activity relationship of Co-based catalysts. It has been observed that Co nanoparticles < 8 nm are more selective towards methane and easily deactivate during synthesis due to the oxidation of F-T active Co catalyst[4,5]. It has also been reported that the activity of the catalyst depends on the metal to support interactions (MSIs)[6–8].

The aim of this chapter is to report on the synthesis and characterization spinel Co_3O_4 nanoparticles. Spinel Co_3O_4 nanoparticles with 10 nm average crystallite size were synthesized using the "benzyl alcohol route"[9,10]. The effect of adding water to the reaction mixture on the size of nanoparticles formed will be discussed.

4.2.1 Synthesis of spinel Co_3O_4 from the ammonia assisted "benzyl alcohol route"

Spinel Co_3O_4 is one of the many metal nanoparticles with size and shape dependent properties[11–13]. Different sizes and shapes of this metal oxide nanoparticles have been used in areas such as catalysis, electrochemistry, energy storage and sensing[11–18]. Spinel Co_3O_4 have been synthesized using methods such as sol-gel[15,16], reverse micelle[17,18], the "benzyl alcohol route"[9,19–21], thermal decomposition[22,23], *etc*. Although there are a variety of ways to synthesize these metal nanoparticles, solution methods such as the sol-gel, reverse micelle and the "benzyl alcohol route" are usually preferred for large scale synthesis of spinel Co_3O_4 crystillites[9,20,21]. Other methods suffer from drawbacks such as expensive reaction setups, long reaction times, difficulty in controlling the shape and size of nanoparticles, and very low yields of products[9,20,21].

Solution methods, such as the sol-gel method, reverse micelle and the "benzyl alcohol" route have been used for synthesis of various metal nanoparticles with different sizes and shapes. However, the sol-gel method and the reverse micelle method suffer from many drawbacks compared to the "benzyl alcohol route". The metal particle sizes are not easily controlled using the sol-gel method due to the high reactivity of the metal precursor in solution, and the

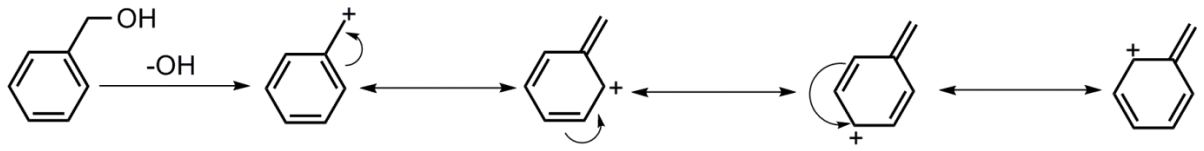
products obtained are usually very small (< 5 nm) crystallites[9,21]. In the reverse micelle approach, a large amount of expensive (and toxic) surfactant is used to produce a very small amount of nanoparticles[9].

Unlike the sol-gel and reverse micelle method, the "benzyl alcohol route" has been reported as a facile, effective and cheap route for the synthesis of metal nanoparticles[9,10]. Furthermore, the "benzyl alcohol route" is more effective in the synthesis of nanoparticles with high crystallinity and less agglomeration, and the alcohol helps control the crystal growth and shape of the resulting nanoparticles[9,10,14]. This is because benzyl alcohol acts as a solvent, a ligand and a capping agent during the reaction[10].

The "benzyl alcohol route" is typically a one pot synthesis reaction where a metal precursor is transformed into a metal oxide in the presence of benzyl alcohol and sometimes an amine solution, at temperatures below the boiling point of benzyl alcohol[10,14]. This method has been used for the synthesis of other metal oxides such as iron oxide, gadolinium oxide and zinc oxide as well as barium titanate and lanthanide doped yttrium oxides[9,20,21]. This method has shown great potential for the synthesis of metal oxide nanoparticles with size- and shape-dependent physical properties.

4.2.1.1 Benzyl alcohol chemistry

Benzyl alcohol consists of a benzene ring and an α-carbon attached to a hydroxyl group. Hydroxyl group elimination leads to the formation of a very stable benzylic carbocation (**Scheme 4.1** below)[10]. The carbocation is resonance stabilized, making the hydroxyl a good leaving group compared to a hydroxyl group in saturated and/or aliphatic alcohols[10]. A metal precursor, which is a complex itself, will undergo ligand substitution (see **eq. 4.1.1**) in the presence of benzyl alcohol. The benzyl alcohol molecules attach themselves to the metal precursor via the hydroxyl group, forming a metal-ligand bond[10,21]. The benzylic carbocation formed then easily reacts with substituted ligands that were attracted to the metal, for e.g., benzyl chloride forms when chlorine ions were ligands in the metal precursor, benzoate when acetate ions were ligands, *etc.* (**e.q 4.1.3**)[10,21]. The hydroxide group on the metal can then be further oxidized to form the desired metal oxide[10,19]. Benzyl alcohol is also fundamental for directing the growth and morphology of the final nanoparticles[9].



Scheme 4.1: Benzyl alcohol and the four resonance structures of benzylic carbocation.

$$[\mathrm{M(X)}_x] + \mathrm{C_7H_8\,O} \rightarrow \mathrm{M(OH)}_x + \mathrm{C_7H_7X} \quad \textbf{e.q 4.1.1}$$

$$[\mathrm{M(X)}_x] + \mathrm{C_7H_8\,O} + \mathrm{ammonia} \rightarrow \mathrm{M(ammonia)}_x + X^- + \mathrm{C_7H_8\,O} \quad \textbf{e.q 4.1.2}$$

$$\mathrm{M(ammonia)}_x + \mathrm{C_7H_8\,O} + \mathrm{heat} \rightarrow \mathrm{M(OH)}_x + \mathrm{C_7H_7X} \quad \textbf{e.q 4.1.3}$$

M=high valent metal, Ti^{4+}, Fe^{3+},

M=low valent metal, Co^{2+}, Zn^{2+},

X=acetate$^-$, Cl^-, NO_3^-, *x*= no. of ligands

As mentioned above, benzyl alcohol also plays a role as a capping agent. In cases where metal acetate is used as metal precursors, the acetate groups and the benzyl group are attached to the catalytically active site of the premade metal oxides[9,10,14]. The metal oxide then facilitates (catalyse) the nucleophilic reaction between the acetate and the benzylic carbocation to form an ester[9]. The catalytically active side of the metal is useful for metal oxide particle growth. Termination of metal oxide nanoparticle growth happens when the catalytically active surface site of the metal is saturated with the acetate and benzyl groups, and also the formed esters[9,10]. The metal oxide is only active at particular sites. Therefore, the shape of the nanoparticle is also controlled by these active catalytic sites[9]. A more detailed explanation of the mechanism for the formation of metal oxides via the "benzyl alcohol route" have been well explained by Pinna[9,20,21], and Hu *et al.*[10].

The synthesis of Co_3O_4 from a Co(II)-complex precursor, like the synthesis of other low valent oxides (II,I) via this route, requires the presence of a base, usually an amine[10,11,14,19]. Low valent metals have a very poor ability to remove the hydroxyl group from benzyl alcohol[10]. The amine solvent is usually added before heating the reaction. The amine solvent will then substitute the ligands on the metal precursors, and when the reaction mixture is heated, the amine ligand will undergo desorption and open sites for the hydroxyl group to allow the benzyl alcohol to attach to the metal centre (**eq. 4.1.2** and **4.1.3**)[10,11]. Amines such as ammonia solution[11,14,19] and dodecylamine[10] have been used in the synthesis of spinel

Co_3O_4 from low valent Co(II)-metal precursor. Other alcohols such as ethanol[11,12] and 1-hexanol[12] have been used for the synthesis of spinal Co_3O_4 nanoparticles.

The aim of this study was to synthesize spinel Co_3O_4 nanoparticles with average crystallite sizes of > 10 nm by modifying the "benzyl alcohol route" reported by Shi *et al.*[14] and Wolf *et al.*[19]. The Co_3O_4 particle sizes must be larger than the Cdots particle sizes (< 6 nm) to afford inverse Co_3O_4/ Cdots supported catalyst. In their synthesis, Shi *et al.*[14] used 160 mg $Co(OAc)_2$, 7 mL BA and 7 mL NH_4OH to produce spinel Co_3O_4 with particle sizes of 4.5 nm. Following a similar procedure but using a rotary evaporator instead of a traditional oil bath heating method, Wolf *et al.*[19] varied this amount $Co(OAc)_2$, BA and NH_4OH to obtain particle with average crystallite sizes of between 3 and 7 nm.

It has been reported that the polarity of the solvent used in the synthesis of metal nanoparticles can affect their overall size. Solvents with lower polarity bind to the nucleation site of the metal nanoparticles and hence terminates growth quicker[9,10,20,21]. However, adding another solvent with higher polarity, like water, can increase the polarity of the system and therefore delay termination of metal particle growth and hence result in the synthesis of metal particles with larger size[11].

Dong *et al.*[11] used ethanol (EtOH) as a solvent in the synthesis of Co_3O_4 nanoparticles with average sizes of 3.5, 6, 11 and 70 nm, at 150 °C. In the study, they used $Co(OAc)_2$, EtOH/H_2O and NH_4OH for the synthesis of Co_3O_4 nanoparticles by an autoclave method. They were able to study the effect of solvent/s polarity on the cobalt particle sizes. Furthermore, they were also able to show that adjusting the polarity of solution by adding H_2O led to the generation of larger Co_3O_4 nanoparticles. The as prepared Co_3O_4 nanoparticle size increased from 3.5 nm when only EtOH was used as a solvent, to 11 nm at 3/2 EtOH/H_2O ratio, and finally 70 nm when only H_2O was used as a solvent[11]. However the nanoparticles obtained had irregular shapes and poor dispersion[11].

In this study, using the "benzyl alcohol route"[14,19] instead of EtOH, the polarity of the reaction system was varied by adding H_2O in the system to synthesize Co_3O_4 nanoparticles average crystallite sizes > 10 nm.

4.2.2 Experimental procedures

4.2.2.1 The rotary evaporator method

The following procedure carried out at the Chemical Engineering Laboratories at the University of Cape Town with assistance from Mr Moritz Wolf. In a typical procedure, 3.2 g of $Co(OAc)_2{\cdot}4H_2O$ was dissolved in 140 mL BA inside a 600 mL flat bottom flask under vigorous stirring. After 2 hrs, 140 mL NH_4OH (25 %) was added dropwise (through a separating funnel) to form a brown emulsion. Distilled H_2O (140 mL) was subsequently added to the mixture through the same separating funnel. The flat bottom flask was then placed in a preheated oil bath at 165 °C on a rotary evaporator. The mixture was allowed to react for 3 hrs. The pump pressure was set at 900 mbar and the flat bottom flask was rotated at 180 rpm, while air was being bubbled into the bottom of the flask for complete mixing. After 3 hrs, the resulting black solution was then allowed to cool to room temperature. After cooling, diethyl ether was added to the mixture and the nanoparticles were obtained after centrifugation at 15000 rpm for 15 min, and washed several times with ethanol and then re-dispersed in a mixture of ethanol and acetone (3:1 ratio), and allowed to dry in a fume hood for three days. The nanoparticles were obtained as Co_3O_4 without calcination.

4.2.2.2 The hotplate method

The method followed in this section was adopted (with modification) from Shi *et al.*[14]. The quantity of $Co(OAc)_2{\cdot}4H_2O$, BA and NH_4OH (25 %) was the same as above. The amount of water was varied by 70, 105 and 140 mL, to investigate the effect of water on the Co_3O_4 crystallite sizes. The experimental set-up is shown in **Figure 4.1** below. 3.2 g of $Co(OAc)_2{\cdot}4H_2O$ in a 600 mL beaker was dissolved in 140 mL BA for 2 hrs, as stated above. To the solution mixture distilled water (70, 105 and 140 mL) was added. The mixture was then transferred into a 1 L flat bottom flask equipped with a magnetic stirrer bar (8×30 mm) and placed inside an oil bath (165 °C) on a magnetic stirrer with a hotplate and a thermocouple to measure the temperature of the oil bath. The mixture was also allowed to react for 3 hrs. Air was pumped into the system as shown in **Figure 4.1**. The Co_3O_4 crystallites were purified as before, and were also obtained as Co_3O_4 without calcination.

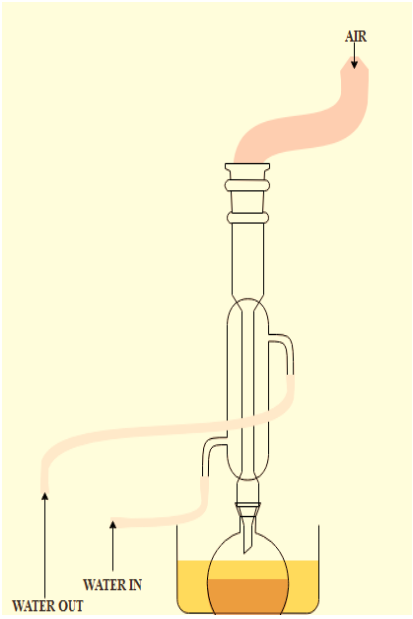


Figure 4.1: Experimental set-up for Co_3O_4 nanoparticles synthesis using a hotplate

4.2.3 Characterization

The synthesized crystalline Co_3O_4 nanoparticles were characterized using XRD, TEM and FT-IR as described in **section 3.3.1**, **3.3.2** and **3.3.5**. Both TEM results and Rietveld refinement in TOPAS5 were used to estimate the particle sizes and crystallite sizes, respectively. The % yield were obtained following **eq. 3.1** in **CHAPTER 3**. The Co_3O_4 nanoparticles were also characterized using Temperature Programmed Reduction.

4.2.3.1 Temperature Programmed Reduction: TPR

TPR was used to determine the reduction temperature of Co_3O_4 to metallic Co under hydrogen (H_2) gas. The reduction temperatures were measured and recorded using a Micromeritics AutoChem II instrument. 100 mg of Co_3O_4 nanoparticles were first degassed at 150 °C for 30 min under helium gas at 50 ml/min. Thereafter, the sample was subjected to temperatures between 50 and 800 °C at 10 °C/min, using 5% hydrogen (balanced with Argon gas) at a flow rate of 50 mL/min as an analysis.

4.2.4 Results and Discussions

Table 4.1 below summarizes the results obtained from each synthesis including the procedure followed in **section 4.2.2.2**.

Table 4.1: Summarized synthesis results of Co_3O_4 nanoparticles with different crystallite sizes

Sample	Distilled water (mL)	Estimated crystallite sizes (nm)	% yields
1*	140	10.2 ± 0.1	35
2#	70	16.6 ± 0.3	19
3#	105	19.2 ± 0.2	26
4#	140	21.2 ± 0.2	22

**Synthesized from the rotary evaporator method, #synthesized from the hotplate method.*

4.2.4.1 Synthesis results

The following observations were made during the preparation of Co_3O_4:

In the first step of the synthesis, after adding NH_4OH, the reaction mixture slowly turned from a bright pink solution to a brown emulsion, symbolizing the formation of $[Co(NH_3)_6)]^{2+}$ [11]. No colour change was observed after adding distilled water, meaning that there was no $[Co(OH)_6)]^{2+}$ complex formed, or if there was, it might have been quickly transformed to $[Co(NH_3)_6)]^{2+}$ complex again. A few minutes after the reaction in the flask mixture was added in the hot oil bath, the colour changed from brown to a deep red-brown colour, symbolizing the oxidation of some of the Co(II) to Co(III)[11]. It is noted that at high temperature, NH_4OH ligands were readily displaced by the hydroxyl groups on the cobalt metal, which subsequently was oxidised by air to a form black solution[10,14]. The solution at the end of the reaction was black, therefore symbolizing the formation of Co_3O_4. The solution also had a sweet smell, consistent with the formation of an ester (benzoate) as a by-product[9]. However the purified products did not have any smell. These observations were made during the synthesis of all the samples.

Table 4.1 showed that the rotary evaporator method gave the highest product yield. This could be due to sufficient mixing of precursors during synthesis which was aided by the rotary evaporator, and bubbling air directly into the reaction mixture. In the hotplate method, a magnetic stirrer was used for mixing, which might have not been enough to allow most of

the Co_3O_4 precursor to be converted to product. The air bubbler was also placed in a position that prevented it to be effective in both mixing and providing air into the reaction mixture.

4.2.4.2 Physical properties: XRD

XRD was used to determine the phase composition of the as prepared Co_3O_4 nanoparticles. **Figure 4.2** below shows the indexed XRD patterns of all four samples with peaks at 2θ = 22 °, 36 °, 43 °,45 °, 52 °, 66 °, 70 ° and 77 ° corresponding to the (111), (220), (311), (222), (400), (422), (511) and (440) planes of Co_3O_4[14,24]. These results also shows that the samples contain purely spinal Co_3O_4, which confirms that $[Co(OH)_6)]^{2+,3+}$ was successfully oxidised to Co_3O_4 without any post-oxidation by calcination. The fact that the samples synthesized by the hotplate method gave the same results even when air was not correctly bubbled into the reaction mixture means that there was enough air (or oxygen) in the system to assist in the oxidation of $[Co(OH)_6)]^{2+,3+}$ to Co_3O_4.

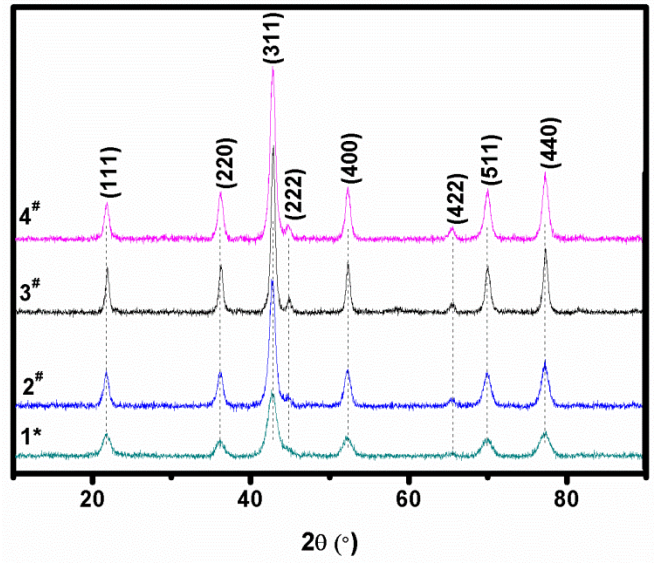


Figure 4.2: XRD patterns of spinel Co_3O_4 nanoparticles highlighting the peak positions of the Co_3O_4 phase

For synthesis 1* and $4^{\#}$ in **Table 4.1**, the same ratio of starting material was used, however the crystallite size of the nanoparticles were different. This could be attributed to loss of water in the reaction mixture during synthesis 1*. During the synthesis of Co_3O_4 nanoparticles by the rotary evaporator, NH_4OH and water were evaporated from the reaction mixture at 165 °C, and collected into collection bottle. This then decreases the polarity of the reaction mixture again and resulted in the formation of smaller nanoparticles (as described in **section 4.2.2.1** above).

4.2.4.3 Physical properties: TEM

The morphology and size of the Co_3O_4 nanoparticles were determined by TEM, as shown in **Figure 4.3**. From the TEM images, it can be observed that the nanoparticles are cubic in shape, and this agrees with the shape obtained by and Shi *et al.*[14] and Wolf *et al.*[19]. However, the particles are not as well dispersed. The particle sizes from synthesis 1*, $2^{\#}$, $3^{\#}$ and $4^{\#}$ were 9.7±2.5 nm, 15.7±2.7 nm, 17.4±4.8 nm, and 19.9±3.3 nm, respectively. This also confirmed that the particle sizes Co_3O_4 nanocubes increase with increase in the amount of water added. The particle sizes determined by TEM and the crystallite sizes determined by Rietveld refinement were also found to be comparable.

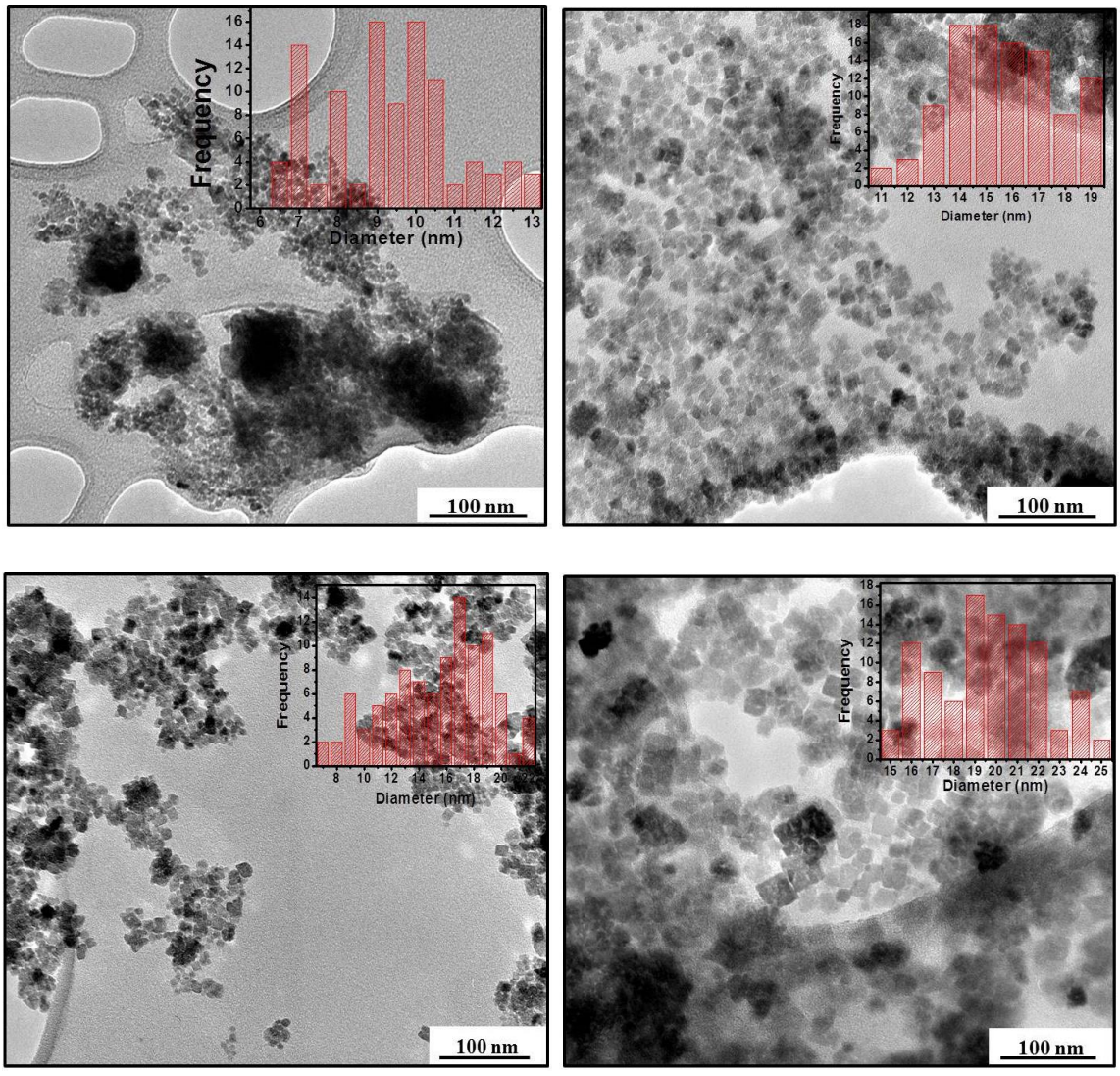


Figure 4.3: TEM image with an inserted particle size distribution histogram of Co_3O_4 nanocubes synthesized by method a) 1*, b) $2^{\#}$, c) $3^{\#}$ and d) $4^{\#}$.

4.2.4.4 Chemical properties

FT-IR spectrum of the prepared spinel Co_3O_4 nanoparticles is shown in **Figure 4.4** below. The spectrum was compared with the FT-IR spectra of cobalt acetate and benzyl alcohol. A weak band at 3718 cm^{-1} was assigned to an O-H stretch. This could be attributed to water molecules that could be adsorbed on the surface of the nanoparticles. The weak bands at 3037 and 2878 cm^{-1} can be attributed to the C-H stretching mode, the bands between 1560 and1433 cm^{-1} could be due to the C-O-O^- stretches and a weak band at 1006 cm^{-1} could be due to the C- O^- stretch. These bands corresponds to some of the bands mostly in cobalt acetate and some from benzyl alcohol, which helps redisperse the nanoparticles in water[14,21]. However, band intensities are very low compared to those observed in the starting material, which implies that most of the acetate ion and benzyl alcohol were washed out during purification. The last two peaks at 567 and 662 cm^{-1} belong to the Co-O bonds stretch, belonging to the crystalline Co_3O_4 [14,25]. The obtained FT-IR spectra were very similar to the one obtained by Shi *et al.*[14], who also noted the two Co-O stretches at 665 and 577 cm^{-1}. Shi *et al.* observed only the bands corresponding to acetate ions in the FT-IR spectra of Co_3O_4, and no other bands which corresponds to the either benzyl alcohol or benzoate[14]. The same FT-IR spectrum was observed for the Co_3O_4 nanoparticles obtained from the hotplate method.

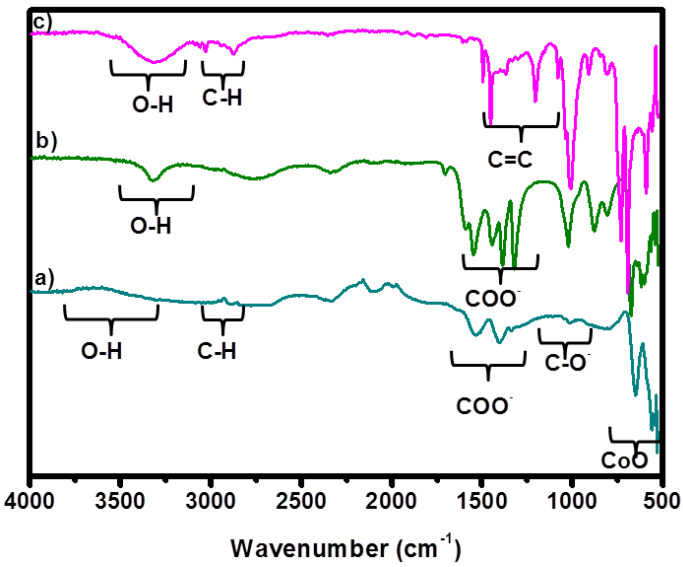


Figure 4.4: FT-IR spectra of **a)** spinel Co_3O_4 nanoparticles at **b)** Cobalt acetate **c)** benzyl alcohol

4.2.4.5 Thermal reduction studies

TPR profile of Co_3O_4 nanoparticles, synthesized using the rotary evaporator method, is shown in **Figure 4.5** below.

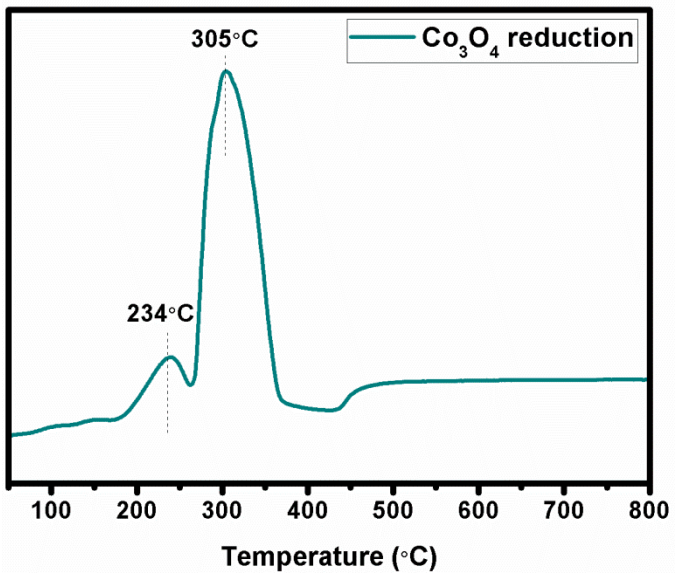


Figure 4.5: TPR profile of crystalline Co_3O_4 nanoparticles

The reduction profiles show two peaks at *ca* 234 and 305 °C, corresponding to the reduction of Co_3O_4 to CoO and to metallic Co, respectively[26]. The reduction equations are represented in **eq.4.1** and **4.2** below. The ratio of hydrogen consumed in the two reactions is 1:3, hence the second peak is more intense than the first one[27]. The peaks are however not well separated. This could imply that there is an overlap in the temperatures at which the two reduction steps represented by **eq. 4.1** and **4.2** occur. Since TPR gives quantitative information, the crystallographic phases (hcp and/or fcc phase) of metallic Co could not be determined.

$Co_3O_4 + H_2 \rightarrow 3CoO + H_2O$ ……..**eq. 4.1**

$CoO + 3H_2 \rightarrow 3Co + 3H_2O$……..**eq. 4.2**

4.3 Conclusion

The benzyl alcohol route was successfully used for the synthesis of spinel Co_3O_4 nanoparticles. XRD and Rietveld refinement were used to estimate the crystallite sizes of the obtained nanoparticles. TEM and Rietveld refinement results confirmed an increase in the

nanocrystallite sizes with increase in volume of distilled water. This could be attributed to an increase in polarity of the reaction mixture, which helps reduce the benzyl alcohol molecules that inhibit nanoparticle growth. FT-IR also confirms the presence of Co-O bands attributed to the Co_3O_4. It also shows that the surface of the crystalline Co_3O_4 nanoparticles has some organic functional groups and water molecules attached to them, which will help in dispersing them in water. The TPR profile of Co_3O_4 nanoparticles shows two joint reduction peaks, which suggests that most of Co_3O_4 is quickly reduced from CoO to Co.

References

1. Tauster, S. J., Fung, S. C., Baker, R. T. K. & Horsley, J. A. Strong Interactions in Supported-Metal Catalysts. *Science* **211**, 1121–1125 (1981).

2. Motchelaho, M. A. M., Xiong, H., Moyo, M., Jewell, L. L. & Coville, N. J. Effect of acid treatment on the surface of multiwalled carbon nanotubes prepared from Fe-Co supported on $CaCO_3$: Correlation with Fischer-Tropsch catalyst activity. *J. Mol. Catal. A Chem.* **335**, 189–198 (2011).

3. Moyo, M., Motchelaho, M. A. M., Xiong, H., Jewell, L. L. & Coville, N. J. Promotion of Co/carbon sphere Fischer-Tropsch catalysts by residual K and Mn from carbon oxidation by $KMnO_4$. *Appl. Catal. A Gen.* **413–414**, 223–229 (2012).

4. Yang, J., Frøseth, V., Chen, D. & Holmen, A. Particle size effect for cobalt Fischer – Tropsch catalysts based on in situ CO chemisorption. *Surf. Sci.* **648**, 67–73 (2016).

5. Iglesia, E. Design, synthesis, and use of cobalt-based Fischer-Tropsch synthesis catalysts. *Appl. Catal. A Gen.* **161,** 59–78 (1997).

6. van Heerden, T. & van Steen, E. Metal – support interaction on cobalt based FT catalysts – a DFT study of model inverse catalysts. *Faraday Discuss.* **197**, 87–99 (2017).

7. Macheli, L. Co_3O_4 -Nanocubes modified with TEOS as models to study support interactions in cobalt-based Fischer-Tropsch catalysts. MSc Dissertation (University of Cape Town, Cape Town, 2014).

8. Xiong, H., Jewell, L. L. & Coville, N. J. Shaped Carbons As Supports for the Catalytic Conversion of Syngas to Clean Fuels. *ACS Catal.* **5**, 2640–2658 (2015).

9. Pinna, N. The 'benzyl alcohol route': an elegant approach towards organic–inorganic hybrid nanomaterials. *J. Mater. Chem.* **17**, 2769–2774 (2007).

10. Hu, M., Xu, J., Gao, J., Yang, S., Wong, J.S.P. & Li, R.K.Y. Benzyl alcohol-based synthesis of oxide nanoparticles: the perspective of S_N1 reaction mechanism. *Dalt. Trans.* **42**, 9777–9784 (2013).

11. Dong, Y., He, K., Yin, L. & Zhang, A. A facile route to controlled synthesis of Co_3O_4 nanoparticles and their environmental catalytic properties. *Nanotechnology* **18**, 1–6 (2007).

12. Zhao, Z. W., Guo, Z. P. & Liu, H. K. Non-aqueous synthesis of crystalline Co_3O_4 powders using alcohol and cobalt chloride as a versatile reaction system for controllable morphology. *J. Power Sources* **147**, 264–268 (2005).

13. Gunnewiek, R. F. K., Mendes, C. F. & Kiminami, R. H. G. A. Synthesis of spinel cobalt oxide nanoparticles using a modified polymeric precursor method. *Adv. Powder Technol.* **27**, 1056–1061 (2016).

14. Shi, N., Cheng, W., Zhou, H., Fan, T. & Niederberger, M. Facile synthesis of monodisperse Co_3O_4 quantum dots with efficient oxygen evolution activity. *Chem. Commun.* **51**, 1338–1340 (2015).

15. Lakshmi, B. B., Patrissi, C. J. & Martin, C. R. Sol-Gel Template Synthesis of Semiconductor Oxide Micro- and Nanostructures. *Chem. Mater.* **9**, 2544–2550 (1997).

16. El Baydi, M., Poillerat, G., Rehspringer, J., Gautier, J. L., Koening, J.,Chartier, P. J. A Sol-Gel Route for the Preparation of Co_3O_4 Catalyst for Oxygen Electrocatalysis in Alkaline Medium. *J. Solid State Chem.* **109**, 281–288 (1994).

17. Prieto, G., Martínez, A., Concepción, P. & Moreno-Tost, R. Cobalt particle size effects in Fischer-Tropsch synthesis: structural and in situ spectroscopic characterisation on reverse micelle-synthesised Co/ITQ-2 model catalysts. *J. Catal.* **266**, 129–144 (2009).

18. Vidal-Abarca, C., Lavela, P. & Tirado, J. L. Cobalt Oxide Nanoparticles Prepared from Reverse Micelles as High-Capacity Electrode Materials for Li-Ion Cells. *Electrochem. Solid-State Lett.* **11**, A198–A201 (2008).

19. Wolf, M., Kotzé, H., Fischer, N. & Claeys, M. Size dependent stability of cobalt nanoparticles on silica under high conversion Fischer–Tropsch environment. *Faraday Discuss.* **197**, 243–268 (2017).

20. Pinna, N. & Niederberger, M. Surfactant-free nonaqueous synthesis of metal oxide nanostructures. *Angew. Chemie - Int. Ed.* **47**, 5292–5304 (2008).

21. Pinna, N., Karmaoui, M. & Willinger, M. G. The ‘benzyl alcohol route’: An elegant approach towards doped and multimetal oxide nanocrystals: Short review and $ZnAl_2O_4$1n anostructures by oriented attachment. *J. Sol-Gel Sci. Technol.* **57**, 323–329 (2011).

22. Liu, X., Qiu, G. & Li, X. Shape-controlled synthesis and properties of uniform spinel cobalt oxide nanocubes. *Nanotechnology* **16**, 3035–3040 (2005).

23. He, T., Chen, D. & Jiao, X. Controlled Synthesis of Co_3O_4 Nanoparticles through Oriented Aggregation. *Chem. Mater.* **16**, 737–743 (2004).

24. Dlamini, M. W. Spherical carbons as model supports for Fe , Co and Fe-Co Fischer-Tropsch catalysts. PhD Thesis (University of the Witwatersrand, Johannesburg, 2016).

25. Sharifi, S. L., Shakur, H. R., Mirzaei, A., Salmani, A. & Hosseini, M. H. Characterization of Cobalt Oxide Co_3O_4 Nanoparticles Prepared by Various Methods: Effect of Calcination Temperatures on Size, Dimension and Catalytic Decomposition of Hydrogen Peroxide. *Int. J. Nanosci. Nanotechnol.* **9**, 51–58 (2013).

26. Xiong, H., Moyo, M., Rayner, M. K., Jewell, L. L., Billing, D.G. & Coville, N.J. Autoreduction and Catalytic Performance of a Cobalt Fischer-Tropsch Synthesis Catalyst Supported on Nitrogen-Doped Carbon Spheres. *ChemCatChem* **2**, 514–518 (2010).

27. Moyo, M. Cobalt and Iron Supported on Carbon Spheres Catalysts for Fischer. PhD Thesis (University of the Witwatersrand, Johannesburg, 2012).

CHAPTER 5: Synthesis and characterization of Co_3O_4/Cdots

5.1 Introduction

The aim of this study was to synthesize Co_3O_4/ Cdots with different Co_3O_4/Cdots ratios in order to investigate the effect of different surface functional groups as well as the effect of different Cdots concentrations on the reduction of Co_3O_4 to metallic Co. The activity and selectivity of the prepared catalysts was also to be investigated. However there were difficulties in studying the reduction of Co_3O_4 supported on Cdots using TPR, which will be discussed later. Hence, the project was narrowed down to studying the reduction of Co_3O_4 supported on N-free (Cdots-1) and N-doped (N-doped Cdots-1) at the same concentration of Co_3O_4.

The synthesis of Co_3O_4/Cdots was based on the knowledge of the Co_3O_4 and Cdots (and N-doped Cdots) chemical properties. It is known that because of their surface functional groups, Cdots disperse in water[1], and according to Shi *et al.*[2], Co_3O_4 nanoparticles also disperse in water. The FT-IR spectra of both Co_3O_4 and Cdots obtained in the experiments carried out in **CHAPTER 3** and **CHAPTER 4** also confirmed the presence of the hydrophilic surface functional groups (O-H, COO^-, *etc*). Therefore water was used as a solvent for the synthesis of Co_3O_4/Cdots and Co_3O_4/N-doped Cdots supported catalysts.

5.2 Experimental procedure

Cdots (2.7 g) were dispersed in 600 mL of distilled H_2O in a 1 L beaker placed on a magnetic stirrer and the solution was stirred (with a 8×30 mm magnetic stirrer bar) for 5 hrs under ambient temperature to achieve a homogeneous dispersion. A solution containing 0.3 g of Co_3O_4 in 600 mL in a different 1 L beaker was also prepared and stirred for 5 hrs on a separate magnetic stirrer. Thereafter, the brown Cdots solution was added to the black Co_3O_4 solution, and the total solution was allowed to react overnight. The colour of the mixture changed to a brown-black colour. Thereafter, distilled water was removed by rotary evaporation (as in **CHAPTER 3**, **section 3.1.2**) at 60 °C. The same reaction was carried out for the synthesis of the Co_3O_4/N-doped Cdots supported catalyst.

5.3 Characterization techniques

X-ray diffraction (XRD), Transmission electron microscopy (TEM), Thermal gravimetric analysis (TGA), Fourier transform infrared (FT-IR), temperature programmed reduction (TPR) and *in-situ* X-ray diffraction (*in-situ* XRD) techniques were used to characterize the structural, thermal and chemical properties of the prepared catalysts.

5.3.1 *In-situ* X-ray diffraction (XRD)

The *in-situ* XRD was used to determine the metallic phase/s formed during the reduction of Co_3O_4 in Co_3O_4/Cdots-1 and Co_3O_4/N-doped Cdots-1. TPR and *in-situ* XRD provide a good insight on the expected catalytic behaviour during F-T reduction[3]. However, *in-situ* XRD unlike TPR, gives information about the temperature at which the catalyst is reduced as well as the change in the crystallographic phase during reduction[4,5]. In has been reported that metallic Co can exist as both Co (fcc) and Co (hcp), and the Co (hcp) is the more active form of metallic Co as it has the appropriate active sites desired for F-T conversion[6–8]. Therefore, by studying the Co phases formed during Co_3O_4 reduction, one can predict the catalytic behaviour of Co under F-T conditions.

The *in-situ* data was measured and recorded on a Bruker AXS D8 Advance diffractometer equipped with an Anton Paar XRK 900 reaction furnace. The measurements were carried out using $Co_{K\alpha}$ X-ray radiation (0.178897 nm) operating at 40 kV and 40 mA. The samples were reduced using 5 % H_2 (balanced with N_2)[3,4]. The temperature was raised from 30 to 570 °C, at increments of using a heating rate of 5 °C/min. The *in-situ* XRD patterns were measured between 20 and 80 ° with a 0.026 ° step. The same step size was used for all the data collected. The data was analysed using Rietveld refinement on TOPAS5. The structure models of Co_3O_4, CoO, Co (fcc) and Co (hcp) were obtained from the Inorganic Crystal Structure Database (ICSD). The Co_3O_4/N-doped Cdots-1 sample was also analysed under inert (N_2) gas condition to determine the reducing properties of N-doped Cdots.

5.4 Results and discussions

5.4.1 X-ray diffraction: XRD

The XRD patterns of Co_3O_4/Cdots-1 and Co_3O_4/N-doped Cdots-1 are shown in **Figure 5.1** below. The XRD patterns were compared to those obtained for Cdots-1 and N-doped Cdots-1 synthesized in **CHAPTER 3**. The XRD patterns show the presence of Co_3O_4, with peaks similar to those observed in **Figure 4.2**. The (111) plane of Co_3O_4, which is expected to appear at *ca* 2θ = 21 °, could not be well distinguished in these XRD patterns. This peak could be masked by the presence of a broad feature which is attributed to the presence of amorphous carbon in the sample arising from the cdots, which both appears at 2θ = 23 ° as shown in **Figure 3.7.a)** and **3.7d)**. This is expected since 9/10 mass ratio of each sample contains functionalized Cdots.

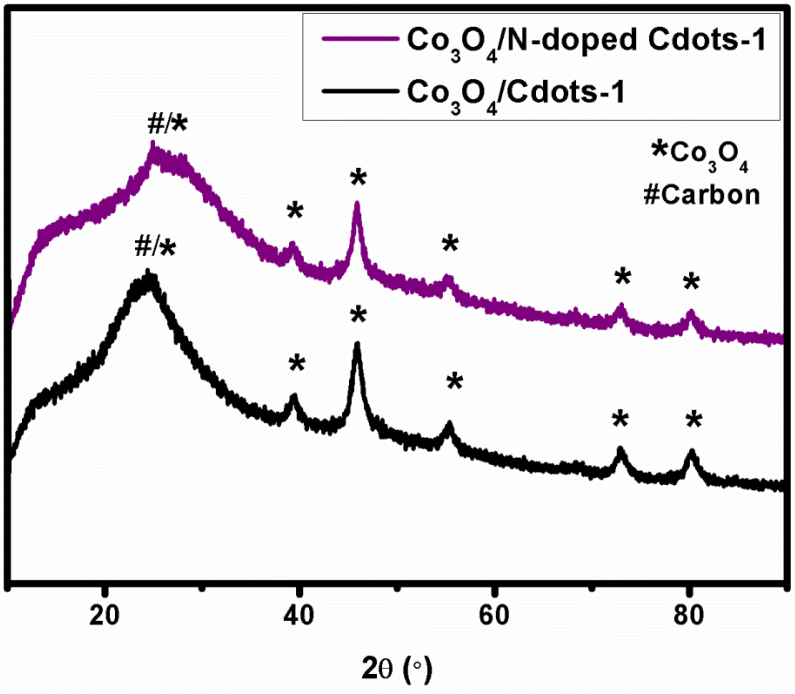


Figure 5.1: XRD pattern of Co_3O_4/Cdots-1and Co_3O_4/N-doped Cdots-1

5.4.2 Transmission Electron Microscopy: TEM

The TEM image of Co_3O_4/ Cdots-1 is represented by **Figure 5.2** below. The image shows Co_3O_4 nanoparticles with average particle size around 11.4 nm. Most of the Co_3O_4 nanoparticles are highly dispersed, with Cdots-1 nanoparticles surrounding each Co_3O_4 nanoparticle. The high dispersion of the metal nanoparticle is very important for the F-T reaction, as this would ensure that the metal nanoparticles do not sinter easily.

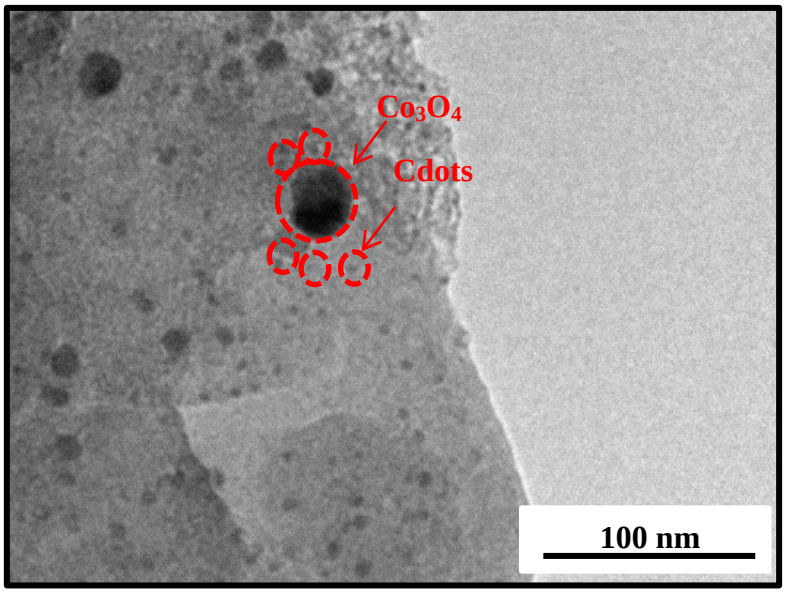


Figure 5.2: TEM image of Co_3O_4/Cdots-1

5.4.4 Thermal gravimetric analysis: TGA

TGA was used in this case to determine the Co_3O_4 loading in each sample. All measurements were taken under the conditions described in **section 3.7**. **Figure 5.3** and **5.4** below show the TG and the DTG graphs of Cdots-1 and Co_3O_4/Cdots-1, and N-doped Cdots-1 with Co_3O_4/Cdots-1, respectively. The TG thermograms of the Cdots and N-doped Cdots showed that both of Cdots and N-doped Cdots samples had fully decomposed at *ca* 700 °C. It has also been reported that Co_3O_4 is very stable between *ca* 35 and 900°C under oxidising conditions[3,9]. Therefore, the % loaded Co_3O_4 is the % of residue left after Cdots-1 and N-doped Cdots-1 decomposition. From the TG thermogram of Co_3O_4/Cdots-1, it can be observed that the residual weight left after decomposition is 10.5 % corresponding Co_3O_4. The DTG thermograph of Co_3O_4/Cdots-1 in **Figure 5.3d)** shows that Cdots-1 is completely decomposed at *ca* 555 °C, while without Co_3O_4, the final decomposition occurs at *ca* 565 °C. This small change may be because Co_3O_4 can catalyse the decomposition of the carbon residue[3,9]. Typically, in the presence of Co_3O_4, both the onset temperature (i.e the temperature at which carbon starts decomposing) and the final decomposition temperature of carbon are reduced. Moyo[9] showed that the onset decomposition temperature of nitric acid functionalized CSs alone was 560 °C, and decrease to 400 °C in the presence of a catalyst. Dlamini[3] also reported the similar observation for non-functionalized CSs.

In **CHAPTER 3** it was noted that the DTG peak at *ca* 102 °C (3 %) may be due to adsorbed moisture, and the peak at *ca* 301 °C (55 %) weight loss may be due to the hydroxyl and/ carbonyl functional on the surface of the Cdots-1. From the DTG of Co_3O_4/Cdots-1, it can be noted that there are no decomposition peaks below *ca* 100 °C or at 300 °C. However, there are 2 peaks at *ca* 212 °C and *ca* 347 °C with 13 % and 15 % weight loss, respectively. These two peaks may be due to a shift in the decomposition temperature of hydroxyl and carbonyl groups, respectively. This evidence suggests that the Cdots-1 are attached to Co_3O_4 via hydroxyl and carbonyl, and their interaction require higher temperatures to remove the Co_3O_4 bound functional group. The peak at *ca* 555 °C (72 %) is due to the carbon decomposition.

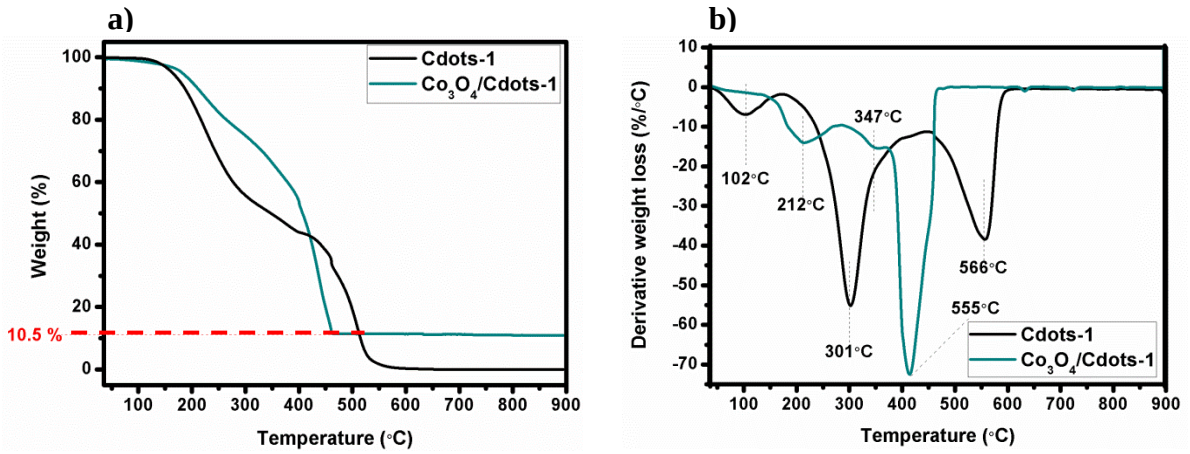


Figure 5.3: **a)** The TG and **b)** DTG thermograms of Cdots-1 and Co_3O_4/Cdots-1

The TG and DTG thermograms of N-doped Cdots-1 and Co_3O_4/N-doped Cdots-1 are shown in **Figure 4.8a)** and **b)** below. The TG graph of Co_3O_4/ N-doped Cdots-1 shows that only 9.6 % of sample is left after the decomposition of N-doped Cdots-1. The shift in the weight loss peak at *ca* 202 °C (30 %) may be due to the interaction between the Cdots functional groups and Co_3O_4. The DTG graph shows that most of N-doped Cdots-1 decomposition occurs at *ca* 442 °C (60 %), which are due to the catalysed oxidation of carbon by Co_3O_4. Without Co_3O_4 catalyst, the final decomposition temperature of N-doped Cdots is *ca* 606 °C. Therefore the final decomposition temperature of the N-doped Cdots-1 is drastically affected by the presence of the Co_3O_4 catalyst compared to the Cdots-1 decomposition, which is shifted by *ca* 10 °C.

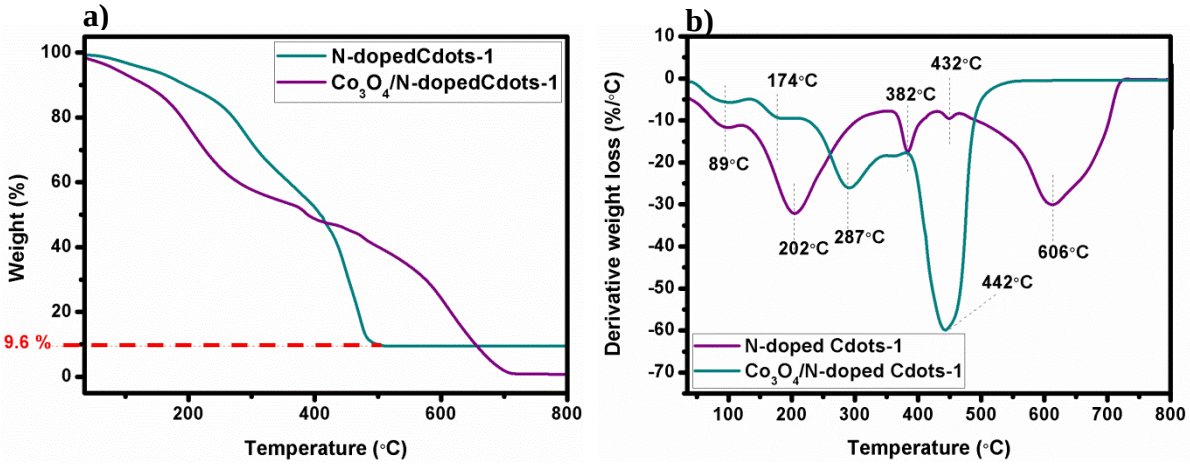


Figure 5.4: **a)** The TG and **b)** DTG thermograms of N-doped Cdots-1 and Co_3O_4/N-doped Cdots-1

5.4.5 Fourier transform infrared spectroscopy: FT-IR spectroscopy

FT-IR was used to investigate the type of bond interactions that might exist between Co_3O_4 and functionalized Cdots. **Figure 5.5a)** and **b)** shows the FT-IR spectra of Co_3O_4/ Cdots-1 and Co_3O_4/ N-doped Cdots-1. The spectra were compared with the spectra of the starting materials. It is known that the surface functional groups of Cdots are affected when metal/Cdots nanocomposites are synthesized[10–13]. Guo *et al.*[13] synthesize Ni@Cdots nanocomposite for catalytic reduction of Cr^{6+} to Cr^{3+}. The FT-IR spectrum of Cdots showed the presence of a carbonyl stretch at 1761 cm^{-1}, which disappeared in the Ni@Cdots spectrum. It was suggested that this could be due to the interactions between the carbonyl surface functional groups of Cdots and the Ni metal[13]. Similar observations were expected for Co_3O_4 and functionalized Cdots. However, FT-IR spectra of both the Co_3O_4/Cdots-1 and Co_3O_4/ N-doped Cdots-1 resembles those of the Co_3O_4, and this suggests that there were no interactions between the Co_3O_4 nanoparticles and the functionalized Cdots. Therefore information regarding the type of bonding interactions between Co_3O_4 and the functionalized Cdots could not be obtained.

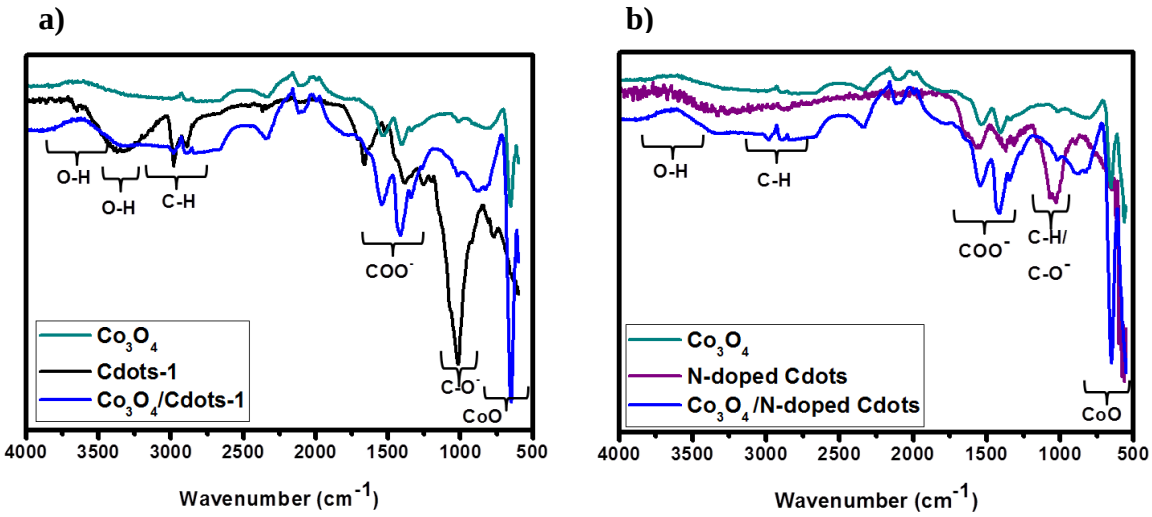


Figure 5.5: FT-IR spectra of **a)** Co_3O_4, Cdots-1 and Co_3O_4/ Cdots-1, and **b)** Co_3O_4, N-doped Cdots-1 and Co_3O_4/ N-doped Cdots-1

5.4.6 Temperature Programmed Reduction: TPR

TPR was used in an attempt to study the effect of Cdots and N-doped Cdots on the reduction temperature of the Co_3O_4 phase. It has been reported that functionalization of carbon nanomaterial by acids and/or nitrogen doping (N-doping) improves the surface chemistry of the carbon nanomaterial[14]. Surface functional groups helps keep the metal catalyst

nanoparticles dispersed through metal to support interactions (MSIs) effect, which also improves the stability of the metal catalysts during the F-T process[15–18]. The Co to carbon interactions therefore improved the catalytic activity of metal catalysts. N-doping in particular has shown excellent improvements in the MSIs stability[15–18]. N-doping in carbon nanomaterials can be via pyridinic, pyrrolic, graphitic and nitroxides configuration[17] as shown earlier in **Figure 3.19**. N-doping produces defects in the carbon nanostructure which can act as active sites for the metal adsorption[15–18]. However, different N-doping configurations affect the catalytic stability and activity of metal catalysts differently. Xiong *et al.*[19] reported that on Fe catalyst supported on N-doped CSs with predominantly pyridinic and pyrrolic configuration showed better F-T activity than Fe supported on N-doped CS with a predominantly graphitic nitrogen configuration[19].

Cdots and N-doped Cdots have the advantages of having a readily functionalized surface. As shown earlier in the XPS study (**section 3.4.3.2**), Cdots-1 contain predominantly acidic functional groups, while the N-doped Cdots have both acidic functional groups and N-functional groups with predominantly pyridinic and pyrrolic configurations. Therefore Cdots-1 and N-doped Cdots-1 were expected to affect the stability and activity of Co differently.

Functionalized carbon nanomaterials have better MSIs with metals than non-functionalized carbon nanomaterials[3,9]. This is usually observed by an increase in the reduction temperature of Co_3O_4 to CoO and Co (in **eq. 4.1** and **4.2**). TPR is usually used to study the MSI effect on the reduction of Co_3O_4. However, for Co_3O_4 supported on Cdots and N-doped Cdots, the TPR profiles are difficult to explain. Further studies will be needed to rationalize the data. For Co_3O_4/ N-doped Cdots-1, only one peaks were observed between *ca* 350 and 500 °C, which may be due to the reduction of Co_3O_4 to metallic Co, implying that the reduction process happens without the formation of CoO intermediate. For Co_3O_4/Cdots-1 shows the presence of two distinct peaks between *ca* 350 and 500 °C, which may be due to the reduction of Co_3O_4 to CoO, and further CoO to metallic Co reduction. The peaks between *ca* 700 and 800 °C observed in both samples could result from methane formation from the support catalysed by metallic Co[3,9].

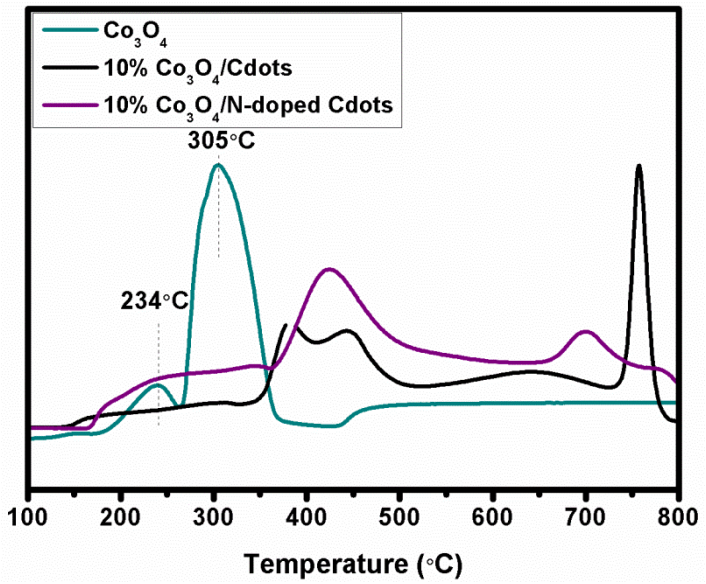


Figure 5.6: TPR profile of Co_3O_4, Co_3O_4/ Cdots-1and Co_3O_4/ N-doped Cdots-1

It was also observed that after the TPR study that the sample tube was brownish in colour on the inside, implying that the functionalized Cdots were affected by the reduction conditions. Therefore, an experiment was carried out in an attempt to study the reducibility of the support without the catalyst. It was observed that volatile material was produced from the supports, and in this case these volatile materials were transferred through the instrument during reduction and blocked the TPR detector. Thus, further reduction data could not be obtained. From these studies, it was assumed that Cdots-1and N-doped Cdots-1 might be reduced under these conditions, which could be detrimental for F-T reactions.

5.4.7 *In-situ* X-ray diffraction (XRD)

The *in-situ* results are presented by **Figure 5.7a)**, **b)** and **c)** below. The colours on each pattern represent the reduction temperatures as represented next to each figure. **Figure 5.7a)** and **b)** represents the reduction patterns of the Co_3O_4/Cdots-1 and Co_3O_4/N-doped Cdots-1 under H_2, respectively. **Figure 5.7c)** represents the reduction of Co_3O_4/N-doped Cdots-1 under inert gas conditions. The *in-situ* reduction behaviour of Co_3O_4 in the Co_3O_4/Cdots-1 and Co_3O_4/N-doped Cdots-1 at 5 % H_2 gas (balanced with N_2) are similar. Between 30 and 240 °C, only cubic Co_3O_4 phase present. As the temperature is increased from 240 to 360 °C, Co_3O_4 is reduced, and the peaks at 2θ = 52 °, 70 ° and 77 ° corresponding to the (400), (511) and (440) planes of Co_3O_4 disappear, and the CoO peaks at 2θ = 42 °, 50 ° and 73 ° corresponding to the (111), (200) and (311) appear. This means that Co_3O_4 is reduced to CoO at these temperatures. The CoO is further reduced to Co (fcc) phase (2θ = 46 ° and 51°) from

390 to 570 °C, and this is presented by the disappearance of the CoO peaks at 2θ = 42 °, 50 ° and 73 °. Although Co (fcc) is a predominant phase of Co at these temperatures, TOPAZ showed that it is not the only Co phase present. The CoO (220) phase (2θ = 59 °) and Co_3O_4 (422) phase (2θ = 63 °) are still present at these temperatures. Similar results were also observed for Co_3O_4/N-doped Cdots-1.

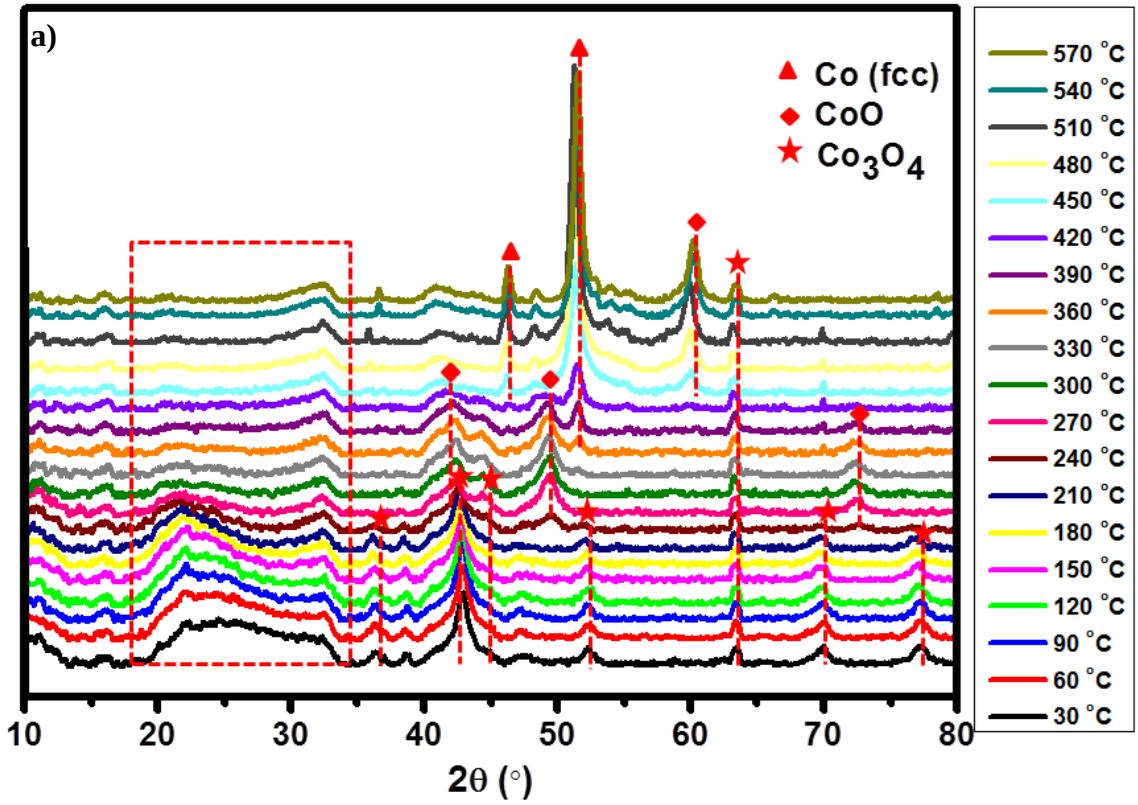


Figure 5.7a): *In-situ* XRD pattern of Co_3O_4/Cdots-1 under H_2 reducing conditions

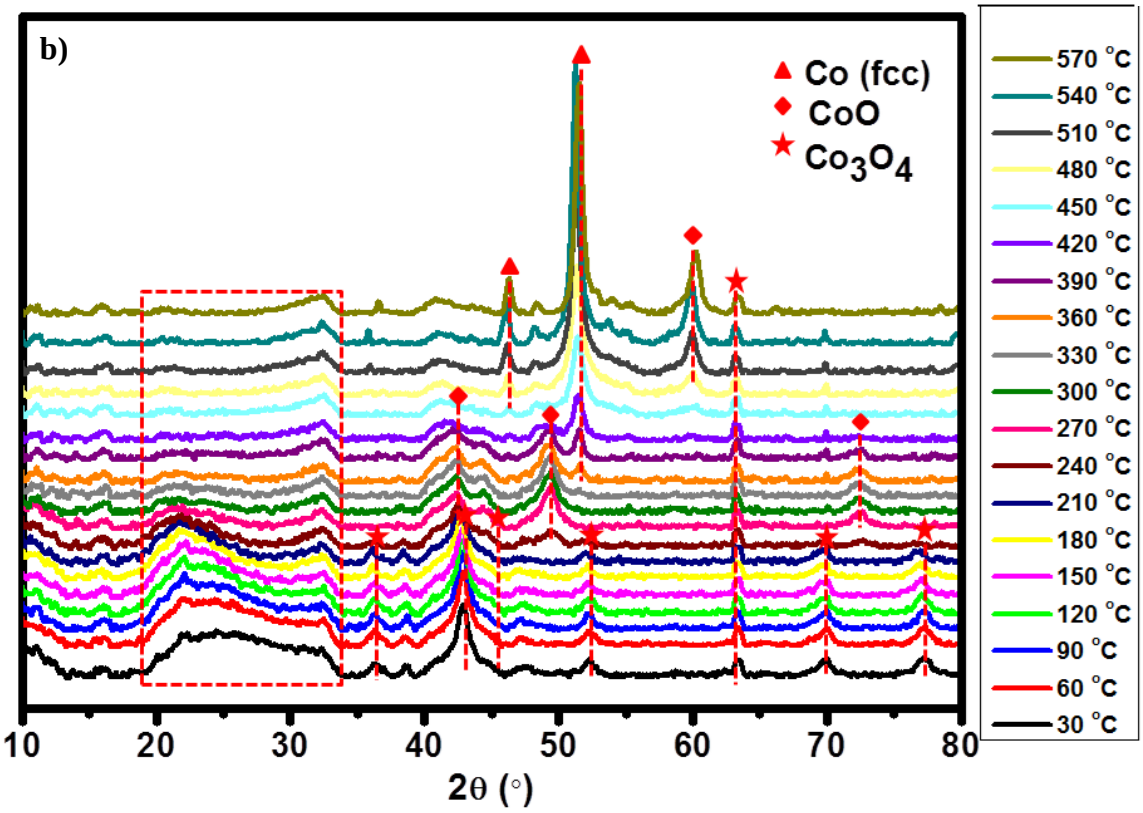


Figure 5.7b): *In-situ* XRD pattern of Co_3O_4/N-doped Cdots-1 under H_2 reducing conditions

Figure 5.7c) shows the reduction behaviour Co_3O_4 in Co_3O_4/N-doped Cdots-1 under inert (N_2) conditions. In this experiment, the reducing properties of N-doped Cdots where tested. It has been reported that Cdots and N-doped Cdots can reduce metal salts into their metallic form[20–22]. Cdots have been used as reduction and stabilizing agents for MnO_2, Ag and Pd[20–22]. Therefore it was hypothesized that the prepared Cdots and N-doped Cdots can also reduce Co_3O_4. The results show that the reduction of Co_3O_4 under these conditions is similar to the Co_3O_4 reduction under H_2, except at 570 °C. The pattern shows that between 30 and 240 °C Co is present in the cubic Co_3O_4 phase. Co_3O_4 is reduced to CoO 240 to 360 °C, and the peaks at 2θ = 42 °, 50 ° and 73 ° corresponding to the (111), (200) and (311) of CoO appear. From 390 °C to 570 °C, the peaks at 2θ = 46 ° and 51° appear, which correspond to the Co (fcc) phase. This indicates the reduction of CoO to Co (fcc). As the temperature is increased further from 540 °C to 570 °C, the Co (hcp) phase (2θ = 55 °) is also formed. The Co (hcp) is has been reported as the most F-T active Co form than the Co (fcc) phase, with high CO conversion and high selectivity towards and long chain (C_{5+}) hydrocarbon compared to Co (fcc)[7,23]. This is because Co (hcp) has more active surface sites than Co(fcc)[6,23,24]. The results suggest that the reduction of Co_3O_4 by N-doped Cdots-1 produce the formation of both the

F-T catalytically active Co (fcc) and Co (hcp). However the properties of N-doped Cdots-1 that assist this regard are not yet understood.

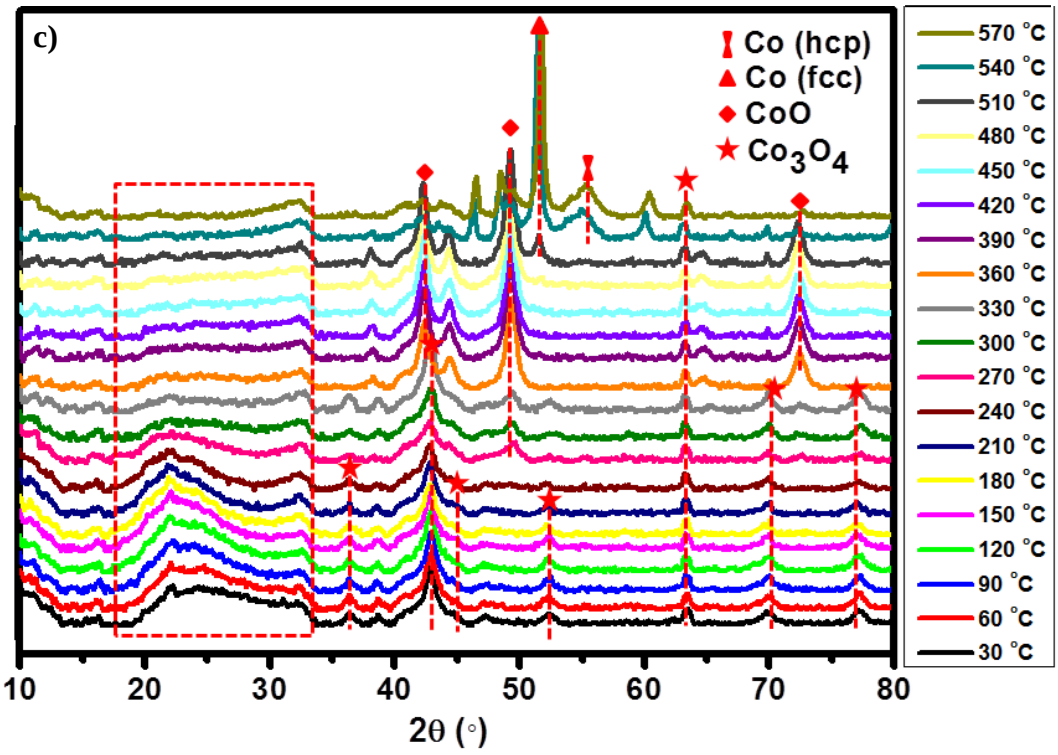


Figure 5.7c): *In-situ* XRD pattern of Co_3O_4/N-doped Cdots-1 under inert (N_2) conditions

5.4.8 The effect of metal to support interaction

The TPR profile of Co_3O_4 in **Figure 4.4** showed that Co_3O_4 is completely conversed to metallic Co at 305 °C under 5% H_2 conditions. However, when Co_3O_4 is supported on functionalized Cdots, the *in-situ* XRD shows that Co_3O_4 is predominantly reduced to Co (fcc) (and Co (hcp)) only at temperatures between 540 °C to 570 °C. This suggests that the MSI causes a delay in the reduction of Co_3O_4 to Co (fcc) and Co (hcp).

5.4.9 Reduction properties of N-doped Cdots-1

To investigate whether the presence of nitrogen on the surface of Cdots were responsible for the reduction of Co_3O_4 to Co (fcc) and Co (hcp), the Cdots were annealed at 500 °C. According to the TG-MS data, the surface functional groups of N-doped Cdots are decomposed at 500 °C this temperature was used to anneal the Cdots.

The reducing properties of Cdots can result from two factors; 1) from their surface functional grounds (such as hydroxyl functional groups), or 2) due to the reducing nature of the carbon nanomaterials. Unnikrishnan *et al.*[20] used Cdots for the reduction of potassium permanganate

($KMnO_4$) to MnO_2 under mild conditions (75 °C). The authors reported that the reduction of MnO_2 is accompanied by oxidation of the C=C and oxygen-type functional groups of Cdots. Liu *at al.*[21] also reported a similar observation from the formation of Ag-N-doped Cdots nanocomposite. Xiong *et al.*[25] used N-doped and non-functionalized CSs to show that CSs can reduce Co_3O_4 to metallic Co without H_2 or any other reducing agent. The authors also noted that the reducing abilities of CSs are solely dependent on the carbon sp^2/sp^3 domains, and independent of their surface functional groups. Therefore, following Xiong *et al.*, N-doped Cdots were annealed in an attempt to remove the surface functional groups. The annealing conditions were as follows:

Annealing procedure

Annealing was done using horizontal chemical vapour deposition (CVD_{hor}) furnace. N-doped Cdots (2.5 g) were dispersed on a quartz boat. The quartz boat was placed in the middle of a hollow tubular quartz reactor (100 cm × 4 cm) loaded in a furnace. The furnace ramped up to 500 °C, and then held at this temperature for 2 hrs. Ar was used as an inert gas throughout the reaction and the gas flow rate was kept at 20 mL/min. After 2 hrs, the tube and the product were allowed to cool down to room temperature. After annealing, it was found that the mass of the product was 1.1 g; therefore 44 wt% of N-doped Cdots-1 was lost.

The structural, chemical, physical and optical properties of the annealed N-doped Cdots-1 were investigated using XRD, TEM, Raman spectroscopy, FT-IR spectroscopy, TGA and PL spectroscopy. The XRD pattern (supplementary information **Figure S5.8a)**) of the annealed sample showed a peak at 2θ = 19 °, and a shoulder at 2θ = 48 °, this peaks were similar to those obtained for N-doped Cdots-1. The TEM results of the annealed products are shown in **Figure 5.8a)**. It was found that the structural morphology of the N-doped Cdots-1 changed upon annealing. The TEM image shows a large carbon material had been found with an irregular shape. The actual identity of the material is yet to be determined. The FT-IR spectrum of the annealed sample was compared with the FT-IR spectrum (**Figure S5.8b)**) of the as prepared N-doped Cdots-1. It was found that the intensity of the band at 3204 cm^{-1} due to the O-H stretch, and the C-O-C bands between 1500 and 1000 cm^{-1} decreased significantly. This suggests that a significant amount of the surface functional groups were remove with annealing. Interestingly, the annealed product was Raman active. This might be due to the removal of surface functional responsible for fluorescing properties of Cdots[1], and/or morphology change. The results show the D band at *ca* 1364 cm^{-1} which can be

attributed to the sp^3 and sp^2 disorder in the carbon structure[1,26,27]. The band at *ca* 1579 cm^{-1} corresponding to the G band is attributed to the graphitic sp^2 carbon[1,26]. The I_D/I_G ratio of the product was found to be 0.6, suggesting that the material has a low degree of disorder[28]. The TG-DTG graphs of the annealed sample in **Figure S5.8c)** shows that the material is fully decomposed at *ca* 670 °C, while the N-doped Cdots-1 is fully decomposed at *ca* 606 °C. This suggests that the annealed sample is more thermally stable than the as prepared N-doped Cdots-1. The PL spectra (**Figure S5.8d)**) of annealed product showed a weak PL emission peak compared to the as prepared N-doped Cdots-1 sample, suggesting that the PL properties were significantly quenched after annealing. The XRD pattern, FT-IR spectroscopy, TGA and PL emission spectrum are attached in under supplementary **Figure S5.1a)-d)**. Since annealing changed the morphology of the N-doped Cdots, the reducing properties of the N-doped Cdots could not be studied.

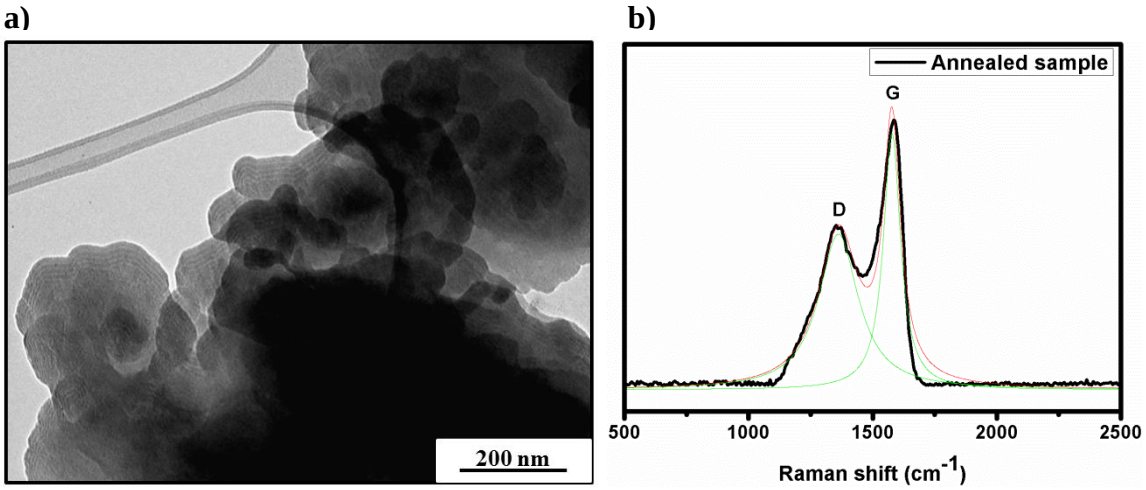


Figure 5.8: **a)** TEM and **b)** Raman spectrum of the product obtained after annealing N-doped Cdots-1 at 500 °C under Argon gas

4.3.3.8 General discussion

The *in-situ* XRD results obtained from the reduction processes under H_2 conditions and under inert conditions show the disappearance of the amorphous peak between 2θ = 20 ° and 30 ° as the reduction temperature was increased (as highlighted in each figure). This peak corresponds to the Cdots and N-doped Cdots amorphous peak. This suggests that the support either get reduced or it decomposes as explained in **section 5.4.6**. The poor thermal stability of the Cdots and N-doped Cdots might be due to its surface functional groups.

Although TOPAS5 was used to identify the phases present, qualitative data such as the % of each phase present and the crystallite sized could not be estimated due to the poor quality of the data. This is due to fluorescence effects of cobalt and a high background signal which is contributing to an overall poor signal to noise ratio thus making the quantification unreliable. Some of the peaks present in the patterns could not be identified without further studies on the material. This will be recommended for future work.

5.5 Conclusion

Co_3O_4/Cdots-1 and Co_3O_4/N-doped Cdots-1 were synthesized using from a solution method using water as a solvent. The TEM of Co_3O_4/Cdots-1 shows Co_3O_4 nanoparticles surrounded by the Cdots. The TGA results confirmed that the Co_3O_4 loading was 10 % on both Cdots-1 and N-doped Cdots-1. TGA results also showed that Cdots-1 and N-doped Cdots-1 decomposes at lower temperature due to the presence of Co_3O_4, which is believed to catalyse the decomposition of Cdots-1 and N-doped Cdots-1. The XRD pattern of both Co_3O_4/Cdots-1 and Co_3O_4/N-doped Cdots-1 showed that the position of Co_3O_4 peaks shifted to higher angle. This shift might be attributed to the MSI between Co_3O_4 and functionalized Cdots.

TPR and *in-situ* XRD studies were conducted in order to investigate the reducibility of Co_3O_4 in Co_3O_4/Cdots-1 and Co_3O_4/N-doped Cdots-1; however in-*situ* XRD gave more insight on the reduction behaviour of Co_3O_4. The *in-situ* XRD showed that Co_3O_4 in Co_3O_4/Cdots-1 and Co_3O_4/N-doped Cdots-1 were reduced to their metallic form at temperatures above 500 °C. However, the reduction conditions were not enough to completely reduce the Co_3O_4 to metallic Co. This suggests that the interaction between metal and the support are strong in such a way that higher temperatures are needed in order to reduce Co_3O_4. The data also showed that N-doped Cdots-1 alone can reduce Co_3O_4 into both Co (fcc) and Co (hcp), which are both F-T active catalytic species. The reducing properties of Cdots and N-doped Cdots are yet to be studied. The reducing condition employed for both TPR and *in-situ* XRD seem to affect the thermal stability of Cdots drastically. This occurrence is not well understood. Therefore further studies on this will be conducted.

References

1. Jelinek, R. Carbon Quantum Dots.1–129 (Springer International Publishing Switzerland , 2017).

2. Shi, N., Cheng, W., Zhou, H., Fan, T. & Niederberger, M. Facile synthesis of monodisperse Co_3O_4 quantum dots with efficient oxygen evolution activity. *Chem. Commun.* **51,** 1338–1340 (2015).

3. Dlamini, M. W. Spherical carbons as model supports for Fe , Co and Fe-Co Fischer-Tropsch catalysts. PhD Thesis (University of the Witwatersrand, Johannesburg, 2016).

4. Phaahlamohlaka, T. N., Kumi, D. O., Dlamini, M. W., Forbes, R., Jewell, L. L., Billing, D. G. & Coville, N. J., Effects of Co and Ru Intimacy in Fischer − Tropsch Catalysts Using Hollow Carbon Sphere Supports : Assessment of the Hydrogen Spillover Processes. *ACS Catal.* **7**, 1568–1578 (2017).

5. Garces, L. J., Hincapie, B., Zerger, R. & Suib, S. L. The Effect of Temperature and Support on the Reduction of Cobalt Oxide: An in Situ X-ray Diffraction Study. *J. Phys. Chem. C* **119**, 5484–5490 (2015).

6. van Heerden, T., van Steen, E. Metal – support interaction on cobalt based FT catalysts – a DFT study of model inverse catalysts. *Faraday Discuss.* **197**, 87–99 (2017).

7. Gnanamani, M. K., Jacobs, G., Shafer, W. D. & Davis, B. H. Fischer-Tropsch synthesis: Activity of metallic phases of cobalt supported on silica. *Catal. Today* **215**, 13–17 (2013).

8. Liu, J., Wang, P., Xu, W. & Hensen, E. J. M. Particle Size and Crystal Phase Effects in Fischer-Tropsch Catalysts. *Engineering* **3**, 467–476 (2017).

9. Moyo, M. Cobalt and Iron Supported on Carbon Spheres Catalysts for Fischer. PhD Thesis (University of the Witwatersrand, Johannesburg, 2012).

10. Kong, D., Yan, F., Han, Z., Xu, J., Guo, X. & Chen, L. Cobalt (ii) ions detection using carbon dots as an sensitive and selective fluorescent probe. *RSC Adv.* **6**, 67481–67487 (2016).

11. Liu, R., Huang, H., Li, H., Liu, Y., Zhong, J., Li, Y., Zhang, S. & Kang, Z. Metal nanoparticle/carbon quantum dot composite as a photocatalyst for high-efficiency cyclohexane oxidation. *ACS Catal.* **4**, 328–336 (2014).

12. Dhenadhayalan, N. & Lin, K. C. Chemically Induced Fluorescence Switching of Carbon-Dots and Its Multiple Logic Gate Implementation. *Sci. Rep.* **5**, 1–10 (2015).

13. Guo, Y., Wang, D., Liu, X., Wang, X., Liu, W. & Qin, W. Synthesis and characterization of the nickel@carbon dots hybrid material and its application in the reduction of Cr(vi). *New J. Chem.* **38**, 5861–5867 (2014).

14. Xiong, H., Jewell, L. L. & Coville, N. J. Shaped Carbons As Supports for the Catalytic Conversion of Syngas to Clean Fuels. *ACS Catal.* **5**, 2640–2658 (2015).

15. Lu, J., Yang, L., Xu, B., Wu, Q., Zhang, D., Yuan, S., Zhai, Y., Wang, X., Fan, Y. & Hu, Z. Promotion Effects of Nitrogen Doping into Carbon Nanotubes on Supported Iron Fischer − Tropsch Catalysts for Lower Olefins. *ACS Catal.* **4**, 613–621 (2014).

16. Li, S., Yao, N., Zhao, F. & Li, X. Nitrogen-doped carbon species: a promising nonmetallic promoter for the Co/SiO_2 Fischer–Tropsch synthesis catalyst. *Catal. Sci. Technol.* **6**, 2188–2194 (2016).

17. He, L., Weniger, F., Neumann, H. & Beller, M. Synthesis , Characterization , and Application of Metal Nanoparticles Supported on Nitrogen-Doped Carbon : Catalysis beyond Electrochemistry Minireviews. *Angew.Chem. Int. Ed.* **55**, 12582 –12594 (2016).

18. Xiong, H., Motchelaho, M. A., Moyo, M., Jewell, L. L. & Coville, N. J. Fischer-Tropsch synthesis: Iron-based catalysts supported on nitrogen-doped carbon nanotubes synthesized by post-doping. *Appl. Catal. A Gen.* **482**, 377–386 (2014).

19. Xiong, H., Moyo, M., Motchelaho, M. A., Tetana, Z. N., Dube, S. M. A., Jewell, L. L. & Coville, N. J. Fischer-Tropsch synthesis: Iron catalysts supported on N-doped carbon spheres prepared by chemical vapor deposition and hydrothermal approaches. *J. Catal.* **311**, 80–87 (2014).

20. Unnikrishnan, B., Wu, C. W., Chen, I. W. P., Chang, H. T., Lin, C. H. & Huang, C. C. Carbon Dot-Mediated Synthesis of Manganese Oxide Decorated Graphene Nanosheets for Supercapacitor Application. *ACS Sustain. Chem. Eng.* **4**, 3008–3016 (2016).

21. Liu, T., Dong, J. X., Liu, S. G., Li, N., Lin, S. M., Fan, Y. Z., Lei, J. L., Luo, H. Q. & Li, N. B. Carbon quantum dots prepared with polyethyleneimine as both reducing agent and stabilizer for synthesis of Ag/CQDs composite for Hg^{2+} ions detection. **322**, 430–436 (2017).

22. Dey, D., Bhattacharya, T., Majumdar, B., Mandani, S., Sharma, B. & Sarma, T. K. Carbon dot reduced palladium nanoparticles as active catalysts for carbon–carbon bond formation. *Dalt. Trans.* **42**, 13821 (2013).

23. Jahangiri, H., Bennett, J., Mahjoubi, P., Wilson, K. & Gu, S. A review of advanced catalyst development for Fischer–Tropsch synthesis of hydrocarbons from biomass derived syn-gas. *Catal. Sci. Technol.* **4**, 2210–2229 (2014).

24. Liu, J. X., Su, H. Y., Sun, D. P., Zhang, B. Y. & Li, W. X. Crystallographic dependence of CO activation on cobalt catalysts: HCP versus FCC. *J. Am. Chem. Soc.* **135**, 16284–16287 (2013).

25. Xiong, H., Moyo, M., Rayner, M. K., Jewell, L. L., Billing, D. G. & Coville, N. J. Autoreduction and Catalytic Performance of a Cobalt Fischer-Tropsch Synthesis Catalyst Supported on Nitrogen-Doped Carbon Spheres. *ChemCatChem* **2**, 514–518 (2010).

26. Xu, Y., Wu, M., Liu, Y., Feng, X. Z., Yin, B. X., He, X. W. & Zhang, Y. K. Nitrogen-Doped Carbon Dots: A Facile and General Preparation Method, Photoluminescence Investigation, and Imaging Applications. *Chem. a Eur. J.* **19**, 2276–2283 (2013).

27. Genc, R., Alas, M. O., Harputlu, E., Repp, S., Kremer, N., Castellano, M., Colak, S. G., Ocakoglu, K. & Erdem, E. High-Capacitance Hybrid Supercapacitor Based on Multi- Colored Fluorescent Carbon-Dots. *Sci. Rep.* **7**, 1–13 (2017).

28. Yang, Y., Cui, J., Zheng, M., Hu, C., Tan, S., Xiao, Y., Yang, Q. & Liu, Y. One-step synthesis of amino-functionalized fluorescent carbon nanoparticles by hydrothermal carbonization of chitosan. *Chem. Commun.* **48**, 380–382 (2012).

CHAPTER 6: GENERAL CONCLUSIONS AND RECOMMENDATIONS

6.1 Conclusions

The purpose of this study was to introduce Cdots as potential support for Co-based F-T catalysts for the preparation of inverse Co/Cdots supported catalyst, which has so far not been reported in the literature. The following conclusions were drawn from the study:

Microwave-assisted synthesis of functionalized Cdots and N-doped Cdots from natural carbon source products such as ascorbic acid, sucrose and chitosan resulted in 21-60 % yield of product. The quantity of product was dependent on the carbon source and reaction conditions. The Cdots and N-doped Cdots were characterized using XRD, TEM, SEM, Raman spectroscopy, FT-IR spectroscopy, XPS, TGA, PL and UV-vis spectroscopy. The structural, chemical, thermal and optical properties of Cdots and N-doped Cdots were comparable to those reported in the literature. The FT-IR spectroscopy and XPS confirmed the presence of functional groups oxygen and nitrogen based functional groups on the surface of the materials. The XPS results also showed that the highest amount of N-doping (~16 wt%) was obtained from the N-doped Cdots-2 sample, derived from a mixture of ascorbic acid and urea. TGA confirmed that both Cdots and N-doped Cdots start decomposing at *ca* 200 °C, due to surface functional groups. This therefore concludes that Cdots and N-doped Cdots are not thermally stable under air. The PL and UV-vis spectroscopy confirmed that both the prepared Cdots and N-doped Cdots are fluorescent materials.

Co_3O_4 catalyst nanoparticles, with crystallite sizes varying from 10 to 20 nm were prepared from the ammonia-assisted "benzyl alcohol route". It has been shown that the varying concentration of water in the reaction mixture affects the crystallite size growth.

The synthesis of Co_3O_4/Cdots produced supported catalyst in which the size of the catalyst is larger (10 nm) than the size of the support (< 5 nm), as it has been shown in the TEM results. The *in-situ* data shows that under H_2 conditions, the Co_3O_4 is reduced to CoO and Co (fcc) at the same temperatures in Co_3O_4/Cdots and Co_3O_4/N-doped Cdots. Which implies that the reduction pathway of Co_3O_4 does not depend on the Cdots surface functional groups. The reduction of Co_3O_4 in Co_3O_4/Cdots and Co_3O_4/N-doped Cdots occurred at high temperature compared to the reduction of the unsupported Co_3O_4. This implies that there are strong metal to support interactions between Co_3O_4 and functionalized Cdots. The *in-situ* data also shows

that N-doped Cdots can reduce Co_3O_4, and the reduction leads to the formation of both Co (fcc) and Co (hcp), which are both active F-T catalysts.

The *in-situ* XRD gave very useful information regarding the interaction between Co_3O_4 functionalized Cdots. However the results opened doors to many questions and possibly a new avenue of research that we are hoping to explore in the future.

6.2 Recommendations

The structural properties of Cdots and N-doped Cdots were only limited to XRD (*ex-situ*) data and TEM sizes. Information such as the spacing of lattice fringes, overall arrangement of lattice planes could not be obtained. This information will be needed in order to understand how functional groups affect the lattice spacing and also to confirm the amorphous nature of Cdots and N-doped Cdots as suggested by XRD.

The other synthesized Cdots from sucrose and N-doped Cdots from a mixture of ascorbic acid and urea were not tested as Co_3O_4 support. Therefore these materials can be tested and compared with the *in-situ* results obtained from other Cdots and N-doped Cdots.

TGA, TPR and *in-situ* XRD data showed that functionalized Cdots have low thermal stability under air and H_2. However the reason for the decomposition of Cdots especially in TPR and *in-situ* XRD studies were not explored. Therefore studying these effects will be important especially since the materials will be used F-T under similar conditions.

The structural or chemical properties of N-doped Cdots that enable reduction of Co_3O_4 without any other reducing agent will also be studied. In this study, an attempt to prepare non-functionalized Cdots by annealing a sample of N-doped Cdots resulted in the formation of carbon materials with a different morphology from Cdots. The aim was to investigate whether non-functionalized Cdots can also reduce Co_3O_4 without any assistance from a reducing agent. If this is true then it will mean that the reduction of Co_3O_4 is achieved by the sp^2/sp^3 type carbon and not the surface functional groups. Preparation of non-functionalized Cdots by other means can be investigated. The formation mechanism of Co (fcc) and Co (hcp) will also need to be studied.

The prepared supported catalysts are recommended for F-T reaction studies. The activity and selectivity of the catalytic Co in Co/Cdots and Co/N-doped Cdots can be studied to complete the investigation.

SUPPLEMENTARY INFORMATION

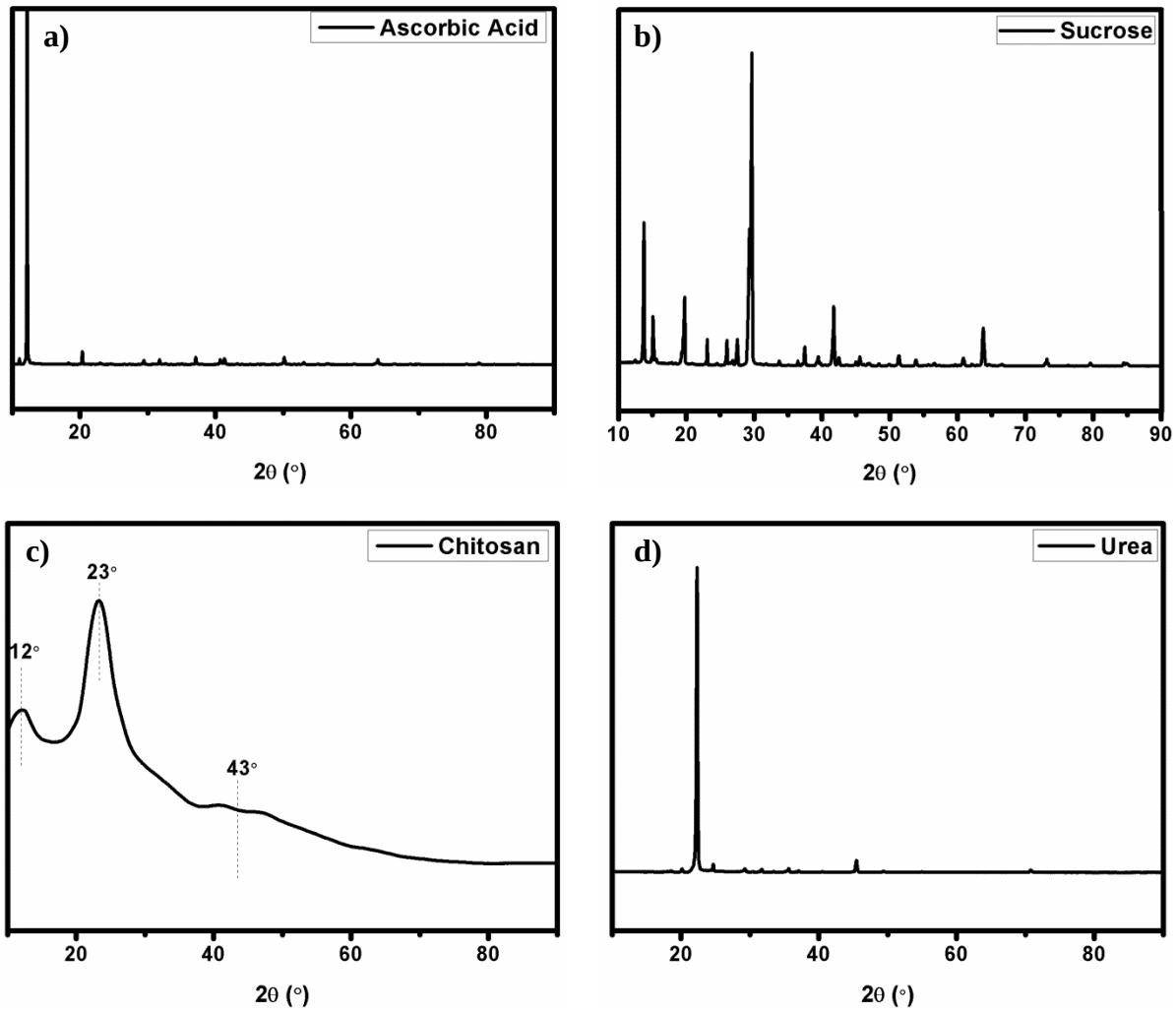


Figure S3.1: XRD patterns of **a)** ascorbic acid, **b)** sucrose, **c)** chitosan, and **d)** urea

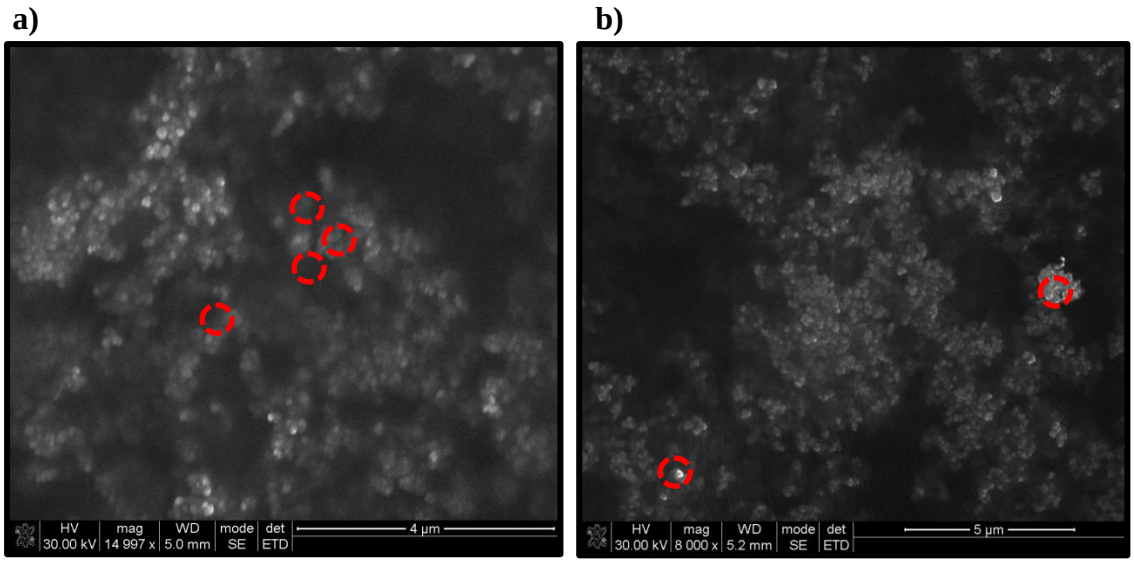


Figure S3.2: Low resolution SEM images of **a)** Cdots-2, and **b)** N-doped Cdots-2. The dotted cycles highlights the Cdots clusters

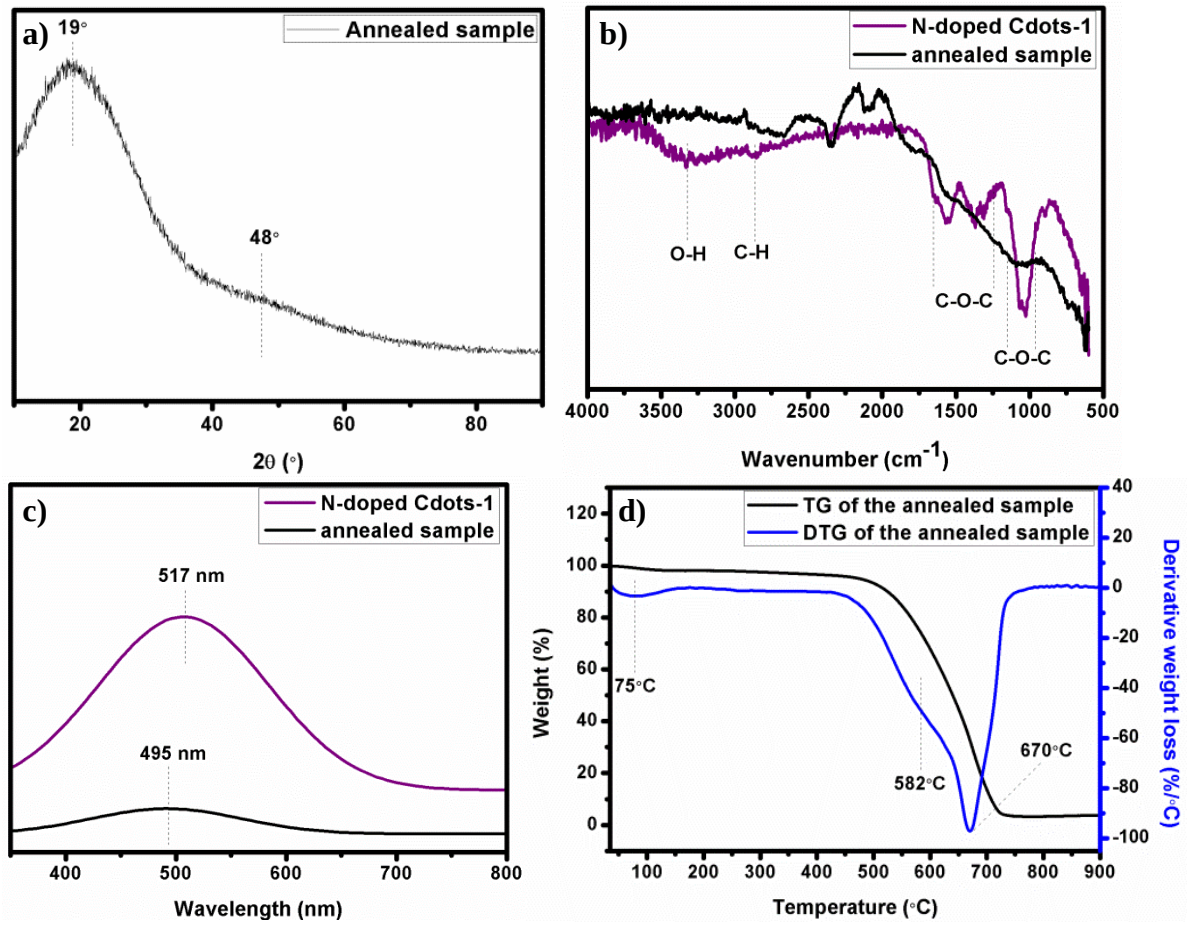


Figure S5.1: a) The XRD pattern, b) FT-IR spectrum, c) PL spectra, and d) TG-DTG thermogram of the annealed N-doped Cdots-1 sample

Table S3.2a): Relative concentrations of carbon bonding states

Sample	Ave. % Concentration				
	sp^2 C-C	sp^2 C-N	sp^3 C-N/C-C	C=O	O-C=O
Cdots-1	50.63	-	27.15	13.66	8.56
Cdots-2	48.21	-	18.00	18.20	15.60
N-doped Cdots-1	49.77	21.04	17.84	8.47	2.88
N-doped Cdots-2	40.11	21.04	18.01	12.47	8.36

Table S3.2b): Relative concentrations of oxygen bonding states

Sample	Ave. % Concentration		
	C=O	O-C=O	C-O-C/C-OH
Cdots-1	27.14	34.56	38.30
Cdots-2	35.25	26.81	37.93
N-doped Cdots-1	58.91	20.88	20.21
N-doped Cdots-2	58.64	33.74	7.61

Table S3.2c): Relative concentrations of nitrogen bonding states

Sample	Ave. % Concentration			
	Pyridinic-N	Pyrrolic-N	Graphitic-N	Organic N
N-doped Cdots-1	41.13	26.44	24.14	8.29
N-doped Cdots-2	20.10	62.20	13.14	4.56